

# **Towards a Complete Photonic Band Gap in the Visible**

Proefschrift ter verkrijging van de graad van doctor aan de Universiteit Utrecht op gezag van de Rector Magnificus, Prof. dr. W.H. Gispen, ingevolge het besluit van het College voor Promoties in het openbaar te verdedigen op maandag 18 maart 2002 des namiddags te 12.45 uur

door

***Krassimir Petkov Velikov***

geboren op 29 juni 1970, te Silistra, Bulgarije




**Universiteit Utrecht**

Promotor: Prof. dr. Alfons van Blaaderen

Faculteit Natuur- en Sterrenkunde, Universiteit Utrecht

FOM - Instituut voor Atoom- en Molecuulfysica, Amsterdam



This work is part of the research program of the Foundation for Fundamental Research on Matter (FOM) with financial support from the Netherlands Organization for Scientific Research (NWO).

ISBN 90-393-2986-9

*На моя син Кристиан.*

---

*A digital version of this thesis can be downloaded from <http://www.colloid.nl>.*

# Contents

<b>Part I .....</b>	<b>1</b>
<b>General Introduction.....</b>	<b>1</b>
<b>I.1 Photonic Crystals .....</b>	<b>1</b>
<b>I.2 Colloidal Particles .....</b>	<b>3</b>
<b>I.3 Colloidal Crystals.....</b>	<b>4</b>
<b>I.4 Methods for Fabrication of Colloidal Photonic Crystals .....</b>	<b>5</b>
<b>I.5 The Computational Method.....</b>	<b>6</b>
<b>I.6 This Thesis .....</b>	<b>7</b>
<b>Part II.....</b>	<b>11</b>
<b>Photonic Crystals of Dielectric Core-Shell Colloidal Particles .....</b>	<b>11</b>
<b>II.1 Synthesis and Characterization of Monodisperse Core-Shell Colloidal Spheres of Zinc Sulfide and Silica.....</b>	<b>13</b>
Introduction .....	14
Experimental Section.....	15
Results and Discussion .....	17
Conclusions .....	27
<b>II.2 Photonic Crystals of Core-Shell Colloidal Particles.....</b>	<b>31</b>
Introduction .....	32
Experimental Section.....	32
Results and Discussion .....	33
Conclusions .....	37
<b>Part III .....</b>	<b>39</b>
<b>Photonic Materials of Metallo-Dielectric Colloidal Particles.....</b>	<b>39</b>
<b>III.1 Synthesis and Characterization of Large Colloidal Silver Particles for Photonic Applications.....</b>	<b>41</b>
Introduction .....	42
Experimental Section.....	43

Results and Discussion .....	44
Conclusions .....	51
<b>III.2 Photonic Glasses of Colloidal Silver Particles .....</b>	<b>55</b>
Introduction .....	56
Experimental Section.....	57
Results and Discussion .....	59
Conclusions .....	69
<b>Part IV .....</b>	<b>71</b>
<b>Photonic Colloidal Crystals with Complex Lattices and Shape-Anisotropic Particles .....</b>	<b>71</b>
<b>IV.1 Layer-by-Layer Growth of Binary Colloidal Crystals .....</b>	<b>73</b>
Introduction .....	74
Experimental Section.....	74
Results and Discussion .....	75
Conclusions .....	82
<b>IV.2 Photonic Crystals of Shape-Anisotropic Colloidal Particles.....</b>	<b>85</b>
Introduction .....	86
Experimental Section.....	87
Results and Discussion .....	87
Conclusions .....	91
<b>Summary .....</b>	<b>93</b>
<b>Acknowledgements .....</b>	<b>95</b>
<b>Publications .....</b>	<b>97</b>
<b>Curriculum Vitae.....</b>	<b>98</b>

---

# Part I

## General Introduction

### I.1 Photonic Crystals

A photonic crystal (PC) is a regularly structured material, with feature sizes on the order of a wavelength (or smaller), that exhibits strong interaction with light.<sup>1-3</sup> The main concept behind photonic crystals is the formation of a 'photonic band gap'. For a certain range of frequencies, electromagnetic waves are diffracted by the periodic modulations in the dielectric constant of the PC forming (directional) stop bands. If the stop bands are wide enough to overlap for both polarization states along all crystal directions, the material is said to possess a complete photonic band gap (CPBG). In such a crystal, propagation of electromagnetic waves with frequencies lying within the gap is forbidden irrespective of their direction of propagation and polarization.<sup>1,2</sup> This leads to the possibility to control the spontaneous emission of light. For example, an excited atom embedded in a PC will not be able to make a transition to a lower energy state as readily if the frequency of the emitted photon lies within the band gap, hence increasing the lifetime of the excited state.<sup>1,2</sup> Photonic crystals with a (directional) stop gap can also have a significant effect on the spontaneous-emission rate.<sup>4</sup> If a defect or mistake in the periodicity is introduced in the otherwise perfect crystal, localized photonic states in the gap will be created. A point defect could act like a microcavity, a line defect like a wave-guide, and a planar defect like a planar wave-guide. By introducing defects, light can be localized or guided along the defects modes.<sup>1,2</sup>

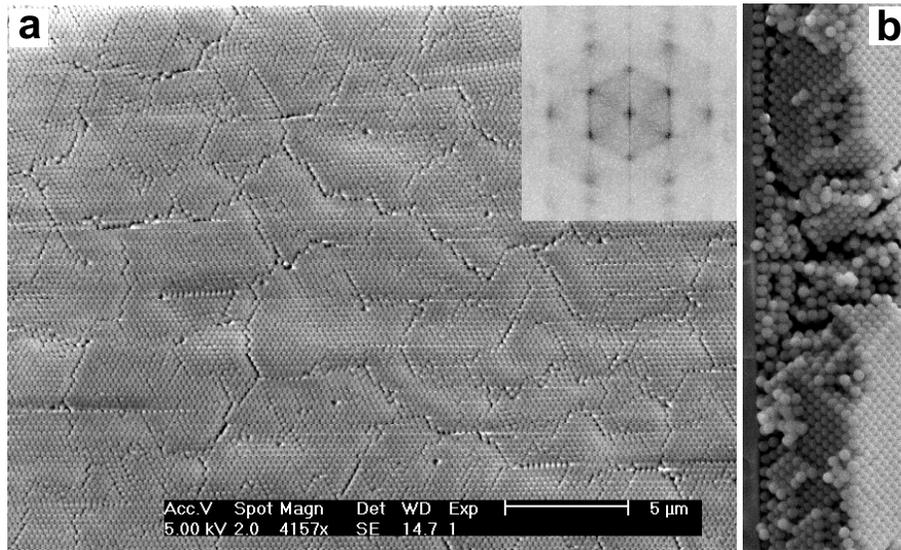


**Figure I.1–1** Scanning electron micrograph (SEM) of a face-centered-cubic (*fcc*) colloidal crystal of closed-packed silica spheres ( $R = 110$  nm). (a) Top view showing the (111) crystal plane. The inset shows a Fourier transformed image of a  $10.76 \times 10.76 \mu\text{m}^2$  region. (b) Side view of a thin colloidal crystal from the same particles.

The possibility to control the propagation and spontaneous emission of light is expected to have a great impact on technology.<sup>5</sup> It is expected that PCs can be applied as filters, high-speed optical switches, optical cavities, light-emitting diodes, low-threshold lasers, waveguides with sharp bending of light, and in several applications in fiber-optics communications. It has also been proposed that PC may hold the key to the continued progress towards all-optical integrated circuits.<sup>6</sup> For recent advances in photonic crystal research see Refs. 5, 7, and 8.

There are two major approaches to the fabrication of photonic crystals: nanolithography and self-assembly. Nanolithography is already widely used by the semiconductor industry. Though it enables the construction of PCs with defects and defect networks, it is however an expensive step-by-step fabrication process. On the other hand, the self-assembly of colloids provides a much simpler, faster, and cheaper alternative to nanolithography. Common examples of self-organized photonic crystals are colloidal crystals of silica (Fig. I.1–1), polystyrene, or more complex core-shell composite particles.<sup>9</sup> Self-assembly has the potential to create samples with full three-dimensional (3D) order, a feature important for engineering larger and complete photonic band gaps. Also, self-assembly methods create easier thicker PCs than lithography. In addition, self-assembly methods are not limited in their length scale, and it is feasible to create materials that are active in the ultraviolet and even the soft X-ray range using colloids of smaller size.<sup>9</sup> A disadvantage is that self-assembly does not provide an easy way for controlled incorporation of defects in a PC.

Important self-organized PCs are the inverted face-centered-cubic (*fcc*) crystals: regular structures of spherical air holes in a high dielectric medium.<sup>10</sup> Such structures, with lattice constants of the order of several hundreds of nanometers, can be created by infiltration of dielectric material into the empty voids of *fcc* crystals that consist of colloidal spheres. One obtains an inverted crystal if the original colloidal material is etched away after the infiltration process. Recently, significant progress was demonstrated towards the fabrication of silicon inverse opals that are expected to have a CPBG in the optical regime ( $\sim 1.5 \mu\text{m}$ ).<sup>11</sup>

Although the precursor of the inverse structure, an *fcc* crystal of dielectric spheres (Fig. I.1–1), only possesses stopgaps,<sup>12</sup> the (local) density of photonic states can still be manipulated significantly. Even for quite modest refractive index contrast, an interesting photonic switch can be realized with *fcc* crystals.<sup>13</sup> Photonic properties of these colloidal crystals can be further improved by the use of particles with a core-shell morphology.<sup>14,15</sup>

Metallo-dielectric PCs have emerged as another (together with inverted *fcc* structures) candidate to achieve a tunable CPBG for optical wavelengths. It has been theoretically shown that CPBG exists in many periodic structures<sup>16,17</sup> and that it is robust against disorder caused by stacking faults and particle polydispersity.<sup>18</sup>

The last group of PCs, which has been hardly studied experimentally, is that of 3D PCs with a complex unit cell (e.g., binary crystals) and crystals of shape-anisotropic particles. It is known from theoretical calculations that the diamond lattice has a CPBG. Although the first plane wave calculations for a diamond lattice of dielectric spheres showed the existence of a large CPBG,<sup>19</sup> recent calculations using the Korringa-Kohn-Rostoker (KKR)<sup>15</sup> method have shown that a CPBG exists but that it is much smaller.<sup>20</sup> The lack of reliable experimental methods for fabrication is the main reason that these crystals have thus far not been explored for colloids.

## I.2 Colloidal Particles

Because of their size (typically 10 – 2000 nm in diameter) and ability to self-organize into 3D periodic structures with different symmetries, colloidal particles of different materials and morphology (both homogeneous and core-shell) are ideal building blocks for the creation of photonic crystals.<sup>2,7,9,14,21</sup> Colloidal core-shell particles are interesting as the structure, size, and composition can be easily altered in a controllable way to tailor their optical properties. Core-shell particles made of a high-index core (e.g.,  $\text{TiO}_2$ ,  $\text{ZnS}$ ) and a low-index shell (e.g.,  $\text{SiO}_2$ ), or vice versa, are of special interest.<sup>14</sup> Because of the high refractive index of the  $\text{ZnS}$ , these particles strongly interact with light. In addition, both  $\text{ZnS}$  and  $\text{SiO}_2$  can be easily doped with

fluorophores in order to study spontaneous emission of light in PCs.

Colloidal metal and metallo-dielectric particles are of great fundamental and industrial interest. It has been shown theoretically that in an *fcc* crystal of metal or metallo-dielectric spheres a CPBG in the visible can be opened.<sup>17,22</sup> As metal particles of sizes larger than 100 nm are hardly available, a new synthesis procedure based on controlled aggregation or seeded growth had to be developed.

Finally, non-spherical colloidal particles can also be used as building blocks for PCs. Crystals of shape-anisotropic building blocks might provide a mechanism for controlling the polarization modes of the emitted light.<sup>23</sup> The aspect ratio of shape-anisotropic particles (e.g., ellipsoids) can be used as an additional parameter to engineer the photonic band gap. Recently, it was demonstrated that spherical, amorphous and polycrystalline (e.g., SiO<sub>2</sub>, ZnS, TiO<sub>2</sub>) particles, or core-shell particles of these materials undergo anisotropic plastic deformation under high-energy ion irradiation. Individual particles can be turned into oblate or prolate ellipsoids with precise control over the aspect ratio.<sup>24</sup>

### I.3 Colloidal Crystals

Colloidal crystals are regular arrays of particles.<sup>25</sup> Under suitable conditions, colloidal particles can self-organize into a colloidal crystal with long-range order. These materials have been the subject of study for several decades as a condensed matter model system. Nowadays, colloidal crystals have received renewed attention

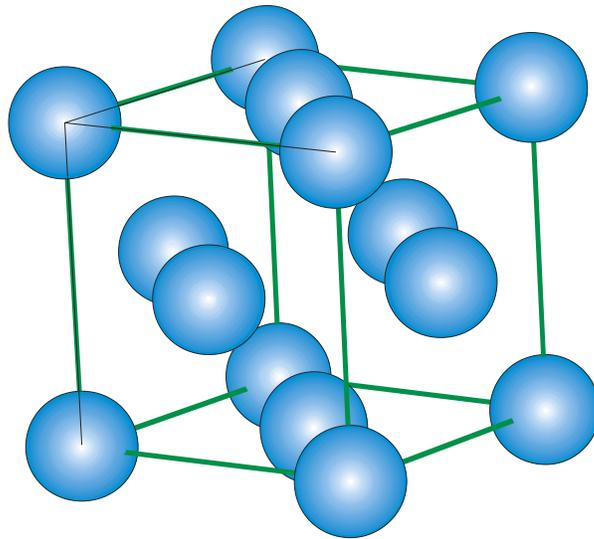


**Figure I.3–1** Schematic representation of the unit cell of a face-centered-cubic (*fcc*) crystal.

as an alternative way to achieve dielectric periodicity on a nanometer to micrometer scale.<sup>14,26-32</sup>

Colloidal crystals can have a variety of different symmetries. The most common structure for a self-organized colloidal crystal is close-packed: face-centered-cubic (*fcc*) (see Fig. I.3–1), hexagonal close-packed (*hcp*) or randomly stacked hexagonal close-packed layers. Dispersions of highly charged, colloidal particles in low ionic strength aqueous solutions can form an *fcc* or a body-centered-cubic (*bcc*) crystals depending on the details of the particle interaction potential. Body-centered-tetragonal (*bct*) colloidal crystals were observed in a colloidal suspension in the presence of an external electric field.<sup>33</sup> More complex, binary colloidal crystals of large (*L*) and small (*S*) particles with stoichiometry  $LS_2$  (atomic analog  $AlB_2$ ) and  $LS_{13}$  (atomic analog  $NaZn_{13}$ ) were observed in natural opals,<sup>34</sup> in suspensions of charge-stabilized polystyrene<sup>35</sup> and in suspensions of hard-sphere-like PMMA<sup>36</sup> particles.

## I.4 Methods for Fabrication of Colloidal Photonic Crystals

The process of colloidal crystallization has been intensively studied, leading to the development of several methods to make high quality crystals. These techniques include electro-hydrodynamic deposition,<sup>37,38</sup> colloidal epitaxy,<sup>28</sup> depletion-induced crystallization,<sup>39</sup> convective self-assembly (controlled drying),<sup>40</sup> and physical confinement.<sup>41</sup> Bimodal  $LS_2$  and  $LS_{13}$  colloidal crystals with complex structure have been observed in binary mixtures of spherical colloids with specific ratios of their radii.<sup>35,36</sup>

The most popular method for creating colloidal crystals is sedimentation in gravity<sup>25</sup> of dispersed colloids. The main drawback of this method is the formation of polycrystalline domains of unknown sizes in the samples. In addition, it is difficult to control the crystal thickness.

To grow close-packed colloidal crystals we used a controlled drying method.<sup>11,27,42</sup> Controlled drying has emerged as a simple and reliable method to create large single colloidal crystals. In this method, particles are transported towards the growing front of the crystal, in the meniscus formed between the substrate and the solvent, by a convective flow that is the result of evaporation (and imposed thermal convection<sup>11</sup>). There they crystallize under the action of capillary forces and other surface tension effects (Fig. I.4–1). For a recent review see Ref. 43. The number of crystal layers can be controlled through the particle volume fraction.

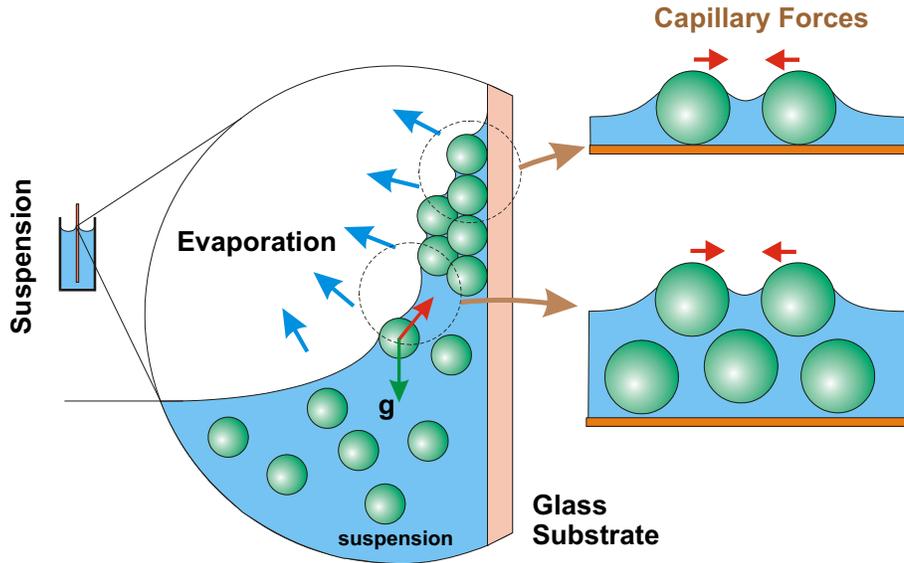


**Figure I.4–1** Schematic representation of the vertical control drying method. Particles are transported towards the drying front by a flow that is the result of the evaporation, and crystallized under the action of capillary forces and other surface tension effects.

## I.5 The Computational Method

In order to calculate reflection, transmission, and absorption of electromagnetic waves in a photonic crystal a photonic analogue of the layer Korringa-Kohn-Rostocker (KKR) method was used.<sup>44</sup> This method is not used by many researchers in the field and here we briefly present its background. The KKR method was developed within the first principle multiple-scattering theory.<sup>45-47</sup> A crystal is viewed as a stack of scattering planes. The single-plane scattering is calculated in a basis of spherical harmonics. Convergence of the transmission and reflection of a single plane is then monitored as a function of a cut-off on the number of spherical waves. Coupling of scattering planes is then established in the plane wave basis which includes all propagation and a first few evanescent modes.<sup>45</sup> The convergence of the transmission and reflection in the crystal case is then monitored as a function of the number of the plane-wave modes. This scheme has resulted in a very efficient and precise computational method, which since the early seventies of the last century has also been known as the low-energy-electron-diffraction theory (LEED). The unique feature of the MST is that, for nonoverlapping (muffin-tin) scatterers<sup>47</sup> (the present situation), it disentangles single-scattering and multiple-

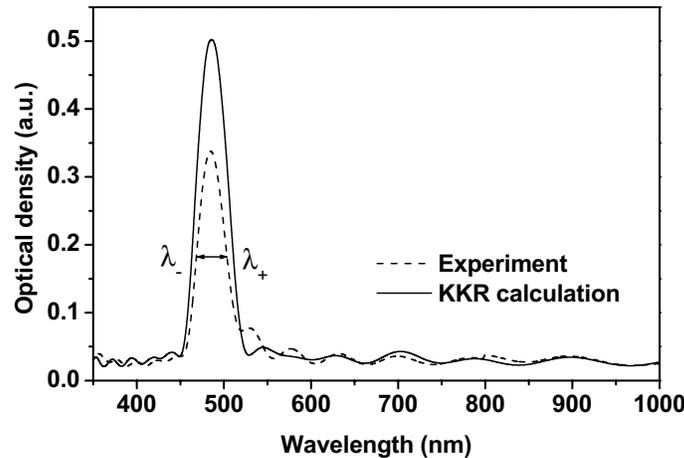


**Figure I.5–1** Comparison between theory and experiment for a thirteen-layer thick *fcc* photonic crystal of SiO<sub>2</sub> spheres ( $R = 110$  nm). The experimental optical density spectrum (dashed line) is taken along the (111) crystallographic axis. The theoretical spectrum was calculated using the KKR method.

scattering effects. Unlike the familiar plane-wave<sup>19</sup> and transfer-matrix methods,<sup>48</sup> the layer KKR uses an exact Mie solution<sup>49</sup> to take into account the single sphere scattering.<sup>44</sup> Another significant advantage of the layer KKR method is that the frequency dependence of the dielectric constant, important for metallo-dielectric PCs, can be easily implemented into the formalism and does not cost any extra computational time. Figure I.5–1 shows an example of an experimentally determined optical density spectrum (OD),  $OD = -\log(\text{Transmission})$ , compared to a theoretical spectrum calculated using the KKR method. The relative L-gap width at half-maximum,  $g_w$ , is given by  $g_w = 2(\lambda_+ - \lambda_-)/(\lambda_+ + \lambda_-)$ . The position of the gap and interference ripples is well predicted by the theory.

## I.6 This Thesis

This thesis describes the preparation and optical characterization of photonic crystals made of colloidal particles.

The first part of the thesis deals with photonic crystals of dielectric core-shell particles. In Chapter II.1 we demonstrate the synthesis and optical characterization of core-shell colloidal particles and hollow shells of ZnS and SiO<sub>2</sub>.

In Chapter II.2 we demonstrate, through use of the controlled drying method, the growth of large colloidal photonic crystals of SiO<sub>2</sub>, ZnS, and ZnS-core-SiO<sub>2</sub>-shell particles. We demonstrate, both experimentally and theoretically, that the relative

stop gap width in the (111) *fcc* crystallographic direction in the case of high-index core low-index shell particles is larger than in a crystal of homogeneous particles of either material.

The second part of the thesis describes the preparation and characterization of metallo-dielectric colloidal photonic glasses and crystals of silver (Ag). In Chapter III.1 we demonstrate the synthesis and optical characterization of large silver particles obtained by reduction of silver nitrate by ascorbic acid in aqueous solutions in the presence of a protective polymer.

In Chapter III.2 we study the optical properties of metallo-dielectric photonic crystals and photonic glasses of colloidal Ag particles dispersed in water formed by sedimentation in gravity.

The last part of the thesis deals with photonic crystals of complex lattices and shape-anisotropic particles. In Chapter IV.1 we present the fabrication of binary colloidal crystals through a simple layer-by-layer drying process. By using spheres with different composition, one component can be selectively removed. As an example we demonstrate the synthesis of a hexagonal non-close-packed colloidal crystal.

In Chapter IV.2 we demonstrate the fabrication of photonic crystals of ellipsoidally-shaped colloidal particles. Using high-energy ion irradiation, we deformed spheres organized in a thin 3D colloidal crystal into oblate ellipsoids. The optical properties of the irradiated crystals are modified as a result of the changed crystal lattice structure and shape of the building blocks.

---

## References

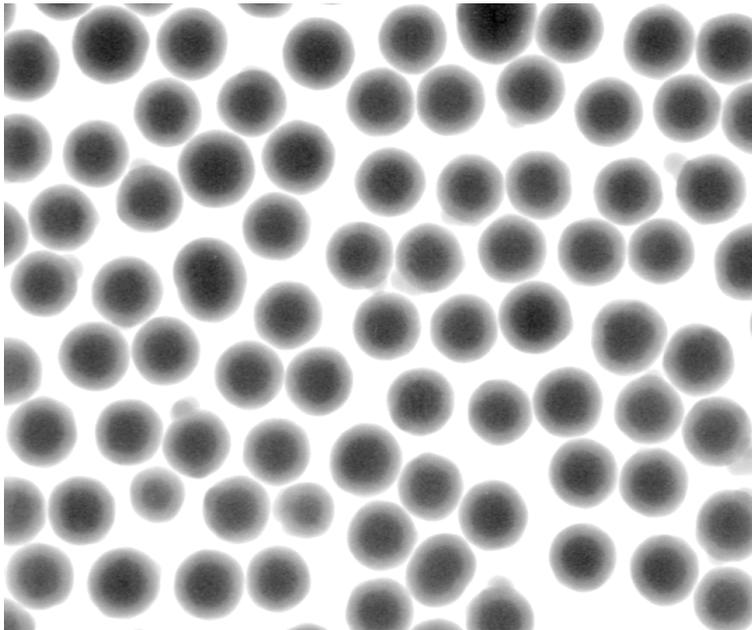
- (1) Joannopoulos, J. D.; Meade, R. D.; Winn, J. N. *Photonic Crystals*; Princeton Univ. Press: Princeton, 1995.
- (2) Soukoulis, C. M. *Photonic Band Gap Materials*; Kluwer Academic Publishers: Dordrecht, 1996.
- (3) Vos, W. L.; Sprik, R.; van Blaaderen, A.; Imhof, A.; Lagendijk, A.; Wegdam, G. H. *Phys. Rev. B* **1996**, *53*, 16231.
- (4) Sprik, R.; van Tiggelen, B. A.; Lagendijk, A. *Europhys. Lett.* **1996**, *35*, 265.
- (5) Krauss, T. F.; De la Rue, R. M. *Prog. Quantum Electron.* **1999**, *23*, 51.
- (6) Joannopoulos, J. D.; Villeneuve, P. R.; Fan, S. H. *Nature* **1997**, *386*, 143.
- (7) Soukoulis, C. M. *Photonic crystals and light localization in the 21th century*; Kluwer Academic Publishers: Dordrecht, 2001; Vol. C 563.
- (8) See the special issues: Material science aspects of photonic crystals. *MRS Bulletin*, **2001**, *26*; Photonic crystals. *Advanced Materials*, **2001**, *13*.
- (9) Colvin, V. L. *MRS Bull.* **2001**, *26*, 637.
- (10) Wijnhoven, J.; Vos, W. L. *Science* **1998**, *281*, 802.
- (11) Vlasov, Y. A.; Bo, X. Z.; Sturm, J. C.; Norris, D. J. *Nature* **2001**, *414*, 289.
- (12) Sozuer, H. S.; Haus, J. W.; Inguva, R. *Phys. Rev. B-Condens Matter* **1992**, *45*, 13962.
- (13) Pan, G. S.; Kesavamoorthy, R.; Asher, S. A. *Phys. Rev. Lett.* **1997**, *78*, 3860.
- (14) van Blaaderen, A. *MRS Bull.* **1998**, *23*, 39.

- (15) Moroz, A.; Sommers, C. *J. Phys.-Condes. Matter* **1999**, *11*, 997.
- (16) Moroz, A. *Phys. Rev. Lett.* **1999**, *83*, 5274.
- (17) Zhang, W. Y.; Lei, X. Y.; Wang, Z. L.; Zheng, D. G.; Tam, W. Y.; Chan, C. T.; Sheng, P. *Phys. Rev. Lett.* **2000**, *84*, 2853.
- (18) Chan, C. T.; Zhang, W. Y.; Wang, Z. L.; Lei, X. Y.; Zheng, D. G.; Tam, W. Y.; Sheng, P. *Physica B* **2000**, *279*, 150.
- (19) Ho, K. M.; Chan, C. T.; Soukoulis, C. M. *Phys. Rev. Lett.* **1990**, *65*, 3152.
- (20) Moroz, A. *submitted* **2001**.
- (21) Soukoulis, C. M. *Photonic Crystals and Light Localization*; Kluwer Academic Publishers: Dordrecht, 2000; Vol. 315.
- (22) Moroz, A. *Europhys. Lett.* **2000**, *50*, 466.
- (23) Noda, S.; Yokoyama, M.; Imada, M.; Chutinan, A.; Mochizuki, M. *Science* **2001**, *293*, 1123.
- (24) Snoeks, E.; van Blaaderen, A.; van Dillen, T.; van Kats, C. M.; Brongersma, M. L.; Polman, A. *Adv. Mater.* **2000**, *12*, 1511.
- (25) Pieranski, P. *Contemp. Phys.* **1983**, 25.
- (26) Jiang, P.; Bertone, J. F.; Colvin, V. L. *Science* **2001**, *291*, 453.
- (27) Jiang, P.; Bertone, J. F.; Hwang, K. S.; Colvin, V. L. *Chem. Mater.* **1999**, *11*, 2132.
- (28) van Blaaderen, A.; Ruel, R.; Wiltzius, P. *Nature* **1997**, *385*, 321.
- (29) Gates, B.; Qin, D.; Xia, Y. N. *Adv. Mater.* **1999**, *11*, 466.
- (30) Yin, Y. D.; Xia, Y. N. *Adv. Mater.* **2001**, *13*, 267.
- (31) Vos, W. L.; Megens, M.; van Kats, C. M.; Bosecke, P. *J. Phys.-Condes. Matter* **1996**, *8*, 9503.
- (32) Tarhan, II; Watson, G. H. *Phys. Rev. Lett.* **1996**, *76*, 315.
- (33) Tao, R.; Sun, J. M. *Phys. Rev. Lett.* **1991**, *67*, 398.
- (34) Murray, M. J.; Sanders, J. V. *Nature* **1978**, *275*, 201.
- (35) Hachisu, S.; Yoshimura, S. *Nature* **1980**, *283*, 188.
- (36) Bartlett, P.; Ottewill, R. H.; Pusey, P. N. *Phys. Rev. Lett.* **1992**, *68*, 3801.
- (37) Trau, M.; Saville, D. A.; Aksay, I. A. *Science* **1996**, *272*, 706.
- (38) Hayward, R. C.; Saville, D. A.; Aksay, I. A. *Nature* **2000**, *404*, 56.
- (39) de Hoog, E. H. A.; de Jong-van Steensel, L. I.; Snel, M. M. E.; van der Eerden, J.; Lekkerkerker, H. N. W. *Langmuir* **2001**, *17*, 5486.
- (40) Denkov, N. D.; Velev, O. D.; Kralchevsky, P. A.; Ivanov, I. B.; Yoshimura, H.; Nagayama, K. *Langmuir* **1992**, *8*, 3183.
- (41) Park, S. H.; Qin, D.; Xia, Y. *Adv. Mater.* **1998**, *10*, 1028.
- (42) Denkov, N. D.; Velev, O. D.; Kralchevsky, P. A.; Ivanov, I. B.; Yoshimura, H.; Nagayama, K. *Nature* **1993**, *361*, 26.
- (43) Kralchevsky, P. A.; Denkov, N. D. *Curr. Opin. Colloid Interface Sci.* **2001**, *6*, 383.
- (44) Stefanou, N.; Yannopapas, V.; Modinos, A. *Comput. Phys. Commun.* **1998**, *113*, 49.
- (45) McRae, E. G. *Surf. Sci.* **1968**, 479.
- (46) Kambe, K. *Z. Naturforschg.* **1967**, *22a*, 42.
- (47) Beeby, J. L. *J. Phys.-Condes. Matter* **1968**, *1*, 82.
- (48) Pendry, J. B. *J. Phys.-Condes. Matter* **1996**, *8*, 1085.
- (49) Bohren, C. F.; Huffman, D. R. *Absorption and scattering of light by small particles*; Wiley: New York, 1983.



## Part II

# Photonic Crystals of Dielectric Core-Shell Colloidal Particles





---

## II.1 Synthesis and Characterization of Monodisperse Core-Shell Colloidal Spheres of Zinc Sulfide and Silica

We report on a new type of composite particles consisting of a zinc sulfide (ZnS) core and a silica (SiO<sub>2</sub>) shell or vice versa. We developed and optimized these particles for photonic applications, because ZnS has a large refractive index and does not absorb light in the visible and both ZnS and SiO<sub>2</sub> can be easily doped with fluorophores. Both kinds of morphologies were created using a seeded growth procedure using monodisperse seeds on which homogeneous layers with a well-defined thickness were grown. Moreover, the ZnS and SiO<sub>2</sub> cores could be completely dissolved leaving SiO<sub>2</sub> and ZnS shells, respectively, filled with solvent or air after drying. The particle morphology was investigated by electron microscopy. The optical properties were studied by extinction measurements and angle resolved light scattering and compared to scattering theory.

## Introduction

Recently, a lot of interest in core-shell colloidal particles has arisen from the ability to fine-tune their properties. The structure, size and composition of these particles can be easily altered in a controllable way to tailor their magnetic, optical, mechanical, thermal, electrical, electro-optical, and catalytic properties.<sup>1-7</sup> Core-shell particles with a shell optically matched to the suspending fluid can be employed as a model system to study direct particle-particle interactions in a fluid or a colloidal crystal.<sup>8</sup> The core-shell morphology can be used as a precursor form to produce hollow spheres<sup>9</sup> or to lower the cost of precious materials by coating them on inexpensive cores.<sup>10,11</sup>

An exciting area of application of colloidal particles is that of photonic bandgap materials.<sup>12-14</sup> These materials can be used for the manipulation of light propagation and spontaneous emission.<sup>15-17</sup> Colloids are ideal building blocks for the creation of photonic crystals, because of their ability to self-organize in three-dimensional (3D) periodic structures with different symmetries. Core-shell particles consisting of high-index core (e.g., ZnS) and low-index shell (e.g., SiO<sub>2</sub>), or vice versa, are of special interest.<sup>13</sup> By changing the thickness of the shell with respect to the core, one can tune the filling fraction of the components and control the optical properties. Further, the cores can be dissolved to obtain a crystal or single particles of hollow shells of high or low-index material.

Zinc sulfide (ZnS) is a widely used metal sulfide with many technological applications (e.g., as pigment,<sup>18</sup> in electroluminescence panels,<sup>19</sup> infrared-windows,<sup>20</sup> and solar cells<sup>21</sup>). ZnS colloidal particles of different size and low polydispersity can be obtained by a homogeneous precipitation and aggregation process.<sup>22-25</sup> Due to the high bulk refractive index ( $n \sim 2.36$  ( $\lambda = 589$  nm) for cubic  $\beta$ -ZnS) and lack of absorption in the visible,<sup>26</sup> ZnS is an appropriate material for photonic applications, such as optical cavities and photonic crystals. Moreover, ZnS can be doped, e.g., with manganese,<sup>27</sup> to induce luminescence or a fluorescent dye can be incorporated into the silica layer at a well-defined radial position.<sup>28</sup> Recent theoretical calculations have shown that a face-cubic-centered (*fcc*) colloidal crystal of ZnS-core-SiO<sub>2</sub>-shell particles with a suitable shell thickness has a larger relative L-stopgap in comparison to a crystal of homogeneous ZnS or SiO<sub>2</sub> spheres.<sup>29</sup> In addition, the relative L-stopgap is also larger than in the case of a crystal from SiO<sub>2</sub>-core-ZnS-shell particles or even hollow ZnS-shells.<sup>30</sup>

Coating of colloidal particles with a silica layer has many advantages, because such a shell is chemically inert and optically transparent. Furthermore, the colloid chemistry of silica is well understood<sup>31</sup> and many possibilities for surface modification are available. Finally, coating by silica in a seeded growth process<sup>32-34</sup> leads to a decrease in the polydispersity of the particles and reduces the van der Waals

attraction, which enhances the colloid stability and ability to form colloidal crystals. A silica coating has already been applied to CdS<sup>35</sup> and ZnS<sup>36</sup> semiconductor nanocrystals, metal,<sup>5,37-42</sup> inorganic,<sup>8,43</sup> and polymer<sup>44</sup> colloidal particles. The thin silica layer increases the mechanical stability, makes possible a transfer into organic solvents, provides for a capping layer on the semiconductor nanocrystals, and protects metal particles against oxidation. Finally, we recently invented a way to turn the spherical SiO<sub>2</sub> and ZnS particles into ellipsoidal particles by ion irradiation.<sup>45</sup>

In this Chapter, we will describe the coating of ZnS colloidal particles of different sizes with a SiO<sub>2</sub> layer, and vice versa, using seeded growth procedures. ZnS and SiO<sub>2</sub> cores were completely dissolved leaving SiO<sub>2</sub> and ZnS shells, respectively, filled with solvent. The optical properties of the particles were studied by means of static light scattering (SLS) and extinction measurements, and compared with scattering theory.

## Experimental Section

**Materials.** Zn(NO<sub>3</sub>)<sub>2</sub>·4H<sub>2</sub>O, ammonia (30 wt % NH<sub>3</sub>), and nitric acid of analytical reagent quality were purchased from Merck, fluorescein–isothiocyanate (FITC, isomer I) was purchased from Sigma, and thioacetamide (TAA), hydrofluoric acid (HF), and tetraetoxysilane (TES) of puriss grade quality were obtained from Fluka. Absolute technical grade ethanol (Nedalco) or analytical grade ethanol (Merck), and Milli-Q water were used in all preparations. All solvents and chemicals were used as received.

**Particle Characterization.** Transmission electron microscopy (TEM) and scanning electron microscopy (SEM) were carried out on Philips CM10 and Philips XL30 FEG microscopes, respectively. The relative width of the size distribution (the polydispersity  $\delta$ ), defined as the ratio between the standard deviation and the mean particle size, was determined by image processing; typically around 200 particles were counted. Static light scattering (SLS) measurements on dilute suspensions in ethanol were performed on a Fica 50 or a homemade light scattering apparatus. Extinction spectra were measured in ethanol using a Cary 100E UV-Vis spectrophotometer. The optical path in the suspension was 1.00 cm. Suspensions were sufficiently diluted ( $< 10^{-5}$  vol. %) to avoid interactions between particles and to keep multiple scattering contributions negligible. Fitting of the spectra was performed using the computer algorithm developed by Bohren and Huffman,<sup>46</sup> adapted to take size polydispersity into account.

**Silica Core Synthesis.** Monodisperse SiO<sub>2</sub> particles were synthesized following the Stöber-Fink-Bohn procedure.<sup>47</sup> A fluorescent dye (FITC) was incorporated into the silica spheres as described by van Blaaderen *et al.*<sup>28</sup>

**ZnS Core Synthesis.** Zinc sulfide colloidal particles of different sizes were obtained by homogeneous precipitation-aggregation from acidic zinc nitrate aqueous

solutions using the thermal decomposition of TAA as a source of sulfide ions.<sup>22,24,25,48</sup> Typical starting conditions used in our experiments were 0.001–0.05 M  $\text{Zn}^{2+}$ , 0.01–0.10 M  $\text{HNO}_3$ ,  $[\text{Zn}^{2+}]/[\text{TAA}] = 4\text{--}10$ , and a constant temperature in the range of 60–70°C. The TAA was first dissolved in water, and the solution was heated to the reaction temperature; then, a mixture of  $\text{Zn}(\text{NO}_3)_2$  and  $\text{HNO}_3$  solution was quickly added, and the reaction vessel was immersed in a water bath set at the reaction temperature. The precipitation reaction was carried out in two stages because this turned out to provide more monodisperse particles. In the first stage a population of particles was obtained as described above and in the literature.<sup>22,24,25,48</sup> However, in some experiments, following Wilhelmy and Matijevic,<sup>22</sup> the solution was first kept at room temperature for 5 h, and then placed in the water bath at an elevated temperature. After a certain period of aging, in which the primary particles reached the desired radius, the precipitation reaction was quenched by cooling the vessel in cold water ( $\sim 15^\circ\text{C}$ ) accompanied by vigorous agitation. The decrease in temperature and the mechanical agitation led to a secondary nucleation. In some cases, the first population of big particles was separated from the solution by centrifugation. The mother liquor with the second population of nuclei was placed again in the warm water bath and the reaction continued, until the secondary particles reached the desired size. The final radius of the particles was controlled by the heating time, which ranged from 30 min to 3 h. The particles were separated from the mother liquid by centrifugation, washed twice with water, and redispersed in ethanol by ultrasonification. Suspensions were stored and remained stable in ethanol.

**Coating of ZnS Cores with  $\text{SiO}_2$ .** A direct coating of the ZnS particles with a silica layer was performed in two steps, based on a modification of the original Stöber method<sup>47</sup> to seeded growth.<sup>32-34</sup> In the first step, concentrated ammonia (30 wt. %  $\text{NH}_3$ ) was added to a vigorously stirred ZnS suspension in ethanol (with a particle concentration  $n$  of  $\sim 10^9 \text{ cm}^{-3}$ ) to a concentration of 0.10 M in  $\text{NH}_3$ . Subsequently, a certain amount of TES was added. Some of the experiments were performed with an additional amount of water added to a total concentration of 1.00 M. The amount of TES was calculated to cover the particle with a silica layer of thickness  $\sim 50 \text{ nm}$ . Typically, when no additional amount of water was added the condensation of TES was slow and took more than 5 hours.<sup>34</sup> In the second step, the ammonia concentration was increased to 0.60 M, and the water concentration was adjusted to 2.00 M. The TES was added in small portions, in order to prevent a secondary nucleation of pure silica particles.<sup>32</sup> The final core-shell particles were separated by centrifugation, washed twice with ethanol, and then redispersed by ultrasonification in pure ethanol.

**$\text{SiO}_2$  Shells.** Hollow silica shells were obtained after dissolving the ZnS cores using a mineral acid. Typically, 0.001 M nitric acid was added to a dilute ( $< 0.1 \text{ vol. \%}$ ) water (50 vol. %) – ethanol (50 vol. %) suspension of ZnS-core- $\text{SiO}_2$ -shell particles

at moderate stirring. A higher acid concentration induced aggregation. For a ZnS core of radius  $\sim 125$  nm, the dissolution process was carried out for 24 h. Depending on the core-shell particle morphology, SiO<sub>2</sub> shells filled with solvent or a silica replica of the pores in the ZnS cores was obtained.

**Coating of SiO<sub>2</sub> Cores with ZnS.** SiO<sub>2</sub>-core-ZnS-shell particles were obtained by homogeneous precipitation of ZnS onto silica seeds in water-ethanol solutions using the thermal decomposition of TAA as a source of sulfide ions. The same concentration range of Zn<sup>2+</sup>, HNO<sub>3</sub>, and [Zn<sup>2+</sup>]/[TAA] ratio as for producing of the ZnS cores was used. An ethanol suspension of fluorescently labeled SiO<sub>2</sub> seeds of radius  $\sim 202$  nm ( $n \sim 10^{10}$  cm<sup>-3</sup>) was mixed with an equal volume of water containing the dissolved TAA. Then, the mixture of Zn<sup>2+</sup> and HNO<sub>3</sub> was quickly added, and the reaction vessel was placed in a water bath at 60°C. The reaction was carried out for 2–3 hours at slow stirring. The final particles were separated by centrifugation, washed twice with ethanol, and then redispersed by ultrasonification in pure ethanol. As in the case of pure ZnS particles, suspensions were stored and remained stable in ethanol.

**ZnS-Shells.** Solvent filled ZnS shells were obtained after dissolving the SiO<sub>2</sub> cores using hydrofluoric acid. Typically, 1 wt. % HF in water was added to a dilute ( $< 0.1$  vol. %) suspension of SiO<sub>2</sub>-core-ZnS-shell particles in ethanol at moderate stirring. Silica cores were dissolved within  $\sim 5$  min. The ZnS shells did not dissolve within the reaction time and remained as hollow shells.

## Results and Discussion

**ZnS Cores.** By use of the above-described procedure, spherical ZnS particles with a narrow size distribution ( $\delta < 8\%$ ) were obtained. The final particle radius, depending on the reaction time and conditions, varied from 80 nm up to 1.4  $\mu$ m (Table II.1–1). Examples of electron micrographs of ZnS cores demonstrating the range of sizes obtained with the method are shown in Fig. II.1–1. The particles were prepared using different experimental conditions, but in all cases the particle size was controlled through the reaction time. The mechanism of ZnS precipitation-aggregation and particle morphology are well understood.<sup>48,49</sup> The ZnS particles are aggregates consisting of small ( $\sim 10$  nm) nanocrystals mainly of cubic  $\beta$ -ZnS. The crystalline structure and crystal size were inferred from X-ray diffraction measurements.<sup>24,49</sup> Because of the aggregation mechanism, ZnS particles are porous and consist of  $\sim 50 - 80\%$  ZnS.<sup>18</sup> The porosity and the average density depend on the particle size and reaction conditions and light scattering results discussed below indicate that the larger particles do not have a homogeneous density distribution. Polydispersity is an important parameter if colloidal particles are used as a model system to study crystallization, melting, or the glass transition.<sup>50</sup> In contrast to previously reported results,<sup>22,23</sup> a significantly lower polydispersity was achieved

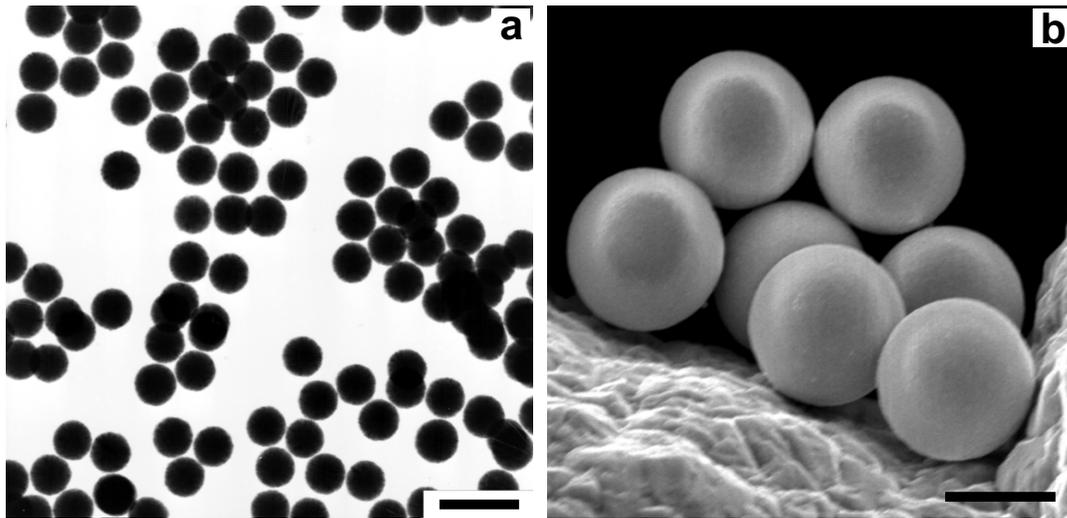


**Figure II.1-1** Transmission (TEM **a**) and scanning (SEM **b**) electron micrographs of spherical monodisperse ZnS particles obtained through homogeneous precipitation-aggregation from aqueous solutions of zinc nitrate demonstrating the range of sizes possible: (**a**) Sample 55SN,  $R = 103$  nm,  $\delta = 3\%$ , scale bar 400 nm; (**b**) Sample 13,  $R = 1.414$   $\mu\text{m}$ ,  $\delta = 1\%$ , scale bar 2  $\mu\text{m}$ . The size and polydispersity were determined by TEM.

without additional purification of the TAA. In general, the polydispersity was below 8%, but in some cases in which a low initial  $\text{Zn}^{2+}$  concentration was used, a polydispersity of  $\sim 1\%$  was reached (Fig. II.1-1b). The initial and the secondary nucleation influence the final size distribution of ZnS. The nucleation process is very sensitive to impurities and thermal or mechanical fluctuations. The secondary nucleation is caused by an excess of  $\text{Zn}^{2+}$  and  $\text{S}^{2-}$  ions, which were not consumed during the primary particle growth. The secondary particles were generally observed to have a lower polydispersity and higher concentration. A possible explanation is that the secondary nucleation takes place in a more homogeneous medium and at a higher concentration of  $\text{S}^{2-}$  in the solution. The higher concentration of sulfide ions in the solution leads to a higher concentration of nuclei. A secondary nucleation could both be induced by agitation or cooling the reaction vessel. Once generated, the secondary particles were further grown to a desired size. The main disadvantage of the method is the difficult control over the final particle size. However, by use of seeded growth (see below) this problem is overcome. The stability of an aqueous ZnS suspension has been studied in detail,<sup>51,52</sup> but to our knowledge no data are available on stability in organic solvents. It is our finding that ZnS particles of any size form a stable suspension in ethanol, where they were kept before coating with silica.

**ZnS-core-SiO<sub>2</sub>-shell.** ZnS seeds were directly coated with a silica layer of the desired thickness by hydrolysis and condensation of TES in an ethanol-water-ammonia mixture. The most important factor in the coating process is the stability of

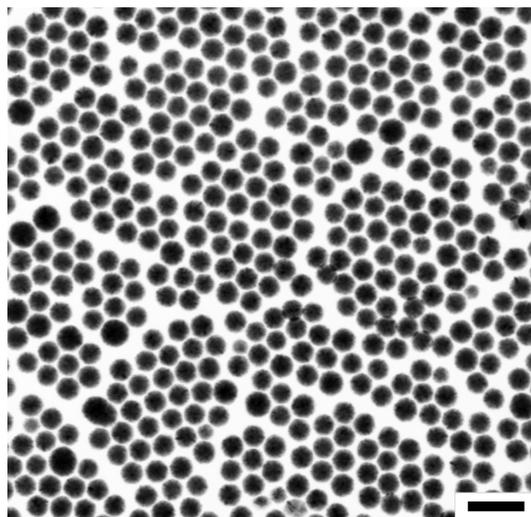


**Figure II.1-2** A TEM micrograph of ZnS-SiO<sub>2</sub> composite cores (sample 56SN-S1), radius  $R = 84$  nm ( $\delta = 6\%$ ) obtained after deposition of silica inside the ZnS pores. The size and polydispersity were determined by TEM. The presence of silica was detected by light scattering through an increase in the effective refractive index. The scale bar is 400 nm.

the initial seed suspension at the reaction conditions. By use of a concentration of 0.10 M of ammonia, particles of different size were initially coated with a very thin silica layer without aggregation. Table II.1-2 gives examples of coated ZnS cores with silica with different thickness and morphology. A ZnS colloidal suspension was found to be stable at 0.10 M NH<sub>3</sub> (0.22 M H<sub>2</sub>O) in a water-ethanol-ammonia mixture; however, at higher concentrations of ammonia (used for seeded growth of pure silica spheres<sup>32,34</sup>) the ZnS cores aggregated. At a pH higher than the isoelectric point (IEP = 7.2<sup>53,54</sup>), ZnS is negatively charged due to the presence of HS<sup>-</sup> and negatively charged hydrolysis products on the particle surface. However, as we did not prevent the presence of oxygen, it is likely that the outside layer is composed of ZnO.<sup>51,52</sup> In principle, this facilitates the growth of SiO<sub>2</sub> on the particle surface. As surface oxidation is quite common for many sulfides, this suggests that coating of large colloidal particles of metal sulfides with a silica layer is generally possible.

The deposited silica layer has a different morphology depending on the ZnS particle porosity and reaction conditions. If the particles are small and porous (< 200 nm), the initial silica is first deposited inside the particle pores forming a ZnS-silica composite core (Fig. II.1-2). The very thin silica layer cannot be determined by TEM initially, but the light scattering experiments clearly show a change in the effective refractive index of the particles due to the presence of silica inside the pores without a significant change in size. However, after dissolving the ZnS the silica remains and can be directly imaged by TEM (see below). In this way, the silica can provide for

mechanical stabilization of small and porous aggregates of metal sulfides. If the particles are bigger or the coating is performed at higher water concentration (higher hydrolysis rate of TES), silica cannot diffuse deep into the particle and quickly forms a layer leading to core-shell particles (Fig. II.1–3).

**Table II.1–1 Radius ( $R$ ) and polydispersity ( $\delta$ ) of ZnS cores obtained after a secondary or primary nucleation burst (see text) as determined by TEM.**

Sample code	$R$ (nm)	$\delta$ (%)	Nucleation burst
50SN	81	8	secondary
56SN	84	5	secondary
55SN	103	3	secondary
57SN	133	6	secondary
32	270	9	primary
54SN	346	6	secondary
61SN	818	7	secondary
13	1415	1	primary

**Table II.1–2 Radius ( $R$ ) and polydispersity ( $\delta$ ) of ZnS-SiO<sub>2</sub> composite and ZnS-core-SiO<sub>2</sub>-shell particles obtained after a seeded coating of ZnS cores with silica as determined by TEM.**

Sample code	$R$ (nm)	$\delta$ (%)	Morphology <sup>a</sup>
56SN-S1	85	6	composite
56SN-S1-S	128	5	core-shell
57SN-S1	125	5	composite
50SN-S1	81	8	composite
50SN-S1-S	245	6	core-shell
50SN-S1-S1	338	4	core-shell
54SN-S3-S	351	5	core-shell

<sup>a</sup> ‘Composite’ means that the silica penetrates into the ZnS core.

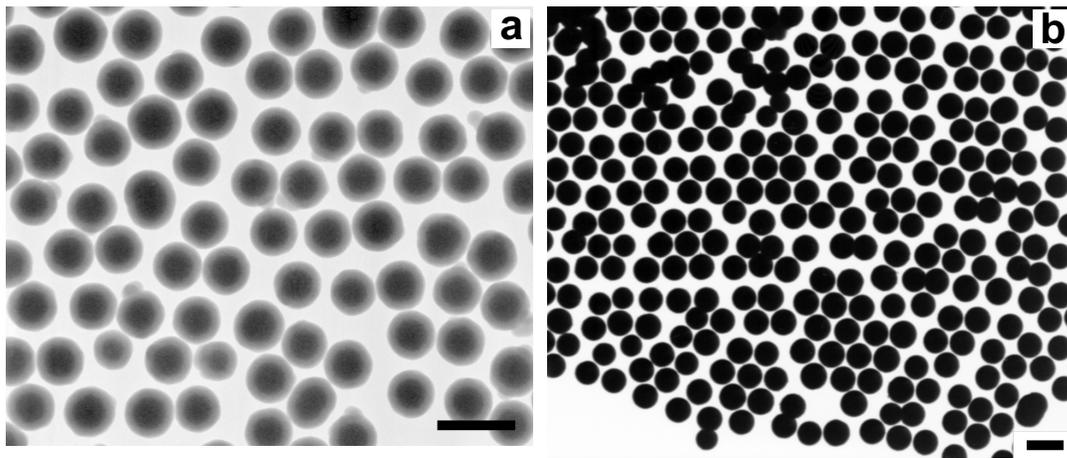


**Figure II.1-3** TEM micrographs of ZnS-core-SiO<sub>2</sub>-shell particles of different core-to-shell ratio and total size ( $R$ ): (a) sample 56SN-S1-S, core radius  $R_c = 84$  nm, total radius  $R = 128$  nm,  $\delta = 5\%$ , scale bar 400nm; (b) sample 54SN-S3, core radius  $R_c = 346$  nm, total radius  $R = 351$  nm,  $\delta = 4\%$ , scale bar 1  $\mu\text{m}$ . The size and polydispersity were determined by TEM.

The conditions necessary to stabilize the ZnS suspension are not optimal to grow silica.<sup>32,34</sup> For this reason, the ammonia concentration was increased to 0.6 M only after the first thin silica layer was deposited. At this ammonia concentration, the silica layer can be continuously grown to a desired thickness (Table II.1-2). If the ZnS core radius is not too large ( $< 200$  nm using 100 keV), the silica shell can be directly observed by TEM (Fig. II.1-3a) because not all electrons used in the imaging are stopped by the particle and there is an appreciable density difference between silica ( $\sim 2.0$  g/cm<sup>3</sup><sup>34</sup>) and ZnS (4.0 g/cm<sup>3</sup><sup>55</sup>). If the particles are larger than

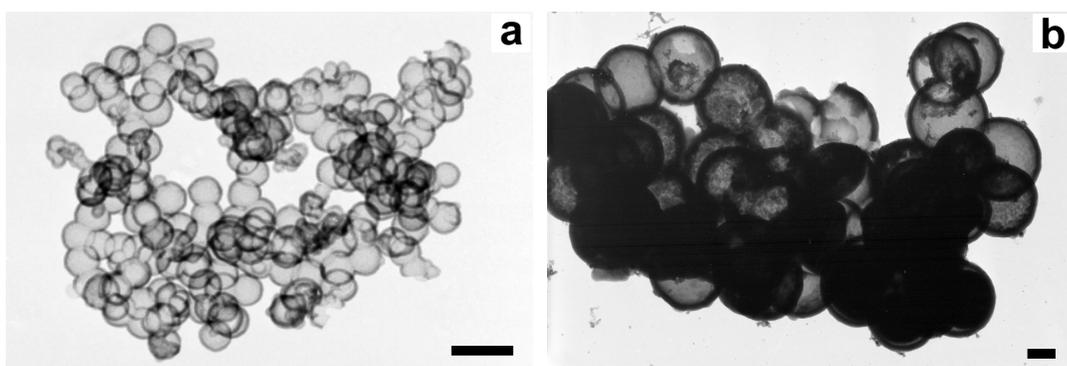


**Figure II.1-4** TEM micrographs of hollow silica shells obtained after dissolution of the ZnS cores: (a) shell thickness 17 nm with an internal radius of 60 nm; (b) shell thickness 50 nm with an internal radius of 260 nm. The scale bars are 200 nm.

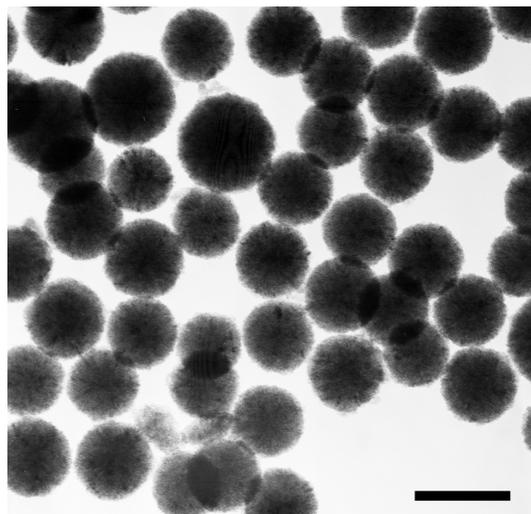


**Figure II.1-5** TEM micrographs of silica replicas obtained after dissolution of the ZnS from the ZnS-SiO<sub>2</sub> composite cores (sample 50SN-S1). The internal morphology of the pores can be seen inside the silica structure. The scale bar is 200 nm.

~ 200 nm, the silica shell can be discerned indirectly because the surface has become smoother (Fig. II.1-3b), by light scattering measurements, or after dissolving the ZnS cores.

**SiO<sub>2</sub> Shells.** It has been shown that the silica layer, created by the Stöber syntheses, is porous with a pore size about 3 Å.<sup>56</sup> This size is sufficiently large to allow free diffusion of Zn<sup>2+</sup> and S<sup>2-</sup> ions across the silica layer. Using this fact, we successfully dissolved the ZnS core using a dilute solution of nitric acid to increase the solubility and obtained hollow silica particles. Figure II.1-4 shows a collection of hollow silica shell particles. The ZnS cores were removed by dissolution with 0.001 M HNO<sub>3</sub> in a water-ethanol mixture. Acid solutions with a pH > 3 should be used to prevent aggregation of the silica shells. The ZnS core is accessible to the acid ions even through a ~ 50 nm thick silica layer (Fig. II.1-4b). The thickness of the silica layer of empty shells can be measured directly by TEM after dissolution of the ZnS core. Dissolution of the ZnS from a small ZnS-silica composite sphere led to a silica replica of the porous structure of the initial particle (Fig. II.1-5). These replicas represent the internal structure of the ZnS core showing that ZnS particles are indeed porous.<sup>18</sup> Silica shells have interesting optical properties on a single particle level and can also be used to create dielectric defects<sup>57</sup> if incorporated in a colloidal crystal of core-shell or homogeneous particles.

**SiO<sub>2</sub>-core-ZnS-shell.** It has been demonstrated that ZnS can be grown onto silica particles under similar conditions as ZnS cores by using H<sub>2</sub>S<sup>58</sup> or by sonification of a TAA solution.<sup>59</sup> In our experiments, we employed the thermal decomposition of TAA in an acidic water-ethanol mixture as a source of sulfide ions. Despite the fact

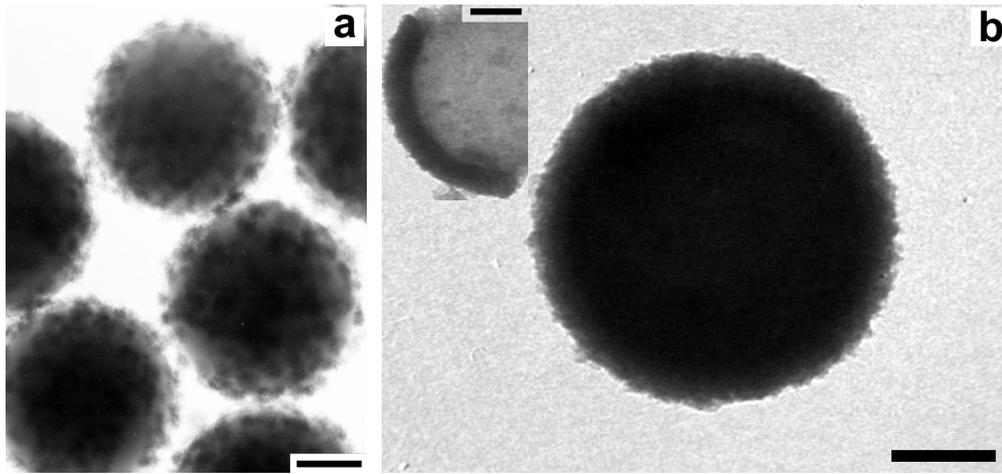


**Figure II.1-6** TEM micrographs of SiO<sub>2</sub>-core-ZnS-shell particles: (a) silica cores of radius 160 nm covered with an incomplete layer of ZnS nanocrystalline aggregates; (b) homogeneously coated silica seeds with a dense ZnS layer of thickness ~ 50 nm. The inset shows a broken ZnS shell. All scale bars are 100 nm.

that a low concentration ( $< 0.001$  M) of nitric acid was used to prevent aggregation of the suspension of SiO<sub>2</sub> seeds, the stability remained a problem. In all samples, a partial aggregation was found. Initially, ZnS forms irregularly shaped clusters composed of single nanocrystals crystals ( $\sim 1$ – $5$  nm) on the silica surface (Fig. II.1-6a). The aggregates are held together by an irregular porous network. These clusters grow further and form a complete shell of dense ZnS. Figure II.1-6b shows homogeneously coated core-shell particles. From broken ZnS shells, the thickness of the ZnS layer was estimated to be  $\sim 50$  nm. By showing the ability of growing both core-shell systems, we have control over the optical properties on a single particle level. These particles can be used to dielectrically dope photonic crystals<sup>57</sup> or grow inverse crystals from the shells.

**ZnS Shells.** Solvent-filled ZnS shells were obtained after dissolving the SiO<sub>2</sub> cores using hydrofluoric acid. Surprisingly, the ZnS shell did not dissolve or dissolved much slower than silica in ethanol solution of HF and remained as hollow shells. Figures II.1-7 shows TEM micrographs of hollow ZnS shells. In a comparison of the ZnS shell before and after dissolving the SiO<sub>2</sub>, it can be seen that the surface is smoother than in the case of the SiO<sub>2</sub>-core-ZnS-shell particle. This is an indication of a partial dissolution of the ZnS. However, an optimal dissolution time was not determined.

High dielectric hollow particles, such as ZnS shells, have interesting optical properties.<sup>10,11</sup> Until now, almost all inverse dielectric structures, that is, low dielectric spheres in an *fcc* arrangement in a high dielectric background, have been made by templating on an already formed crystal.<sup>60</sup> With our method individual hollow spheres are generated which can subsequently be crystallized. Starting with

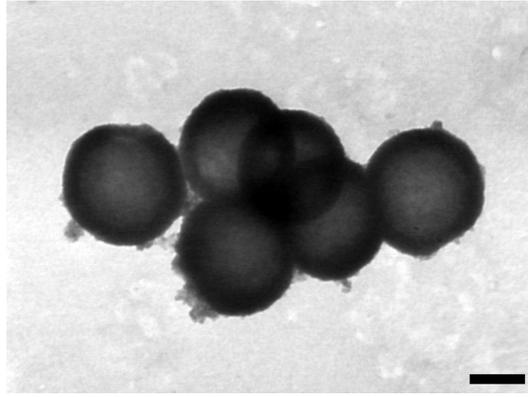


**Figure II.1-7** TEM micrographs of hollow ZnS shells obtained after dissolution of the silica cores by HF. The shell thickness is 50 nm with an internal radius of 160 nm. The scale bar is 200 nm.

individual shells gives more flexibility, however, if one wants to dope the lattice dielectrically or wants to grow more complex lattices, like body centered tetragonal<sup>61</sup> or binary lattices.<sup>62</sup>

**Optical Properties.** Because of the high refractive index of  $\beta$ -ZnS ( $n = 2.36$ <sup>26</sup> at  $\lambda = 589$  nm) and the size of the particles studied, a full solution of the Maxwell equations is necessary to quantitatively describe the light scattering of this system. Aden and Kerker derived an analytical solution for spherical core-shell particles.<sup>63</sup> The exact shape of the curves is sensitive to polydispersity, dielectric contrast and particle size. We performed both wavelength-dependent (extinction) and angle dependent (SLS) measurements on ZnS and ZnS-core-SiO<sub>2</sub>-shell particles only. The combination of both techniques gives a consistency check on the dielectric properties and structure obtained on the single particle level. All spectra were taken in the range above the absorption edge of bulk ZnS (350 nm).<sup>18</sup> The extinction efficiency (extinction cross section divided by cross-sectional area<sup>46</sup>) spectra and SLS spectra were calculated using scattering theory extended to the case of polydisperse particles assuming a Gaussian size distribution. In the case of core-shell particles, a Gaussian distribution was assumed in the core and an independent Gaussian distribution was assumed in the total particle radius.<sup>64</sup> Both distributions were measured by electron microscopy. The porous ZnS core cannot be represented with the refractive index of pure ZnS and requires a model. Fortunately, the ZnS nanocrystals are much smaller than the wavelength of light allowing a description of the particle by an effective dielectric constant of ZnS dispersed in a host of the solvent (or silica in the case of a composite ZnS-SiO<sub>2</sub> core). The effective dielectric constant was calculated using the Maxwell-Garnett effective medium approximation<sup>46</sup>

$$\frac{\epsilon_{eff} - \epsilon_s}{\epsilon_{eff} + 2\epsilon_s} = f \frac{\epsilon_{ZnS} - \epsilon_s}{\epsilon_{ZnS} + 2\epsilon_s},$$

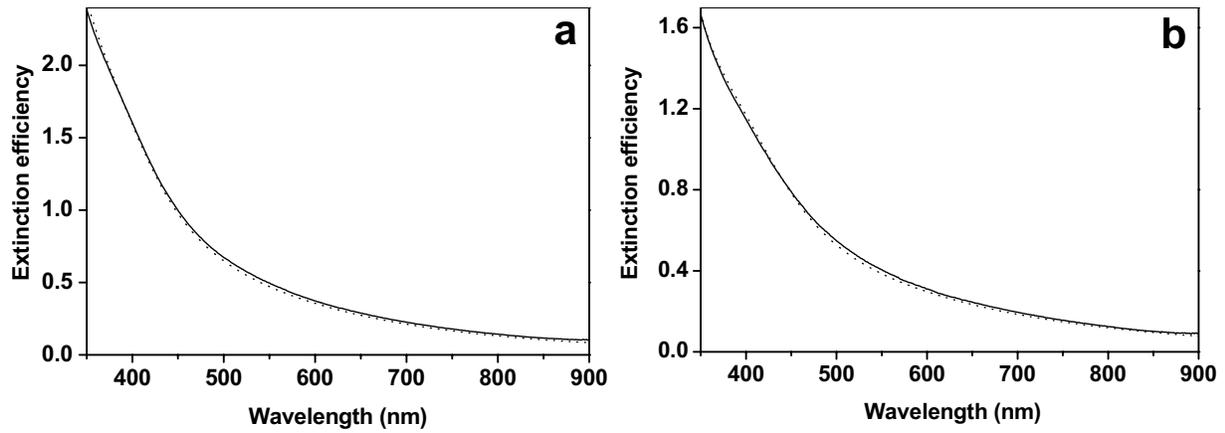


**Figure II.1-8** Experimental (solid line) and calculated (dotted line) extinction efficiency spectra: (a) ZnS cores (sample 56SN) of radius  $R_c = 84$  nm,  $\delta_c = 6\%$  (from TEM); (b) ZnS-core-SiO<sub>2</sub>-shell particles (sample 56SN-S1-S, Fig. II.1-3a), consisting of the same ZnS core, with total radius  $R = 128$  nm,  $\delta = 5\%$  (from TEM). The extinction efficiency spectra were calculated using the following parameters:  $R_c = 92$  nm,  $\delta_c = 5\%$ ,  $R = 128$  nm, and  $\delta = 5\%$ . The filling fraction of ZnS in both cases is 0.62 ( $n_{eff} = 1.92$  at  $\lambda = 589$  nm).

where  $f$  is the filling fraction of ZnS with a wavelength-dependent bulk dielectric constant  $\epsilon_{ZnS}$ .<sup>26</sup> The particle pores are filled with a second material (solvent or silica in the case of the ZnS-SiO<sub>2</sub> composite core) with a dielectric constant  $\epsilon_s$ . For the refractive index of silica ( $n = 1.450$ ) and the solvent (ethanol  $n = 1.361$ ), the wavelength dependence can be neglected. The most important fitting parameter obtained from the light scattering curves is the filling fraction of ZnS. Both the particle radii and polydispersity were varied as well, but the values taken were close to those determined from the electron microscopy.

In Fig. II.1-8, experimental and calculated extinction efficiency spectra of ZnS cores and the same cores coated with a  $\sim 44$  nm silica shell are shown. The best fit was determined with an accuracy of  $\pm 0.01$  in the filling fraction of ZnS ( $\pm 0.01$  in the refractive index) and  $\pm 2$  nm in the radius. In the case of core-shell particles, the core parameters were assumed to be the same and only the shell thickness was varied. A strong modulation of the scattering efficiency with wavelength, due to Mie resonances, was observed in large ZnS particles (Fig. II.1-9). The whispering gallery modes of the morphology-dependent resonances, averaged out in Fig. II.1-9a, can be observed only at low size polydispersity (Fig. II.1-9b). In general, the filling fraction of ZnS was determined to be in range of  $f = 0.60 - 0.80$ , which is in good agreement with previous results.<sup>18</sup> Angle resolved scattering (SLS) curves (Fig. II.1-10) were in agreement with the extinction curves (Fig. II.1-9a) and showed no indication of

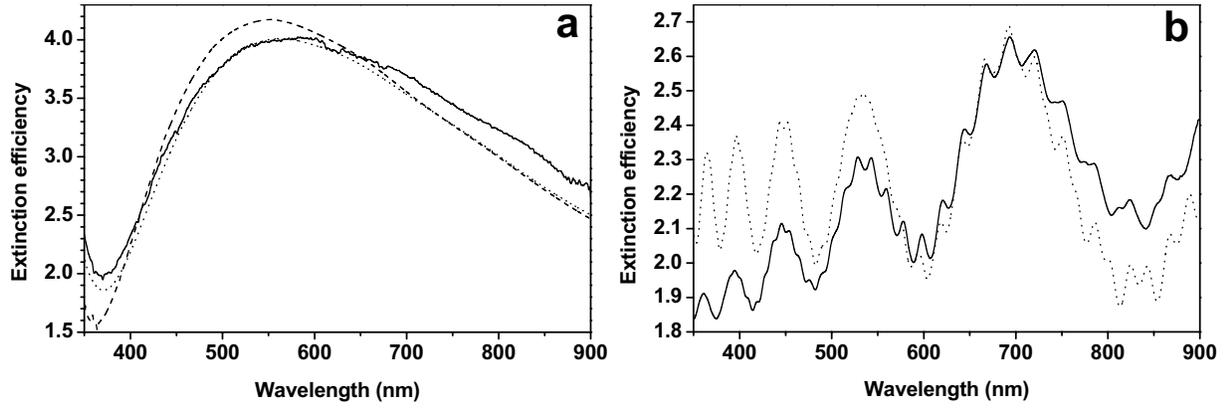


**Figure II.1-9** Experimental (solid line) and calculated (dotted line) extinction efficiency spectra: **(a)** ZnS particles (sample 54SN) of radius 346 nm and  $\delta = 6\%$  (from TEM). The extinction efficiency spectra were calculated using the following parameters:  $R = 350$  nm,  $\delta = 6\%$ , and ZnS filling fraction of  $f = 0.58$  ( $n_{\text{eff}} = 1.88$  at  $\lambda = 589$  nm). The dashed line represents the calculated extinction efficiency of pure ZnS particles of total radius of 350 nm ( $\delta = 6\%$ ) assuming a low-dense core ( $R_c = 200$  nm,  $f_c = 0.49$ ,  $\delta_c = 6\%$ ) and a high-dense shell ( $f_s = 0.49$ ) with a volume averaged filling fraction of 0.58; **(b)** highly modulated scattering by large monodisperse ZnS particles (see Fig. II.1-1b). The theoretical curve (dotted line) was calculated using  $R = 1450$  nm,  $f = 0.72$ , and  $\delta = 0.5\%$ .

particle aggregation.

For both SLS and extinction efficiency spectra, good agreement with Mie scattering theory was found for ZnS particles (cores) up to  $\sim 300$  nm in radius. However, in the case of larger ZnS particles a good fit could not be obtained, probably due to an inhomogeneous distribution of ZnS in the particles (Fig. II.1-9b). The extinction curves of the smaller ZnS cores (Fig. II.1-8a) are not sensitive to an inhomogeneous distribution of ZnS. This is understandable, as the inhomogeneities have to be smaller than the wavelength. To give an idea of the effect of inhomogeneities for larger particles, we calculated a curve (Fig. II.1-9a) for a ZnS core with a radius of 350 nm in which the most simple inhomogeneous distribution, that of a core-shell, was assumed. Arbitrarily, we chose the core to have a radius of 200 nm with a filling fraction of 0.49 and the outer shell of 150 nm to have a filling fraction of 0.60. These values give a volume-averaged filling fraction that is the same (0.58) as that obtained from fitting the ZnS cores assuming a homogeneous particle. The curve calculated for a homogeneous distribution is closer to the measured values, but is also not a perfect fit. The differences in both calculated curves make it clear that small inhomogeneities cannot be excluded. However, as no exact model is available for the radial dependence of the refractive index, we did not refine our calculations, as obtaining this function from scattering is an ill-defined problem.<sup>46</sup> The

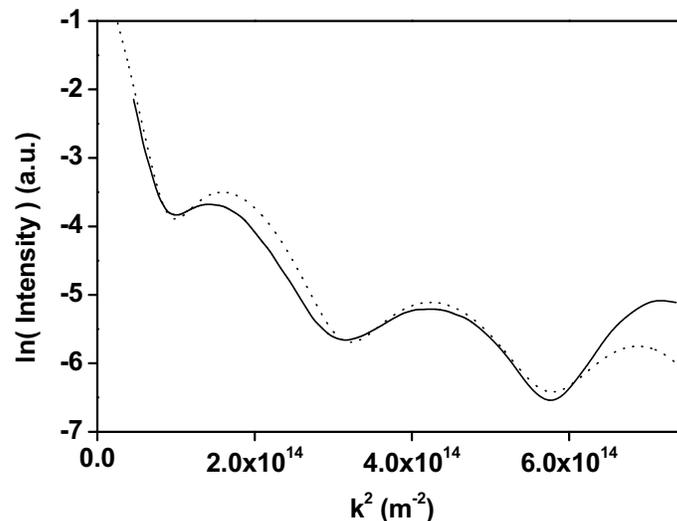


**Figure II.1-10** Experimental SLS spectra (solid line) of ZnS particles (sample 54SN) measured at  $\lambda = 546$  nm as a function of the square of the scattering vector. The theoretical curve (dotted line) was calculated using the same parameters (with  $n_{\text{eff}} = 1.89$ ) as for the extinction efficiency spectra.

optical properties of the core-shell particles can be tuned by changing the thickness of the SiO<sub>2</sub> (ZnS) shell with respect to the core radius. This is an important property, which can be employed to control the filling fraction of the high dielectric material in a photonic crystal made from colloidal crystal of core-shell particles (see Chapter II.2).<sup>30</sup>

## Conclusions

We demonstrated that ZnS colloids covering most of the colloidal size range can be directly coated with a SiO<sub>2</sub> layer, or vice versa, to produce well-defined monodisperse core-shell particles. The coating procedure is performed without using a coupling agent and should be applicable to a variety of metal sulfides. The method produces monodisperse core-shell particles with a tunable core-to-shell size ratio and total radius. Both the ZnS and SiO<sub>2</sub> cores can be dissolved to produce hollow silica and ZnS shells, respectively. The optical properties of small ( $R < 300$  nm) ZnS cores and ZnS-core-SiO<sub>2</sub>-shell particles are well described by an effective refractive index for the ZnS core. Larger ZnS particles cannot be described well as homogeneous scatters. Due to the monodispersity and the high refractive index of the ZnS core (shell) and the availability of many coating procedures, the particles are ideal optical tracers, for instance, in light scattering<sup>65</sup> or optical tweezers studies,<sup>8</sup> and are suitable building blocks for photonic crystals.<sup>13</sup>

## Acknowledgments

We would like to thank Carlos M. van Kats, Arnout Imhof (Utrecht University), and Jacob P. Hoogenboom (FOM AMOLF) for helpful discussions.

---

## References

- (1) Philipse, A. P.; van Bruggen, M. P. B.; Pathmamanoharan, C. *Langmuir* **1994**, *10*, 92.
- (2) Caruso, F.; Susha, A. S.; Giersig, M.; Mohwald, H. *Adv. Mater.* **1999**, *11*, 950.
- (3) Chang, S. Y.; Liu, L.; Asher, S. A. *J. Am. Chem. Soc.* **1994**, *116*, 6739.
- (4) Giersig, M.; Ung, T.; Liz-Marzan, L. M.; Mulvaney, P. *Adv. Mater.* **1997**, *9*, 570.
- (5) Ung, T.; Liz-Marzan, L. M.; Mulvaney, P. *Langmuir* **1998**, *14*, 3740.
- (6) Oldenburg, S. J.; Averitt, R. D.; Westcott, S. L.; Halas, N. J. *Chem. Phys. Lett.* **1998**, *288*, 243.
- (7) Averitt, R. D.; Sarkar, D.; Halas, N. J. *Phys. Rev. Lett.* **1997**, *78*, 4217.
- (8) Viravathana, P.; Marr, D. W. M. *J. Colloid Interface Sci.* **2000**, *221*, 301.
- (9) Zhong, Z. Y.; Yin, Y. D.; Gates, B.; Xia, Y. N. *Adv. Mater.* **2000**, *12*, 206.
- (10) Ocana, M.; Hsu, W. P.; Matijevic, E. *Langmuir* **1991**, *7*, 2911.
- (11) Hsu, W. P.; Yu, R. C.; Matijevic, E. *J. Colloid Interface Sci.* **1993**, *156*, 56.
- (12) Soukoulis, C. M. *Photonic Crystals and Light Localization*; Kluwer Academic Publishers: Dordrecht, 2000; Vol. 315.
- (13) van Blaaderen, A. *MRS Bull.* **1998**, *23*, 39.
- (14) Soukoulis, C. M. *Photonic Band Gap Materials*; Kluwer Academic Publishers: Dordrecht, 1996.
- (15) Yablonovitch, E. *Phys. Rev. Lett.* **1987**, *58*, 2059.
- (16) Bykov, V. P. *Sov. J. Quantum Electron.* **1975**, *4*, 861.
- (17) John, S. *Phys. Rev. Lett.* **1987**, *58*, 2486.
- (18) Scholz, S. M.; Vacassy, R.; Dutta, J.; Hofmann, H.; Akinc, M. *J. Appl. Phys.* **1998**, *83*, 7860.
- (19) Mach, R.; Muller, G. O. *J. Cryst. Growth* **1988**, *86*, 866.
- (20) Harris, D. C. *Infrared Phys. and Tech.* **1998**, *39*, 185.
- (21) Yamaguchi, T.; Yamamoto, Y.; Tanaka, T.; Yoshida, A. *Thin Solid Films* **1999**, *344*, 516.
- (22) Wilhelmy, D. M.; Matijevic, E. *J. Chem. Soc. Faraday Trans.* **1984**, *80*, 563.
- (23) Williams, R.; Yocom, P. N.; Sofko, F. S. *J. Colloid Interface Sci.* **1985**, *106*, 388.
- (24) Celikkaya, A.; Akinc, M. *J. Am. Ceram. Soc.* **1990**, *73*, 245.
- (25) Celikkaya, A.; Akinc, M. *J. Am. Ceram. Soc.* **1990**, *73*, 2360.
- (26) Palik, E. *Handbook of Optical Constants of Solids*; Academic Press, 1997.
- (27) Bhargava, R. N.; Gallagher, D.; Hong, X.; Nurmikko, A. *Phys. Rev. Lett.* **1994**, *72*, 416.
- (28) van Blaaderen, A.; Vrij, A. *Langmuir* **1992**, *8*, 2921.
- (29) Moroz, A.; Sommers, C. *J. Phys.-Condes. Matter* **1999**, *11*, 997.
- (30) Velikov, K. P.; Moroz, A.; van Blaaderen, A. *Appl. Phys. Lett.* **2002**, *80*, 49.
- (31) Bergna, H. E. *The Colloid Chemistry of Silica*; ACS: Washington, DC, 1994; Vol. 234.
- (32) Philipse, A. P. *Colloid Polymer Sci.* **1988**, *266*, 1174.

- (33) Bogush, G. H.; Zukoski, C. F. *J. Colloid Interface Sci.* **1991**, *142*, 19.
- (34) van Blaaderen, A.; van Geest, J.; Vrij, A. *J. Colloid Interface Sci.* **1992**, *154*, 481.
- (35) Correa-Duarte, M. A.; Giersig, M.; Liz-Marzan, L. M. *Chem. Phys. Lett.* **1998**, *286*, 497.
- (36) Iler, R. K. **1959**, USA, Patent No. *2 885 366*.
- (37) Ohmori, M.; Matijevic, E. *J. Colloid Interface Sci.* **1993**, *160*, 288.
- (38) Liz-Marzan, L. M.; Philipse, A. P. *J. Colloid Interface Sci.* **1995**, *176*, 459.
- (39) Alejandro-Arellano, M.; Ung, T.; Blanco, A.; Mulvaney, P.; Liz-Marzan, L. M. *Pure Appl. Chem.* **2000**, *72*, 257.
- (40) Mulvaney, P.; Liz-Marzan, L. M.; Giersig, M.; Ung, T. *J. Mater. Chem.* **2000**, *10*, 1259.
- (41) Yang, C. S.; Liu, Q.; Kauzlarich, S. M.; Phillips, B. *Chem. Mat.* **2000**, *12*, 983.
- (42) Hardikar, V. V.; Matijevic, E. *J. Colloid Interface Sci.* **2000**, *221*, 133.
- (43) Ohmori, M.; Matijevic, E. *J. Colloid Interface Sci.* **1992**, *150*, 594.
- (44) Goller, M. I.; Vincent, B. *Colloid Surf. A-Physicochem. Eng. Asp.* **1998**, *142*, 281.
- (45) Snoeks, E.; van Blaaderen, A.; van Dillen, T.; van Kats, C. M.; Brongersma, M. L.; Polman, A. *Adv. Mater.* **2000**, *12*, 1511.
- (46) Bohren, C. F.; Huffman, D. R. *Absorption and scattering of light by small particles*; Wiley: New York, 1983.
- (47) Stöber, W.; Fink, A.; Bohn, E. *J. Colloid Interface Sci.* **1968**, *26*, 62.
- (48) Vacassy, R.; Scholz, S. M.; Dutta, J.; Plummer, C. J. G.; Houriet, R.; Hofmann, H. *J. Am. Ceram. Soc.* **1998**, *81*, 2699.
- (49) Scholz, S. M.; Vacassy, R.; Lemaire, L.; Dutta, J.; Hofmann, H. *Appl. Organomet. Chem.* **1998**, *12*, 327.
- (50) Kegel, W. K.; van Blaaderen, A. *Science* **2000**, *287*, 290.
- (51) Duran, J. D. G.; Guindo, M. C.; Delgado, A. V.; Gonzalez-Caballero, F. *Langmuir* **1995**, *11*, 3648.
- (52) Duran, J. D. G.; Guindo, M. C.; Delgado, A. V. *J. Colloid Interface Sci.* **1995**, *173*, 436.
- (53) Toikka, G.; Hayes, R. A.; Ralston, J. *Langmuir* **1996**, *12*, 3783.
- (54) Toikka, G.; Hayes, R. A.; Ralston, J. *Colloids Surf. A-Physicochem. Eng. Asp.* **1998**, *141*, 3.
- (55) David, R. L. *Handbook of chemistry and physics*; 76 th ed.; CRC Press, 1995-1996.
- (56) Walcarius, A.; Despas, C.; Bessiere, J. *Microporous and Mesoporous Mater.* **1998**, *23*, 309.
- (57) Pradhan, R. D.; Tarhan, I. I.; Watson, G. H. *Phys. Rev. B-Condens Matter* **1996**, *54*, 13721.
- (58) Dekany, I.; Turi, L.; Tombacz, E.; Fendler, J. H. *Langmuir* **1995**, *11*, 2285.
- (59) Dhas, N. A.; Zaban, A.; Gedanken, A. *Chem. Mat.* **1999**, *11*, 806.
- (60) Velez, O. D.; Kaler, E. W. *Adv. Mater.* **2000**, *12*, 531.
- (61) Dassanayake, U.; Fraden, S.; van Blaaderen, A. *J. Chem. Phys.* **2000**, *112*, 3851.
- (62) Pusey, P. N.; Poon, W. C. K.; Ilett, S. M.; Bartlett, P. *J. Phys.-Condes. Matter* **1994**, *6*, A29.
- (63) Aden, A. L.; Kerker, M. *J. Appl. Phys.* **1951**, *22*, 1242.
- (64) Quirantes, A.; Delgado, A. V. *J. Phys. D: Appl. Phys.* **1997**, 2123.
- (65) Underwood, S. M.; van Megen, W. *Colloid Polymer Sci.* **1996**, *274*, 1072.



---

## II.2 Photonic Crystals of Core-Shell Colloidal Particles

We report on the fabrication and optical transmission studies of thin three-dimensional photonic crystals of high-dielectric ZnS-core and low-dielectric SiO<sub>2</sub>-shell colloidal particles. These samples were fabricated using a vertical controlled drying method. The spectral position and width of a stopgap depend on the core-to-shell ratio, in a manner consistent with numerical calculations. Both experiments and calculations show that the relative L-stopgap width in the case of high-index core low-index shell particles can be larger in comparison to the case of homogeneous particles of either material. The core-shell morphology gives additional control over the photonic stopgap characteristics.

## Introduction

Photonic crystals are materials with a periodically modulated dielectric constant.<sup>1,2</sup> In analogy to electrons in a semiconductor, electromagnetic wave propagation in a photonic crystal can be inhibited for a certain frequency range resulting in the formation of a photonic band gap. A promising way for fabrication of photonic crystals at optical wavelengths is the use of colloidal particles.<sup>3</sup> Colloids can self-organize into a three-dimensional (3D) face-centered-cubic (*fcc*) (or body-centered-cubic) crystal with a long-range periodicity. Although *fcc* structures of dielectric spheres only possess stopgaps,<sup>4,5</sup> the (local) density of states can still be manipulated significantly.<sup>6</sup> Even for quite modest index contrast an interesting photonic switch can be realized with *fcc* crystals.<sup>7</sup> Photonic properties of colloidal crystals can be further improved by using a core-shell particle morphology. The latter can be used to enhance nonlinearities<sup>8</sup> and to engineer photonic bandgap properties.<sup>3</sup> Indeed, the full vector calculations on an *fcc* crystal of core-shell particles have shown that the relative L-stopgap width ( $g_w$ ) can be increased by more than 50% compared to the case of homogeneous particles.<sup>5</sup>

Zinc sulfide (ZnS), due to its high bulk refractive index ( $\beta$ -ZnS,  $n_{589} = 2.36$ ) and lack of absorption in the visible and near IR region,<sup>9</sup> is a convenient material for photonic applications. Spherical ZnS particles can be made with a wide range of sizes (100 – 1500 nm in radius) and high monodispersity (see Chapter II.1).<sup>10,11</sup> Recently, we have shown that a silica layer can be deposited on the ZnS spheres, or vice versa, in order to change the filling fraction of the high-index material and tune the optical properties of the particles (see Chapter II.1).<sup>11</sup> Moreover, ZnS can be doped, e.g., with manganese,<sup>12</sup> to induce luminescence, or, a fluorescent dye can be incorporated into the silica layer at a well-defined radial position.<sup>13</sup> In addition, pure silica or pure ZnS particles, or shells of these materials, can be used for dielectric doping of photonic crystals in order to create localized modes inside the bandgap.<sup>14</sup>

In this Chapter, we demonstrate the fabrication of photonic crystals through a controlled drying<sup>15,16</sup> of a suspension of particles with a high-dielectric ZnS core and a low-dielectric SiO<sub>2</sub> shell. We study optical transmission at normal incidence on thin photonic crystals. In accordance with previous calculations,<sup>5</sup> we demonstrate that photonic crystals of high-index core and low-index shell particles possess a larger relative L-stopgap width in comparison to crystals of low-index core and high-index shell<sup>17</sup> or homogeneous particles.

## Experimental Section

Photonic crystals were fabricated of monodisperse colloidal (core-shell) particles. Three different types of colloidal particles were used. Pure silica particles of radius 123 nm (with a relative width of the size distribution,  $\delta = 5\%$ ) were

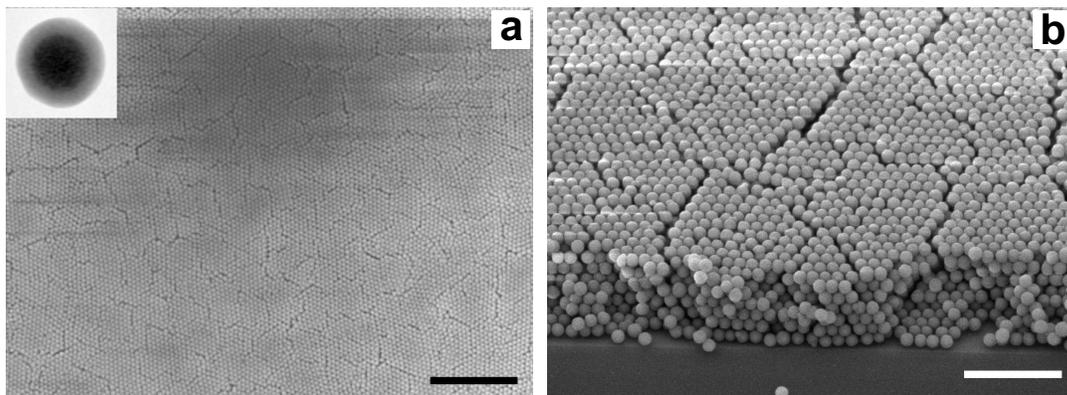
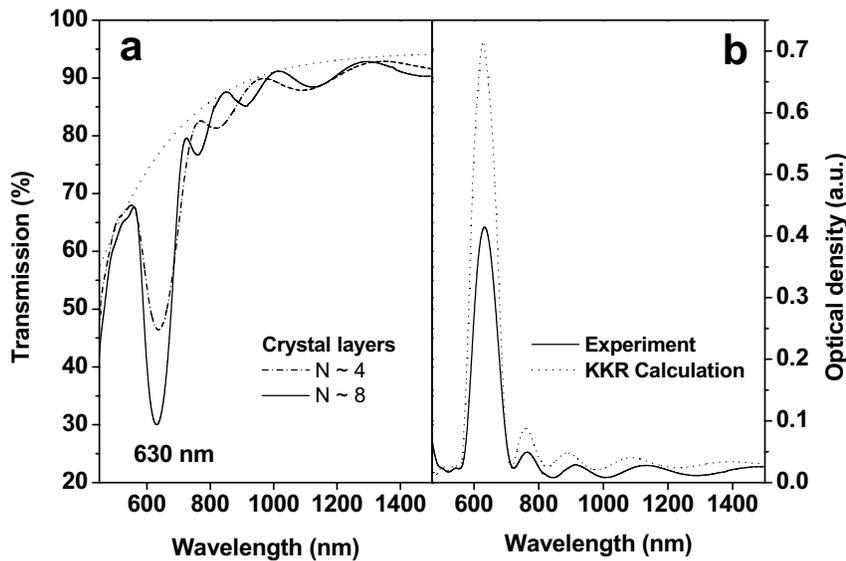


**Figure II.2-1** Scanning electron micrographs (SEM) of a planar photonic crystal of close-packed core-shell colloidal particles. (a) Top view of the crystal showing a (111)-crystal plane. The scale bar is 5  $\mu\text{m}$ . The inset shows a transmission electron micrograph (TEM) of a single ZnS-core-SiO<sub>2</sub>-shell particle. The total particle radius is 128 nm with a 44 nm silica shell. (b) Side view of the crystal. The scale bar is 2  $\mu\text{m}$ .

synthesized following the Stöber-Fink-Bohn method.<sup>18</sup> Homogeneous ZnS-SiO<sub>2</sub> composite particles of radius 125 nm ( $\delta = 6\%$ ) were obtained after condensation of silica inside the pores of the ZnS spheres. In this case, micropores are filled up with silica, which results in an increase of the effective refractive index of the particle. ZnS-core-SiO<sub>2</sub>-shell particles of total radius 128 nm ( $\delta = 5\%$ ) with a ZnS-SiO<sub>2</sub> composite core radius of 84 nm ( $\delta = 6\%$ ) were obtained after coating of ZnS cores with silica. The synthesis and optical characterization of the core-shell particles from ZnS and SiO<sub>2</sub> are described in Chapter II.1.<sup>11</sup> The size and polydispersity were determined by transmission electron microscopy (TEM). The wavelength dependent effective refractive index of the ZnS was determined from extinction measurements of a dilute suspension in ethanol (see Chapter II.1).<sup>11</sup> Thin colloidal crystals were grown onto glass substrates using a vertical controlled drying method.<sup>15,16</sup> This method allows the growth of large (cm) arrays of colloidal crystals with precise control over the crystal thickness. Depending on the particle polydispersity, large (mm) single crystalline domains can be obtained. Scanning electron microscopy (SEM) was used to determine the number of layers in the crystal. The optical transmission spectra, measured with a Cary 500 UV-near-IR spectrometer, were taken along the (111) crystallographic axis, normal to the direction of the glass plate. The light beam spot was about 5 mm<sup>2</sup>, which is comparable to the area of a single crystalline domain.

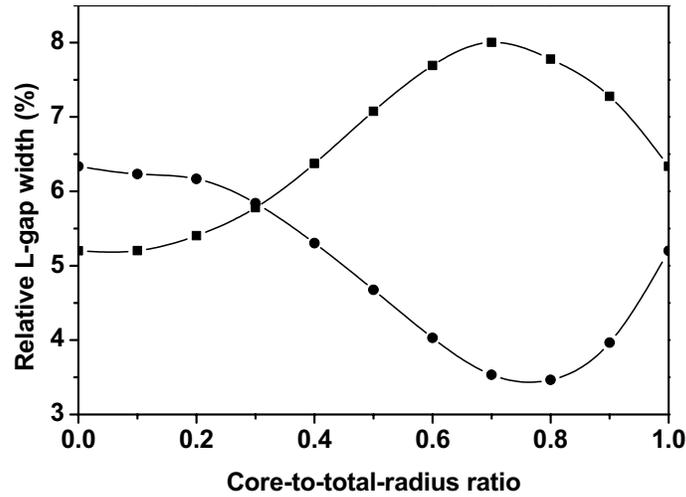
## Results and Discussion

Figure II.2-1 shows SEM micrographs of thin planar crystals of close-packed monodisperse ZnS-core-SiO<sub>2</sub>-shell colloidal particles. Cracks, typically observed every 5–10  $\mu\text{m}$ , are formed after drying and shrinkage of the particles. More cracks form



**Figure II.2-2** Optical transmission spectra (a) measured on photonic crystals of ZnS-core-SiO<sub>2</sub>-shell colloidal particles grown on glass substrates. The experimental spectra were taken along the (111) crystallographic axis. The dotted line shows the assumed background scattering. (b) Calculated (dotted line) and experimentally determined (solid line) optical density spectra (OD),  $OD = -\log(T)$ , of an eight-layer thick crystal on a glass substrate ( $n_{sub} = 1.40$ ). The theoretical spectrum was calculated using the parameters similar to those determined from light scattering and TEM ( $R_c = 93.4$  nm,  $R = 130$  nm,  $\phi_{ZnS} = 62\%$ ,  $n_{589} = 1.92$ ).

under influence of the vacuum and electron beam in the SEM, therefore there are less cracks present in the films used for extinction measurements. However, the crystalline order extends over a much longer distance. The inset shows a TEM image of a single particle, where the ZnS core and SiO<sub>2</sub> shell can be directly seen. Figure II.2-2 shows optical transmission spectra of thin photonic crystals of ZnS-core-SiO<sub>2</sub>-shell particles. The spectra exhibit a minimum in the optical transmission, where the light satisfies the Bragg condition and is diffracted away from the propagation direction. The small shift ( $\sim 7$  nm) of the stop bandgap position to longer wavelengths is a finite-size effect. The thickness dependence of the stopgap position disappears if the sample is thicker than  $\sim 8$ – $10$  layers.<sup>19</sup> For the given dielectric contrast, this is also expected from one-dimensional calculations.<sup>20</sup> The fast decrease of the optical transmission, near, but before the absorption edge of ZnS,<sup>9</sup> is due to the strong scattering from the crystal defects. Theoretical spectra were calculated using the layer KKR method.<sup>21</sup> In order to compare with the numerical calculations, the background scattering (shown with dotted line on Fig. II.2-2a) was subtracted.<sup>19</sup> The peak position, the width, and the interference ripples agree well with theory (Fig. II.2-2b). However, the height of the maximum does not. This is because of the unavoidable presence of crystal defects. An exact match of the experimental spectra is difficult to obtain, because the crystal thickness is very likely not constant over the measured region.



**Figure II.2-4** Calculated relative L-stopgap width as a function of the core-to-total-radius ratio for an infinite crystal of high-index core low-index shell particles (squares) and, for comparison, the reverse structure with the same parameters (circles). The high-index core (shell) consists of 62% bulk ZnS embedded in a silica matrix. The low-index shell (low-index core) consists of pure silica. The wavelength dependent effective dielectric constant of the high-index core (high-index shell) was calculated using the Maxwell-Garnett formula.<sup>11</sup> The line is to guide the eye.

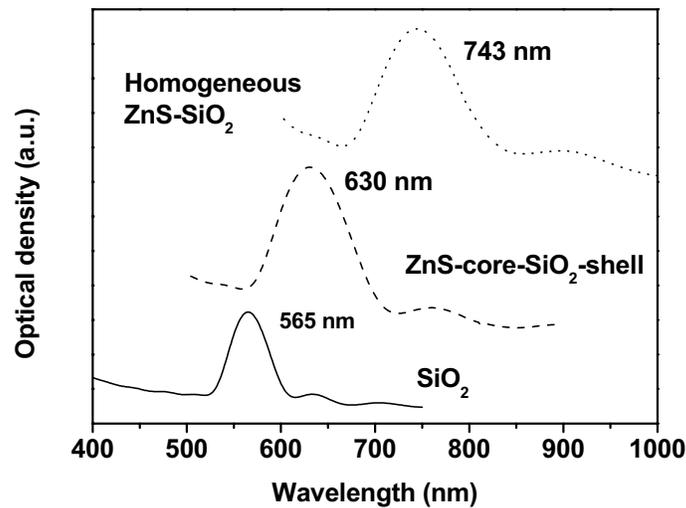


**Figure II.2-3** Optical density (OD) spectra measured on photonic crystals of homogeneous ZnS-SiO<sub>2</sub> composite (dotted line), ZnS-core-SiO<sub>2</sub>-shell (dashed line), and pure silica (solid line) particles. The average crystal thickness is eight layers. The position of the L-stopgap shifts towards longer wavelengths as the effective refractive index of the single particle increases.

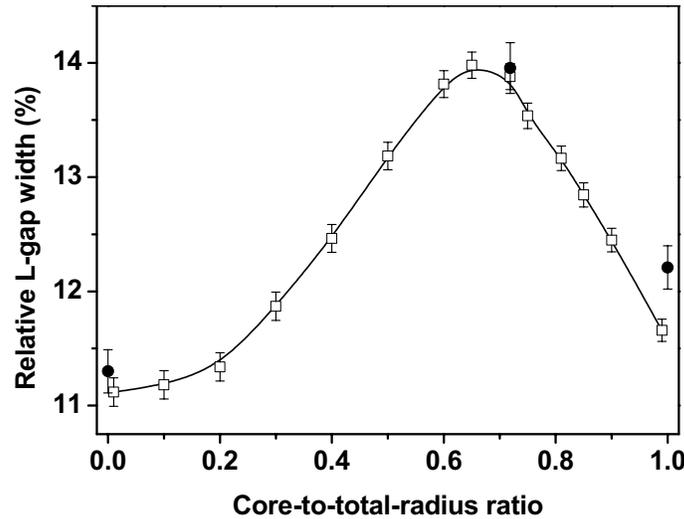


**Figure II.2-5** Relative L-stopgap (the crystallographic direction is defined with respect to an infinite crystal) width at half-maximum determined from the experimental (circles) and theoretical (open squares) spectra as a function of the core-to-total-radius ratio for eight-layers thick crystals. The experimental data are obtained from crystals of pure silica, ZnS-core-SiO<sub>2</sub>-shell, and ZnS-SiO<sub>2</sub> composite particles of similar radii (Fig. II.2-4). Theoretical spectra were calculated with the same particle parameters as in Fig. II.2-1b. There is an optimal ratio ( $\gamma \sim 0.65$ ) at which the stopgap has a maximal value. The line is to guide the eye.

In order to demonstrate the importance of the particle morphology we performed calculations for infinite crystals. Figure II.2-3 shows the calculated relative L-stopgap width,  $g_w$ , of ZnS-core-SiO<sub>2</sub>-shell and SiO<sub>2</sub>-core-ZnS-shell particles as a function of the core-to-total-radius ratio ( $\gamma = R_c/R$ ). The calculations were performed using a wavelength dependent effective refractive index (see Chapter II.1).<sup>11</sup> In both cases, the filling fraction of bulk ZnS (in a silica matrix,  $n = 1.45$ ) in the particle core or shell was 0.62. The high-index core low-index-shell particles display a maximum in the  $g_w$  at  $\gamma \sim 0.70$ , which is about 20% larger than that of a photonic crystal of homogeneous particles with the higher refractive index. Remarkably, calculations show that a crystal of high-index core low-index-shell particles in air for  $\gamma \sim 0.70$  also has a larger  $g_w$  compared to the case of an air-sphere crystal (i.e., high index material surrounding spheres of air). In contrast, the reverse system displays a minimum at  $\gamma \sim 0.76$  and a gap width that is lower than that of homogeneous particles. These calculations demonstrate the effect of the morphology and optimization of the filling fraction of the high dielectric material, using core-shell particles, on the optical properties of photonic crystals. For the L-stopgap the high-index core low-index shell morphology is clearly better than the low-index-core high-index shell<sup>17</sup> for photonic applications. Figure II.2-4 compares measured optical transmission spectra of thin

photonic crystals from silica, ZnS-core-SiO<sub>2</sub>-shell, and homogeneous ZnS-SiO<sub>2</sub> composite particles of similar radii. Despite being of almost the same total radius, the stopgap moves towards longer wavelengths because of the increased effective refractive index of the single particle. Figure II.2–5 presents the experimental and calculated relative L-stopgap (crystallographic directions mentioned hereafter are with respect to an infinite crystal) width,  $g_w$ , for a finite crystal measured at half-maximum as a function of the core-to-total-radius ratio. The values determined from the experimental spectra (Fig. II.2–4) are in good agreement with those from the theoretical spectra for an eight-layer thick crystal. However, the  $g_w$  obtained from the experiment is slightly broadened due to the presence of a moderate disorder in the crystal. This effect has been observed earlier.<sup>22</sup> Assuming equal contributions of the crystal defects in the three cases, based on the similar particle polydispersity, a clear maximum can be distinguished in the case of the crystal of core-shell particles. One should notice that the  $g_w$  for thin crystals is still strongly dependent on the number of crystal layers. For instance, calculations for seven layers showed a ~1% increase of  $g_w$ .

## Conclusions

In conclusion, we have demonstrated the fabrication of photonic crystals of high-index ZnS core and low-index SiO<sub>2</sub> shell colloidal particles. Due to the optimal filling fraction of the high dielectric material, photonic crystals from core-shell particles possess a larger relative L-stopgap width than crystals from homogeneous particles. By applying a low-dielectric coating we demonstrated the ability to control the filling fraction of the high dielectric material and optical properties of the photonic crystal. The combination of ZnS and SiO<sub>2</sub> opens new possibilities to study dielectrically and fluorescently doped photonic crystals.

## Acknowledgments

We would like to thank Arnout Imhof (Utrecht University), Jacob P. Hoogenboom (FOM AMOLF), Edd J. Vlietstra, and Carlos M. van Kats (Utrecht University) for their assistance and helpful discussions.

---

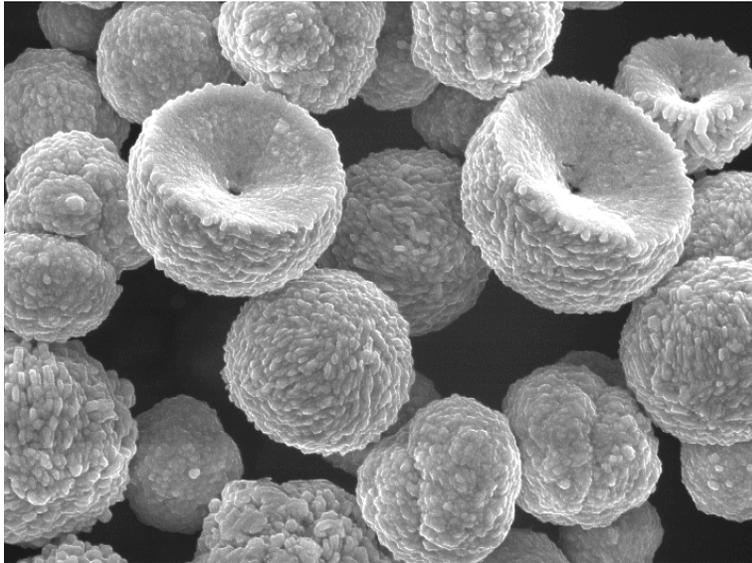
## References

- (1) Yablonovitch, E. *Phys. Rev. Lett.* **1987**, *58*, 2059.
- (2) Bykov, V. P. *Sov. J. Quantum Electron.* **1975**, *4*, 861.
- (3) van Blaaderen, A. *MRS Bull.* **1998**, *23*, 39.
- (4) Sozuer, H. S.; Haus, J. W.; Inguva, R. *Phys. Rev. B-Condens Matter* **1992**, *45*, 13962.
- (5) Moroz, A.; Sommers, C. *J. Phys.-Condes. Matter* **1999**, *11*, 997.
- (6) Zhang, Z.; Satpathy, S. *Phys. Rev. Lett.* **1990**, *65*, 2650.

- (7) Pan, G. S.; Kesavamoorthy, R.; Asher, S. A. *Phys. Rev. Lett.* **1997**, *78*, 3860.
- (8) Chemla, D. S.; Miller, D. A. *Opt. Lett.* **1986**, *11*, 522.
- (9) Scholz, S. M.; Vacassy, R.; Dutta, J.; Hofmann, H.; Akinc, M. *J. Appl. Phys.* **1998**, *83*, 7860.
- (10) Wilhelmy, D. M.; Matijevic, E. *J. Chem. Soc. Faraday Trans.* **1984**, *80*, 563.
- (11) Velikov, K. P.; van Blaaderen, A. *Langmuir* **2001**, *17*, 4779.
- (12) Bhargava, R. N.; Gallagher, D.; Hong, X.; Nurmikko, A. *Phys. Rev. Lett.* **1994**, *72*, 416.
- (13) van Blaaderen, A.; Vrij, A. *Langmuir* **1992**, *8*, 2921.
- (14) Pradhan, R. D.; Tarhan, I. I.; Watson, G. H. *Phys. Rev. B-Condens Matter* **1996**, *54*, 13721.
- (15) Denkov, N. D.; Velev, O. D.; Kralchevsky, P. A.; Ivanov, I. B.; Yoshimura, H.; Nagayama, K. *Langmuir* **1992**, *8*, 3183.
- (16) Jiang, P.; Bertone, J. F.; Hwang, K. S.; Colvin, V. L. *Chem. Mater.* **1999**, *11*, 2132.
- (17) Breen, M. L.; Dinsmore, A. D.; Pink, R. H.; Qadri, S. B.; Ratna, B. R. *Langmuir* **2001**, *17*, 903.
- (18) Stöber, W.; Fink, A.; Bohn, E. *J. Colloid Interface Sci.* **1968**, *26*, 62.
- (19) Bertone, J. F.; Jiang, P.; Hwang, K. S.; Mittleman, D. M.; Colvin, V. L. *Phys. Rev. Lett.* **1999**, *83*, 300.
- (20) Rorres, C. *SIAM J. Appl. Math.* **1974**, *27*, 303.
- (21) Stefanou, N.; Yannopapas, V.; Modinos, A. *Comput. Phys. Commun.* **1998**, *113*, 49.
- (22) Vlasov, Y. A.; Deutsch, M.; Norris, D. J. *Appl. Phys. Lett.* **2000**, *76*, 1627.

## Part III

# Photonic Materials of Metallo-Dielectric Colloidal Particles





---

## III.1 Synthesis and Characterization of Large Colloidal Silver Particles for Photonic Applications

Metal colloidal particles are widely used as building blocks for novel materials with photonic applications. In this article, we demonstrate the synthesis of silver particles with a wide range of sizes (up to 1200 nm in radius) by reducing silver nitrate with ascorbic acid in aqueous solutions in the presence of a polymeric steric stabilizer. The resulting particles were spherical aggregates with a rough surface and polydispersity below 20%. The particle morphology was examined by electron microscopy. Optical properties on a single particle level were studied by means of extinction measurements and compared to scattering theory. At low ionic strength the effective polydispersity of the charged silver particles was low enough that colloidal crystals could be grown.

## Introduction

Colloidal metal and metallo-dielectric particles are of great fundamental and industrial interest. Metal colloidal particles are used in catalysis,<sup>1,2</sup> in biological and chemical sensing,<sup>3</sup> nonlinear optics,<sup>4,6</sup> surface-enhanced Raman spectroscopy (SERS),<sup>7,8</sup> and electronics.<sup>9</sup> Recently, metal and metallo-dielectric spheres found new applications in the field of photonic crystals.<sup>10-14</sup> Photonic crystals are materials with a periodically modulated dielectric constant.<sup>15-17</sup> In analogy to electrons in semiconductors, electromagnetic wave propagation in photonic crystals can be forbidden for a certain frequency range resulting in the formation of a complete photonic band gap (CPBG); photons in the gap cannot travel in any direction for any polarization. It has been shown theoretically that in a face-centered-cubic (*fcc*) crystal of metal or metallo-dielectric spheres a CPBG in the visible can be opened.<sup>10-12</sup> Because of the high dielectric contrast necessary ( $> 2.8$  for air-sphere *fcc* crystals<sup>18,19</sup>), it is difficult to create a CPBG in the visible with purely dielectric materials. To build photonic crystals, the size of the particles should be comparable to the wavelength of light. The second important requirement is to use particles with low absorption in the region of application. A few metals (Ag, Au, Al, Ni, Cu) have been investigated theoretically as possible candidates for metallo-dielectric photonic crystals.<sup>10-14</sup> Because of its low bulk absorption, silver (Ag) is the most suitable metal to create a band gap in the visible. Recent calculations of Moroz have shown that a CPBG can be even opened up for a filling fraction of silver as low as 2%.<sup>20</sup>

Several methods have been developed to synthesize colloidal metal particles.<sup>21-23</sup> These are, precipitation from homogeneous solutions by using appropriate reducing agents,<sup>24,25</sup> seeded growth,<sup>26</sup> reverse micelles,<sup>27,28</sup> electrochemical,<sup>29</sup> and sonoelectrochemical<sup>30</sup> techniques. Among these, precipitation in aqueous or non-aqueous media is the most commonly used because it is easy, cheap, and versatile. The precipitation technique offers many possibilities to control the particle characteristics by changing the experimental parameters, like reactants concentrations, temperature, pH, reducing agents, and stabilizers.<sup>21,31,32</sup> Furthermore, it is also possible to synthesize composite particles and alloys.<sup>33-35</sup> Because of the high electropositive character of silver (+ 0.799 V<sup>36</sup>), various reducing agents including sodium borohydride ( $\text{NaBH}_4$ ),<sup>37</sup> citrate or ethylenediaminetetraacetic acid (SDTA),<sup>38</sup> and ethanol<sup>39</sup> can be used. However, most methods known for the preparation of metal spheres were developed to produce small particles (radius less than 100 nm). Only recently, gold particles with a radius up to 2  $\mu\text{m}$  were synthesized by controlled aggregation of gold nanoparticles using gum arabic as a steric stabilizer.<sup>21</sup>

In this Chapter, we will describe the synthesis of silver particles of a wide range of sizes and narrow size distribution by reducing silver nitrate with ascorbic

acid in an aqueous medium. The particle morphology was studied by electron microscopy. Optical response on a single particle level was studied by means of extinction measurements and compared to scattering theory. The formation of charge-stabilized colloidal crystals and colloidal glasses of the silver particles in water was studied by reflection confocal microscopy.

## Experimental Section

**Materials.** All reagents were used as received without further purification. Ultra pure grade silver nitrate ( $\text{AgNO}_3$ ) was purchased from Acros Organics, Gum arabic from Sigma, Ascorbic acid ( $\text{C}_6\text{O}_8\text{H}_6$ ) from PG Farma, and sodium hydroxide ( $\text{NaOH}$ ) from Baker Chemicals B.V. All solutions were prepared with deionized water.

**Particle Synthesis.** A variable amount of a silver nitrate stock solution was added to a variable amount of a stock solution of gum arabic and filled up to a controlled volume with deionized water. In the same way, a solution containing controlled amounts of ascorbic acid and gum arabic was prepared; then, filled up to a certain volume. The pH of the reaction mixture was set at this stage by adding a controlled volume of  $\text{NaOH}$  to the ascorbic acid solution. Both reactant solutions always contained the same weight-percentage of gum arabic. The reactions were carried out in a two-necked round-bottom flask of 250 ml with a magnetic stirrer or with a variable high-speed electric stirrer (1100 rpm). First, the solution containing the ascorbic acid was put into the reaction flask. Then, the silver solution was quickly added to the vigorously stirred acid solution. As a result of the size-dependent extinction of the silver particles, the color of the solution turned from transparent, to black, and then to dark brown-grayish as the scattering contribution increased. After several hours ( $\sim 2\text{--}4$  h) the solution became brownish to green-brownish. The induction time (a few seconds) for these colors to appear was dependent on the reaction conditions. The solutions were stirred up to 24 hours at room temperature. Subsequently, the dispersions were washed twice with deionized water after sedimentation or centrifugation (max. 200 G). The silver particles were kept in water where they remain stable longer than a year.

**Particle Characterization.** The particle morphology was studied by transmission electron microscopy (TEM) and scanning electron microscopy (SEM) on a Philips CM10 and on a Philips XL30 FEG respectively. The particle size and polydispersity were determined from the TEM micrographs using a Nikon profile projector. Thermo-gravimetric analysis (TGA) was performed on a Setaram 92. A Coulter Delsa 440 SX was used to measure the particle electrophoretic mobility in aqueous suspension. UV-vis spectroscopy (Cary 1E UV-vis spectrophotometer) was performed on dilute ( $< 10^{-5}$  vol. %) suspensions of Ag particles in water. The optical path was 1.0 cm. Fitting of the spectra was performed using a FORTRAN computer

algorithm developed by Wiscombe,<sup>40</sup> adapted to take the size polydispersity into account. Colloidal crystallization was studied in both little glass vials (1.7 ml), of which the bottom was replaced by a microscope cover slip (Chance Proper) with a thickness of 0.15 mm and thin (0.20 mm) glass capillaries (VitroCom). Charge-stabilized crystals and glasses in water were observed in reflection mode ( $\lambda = 632$  nm) with a confocal microscope (Leica DM IRB, in combination with a Leica TCS NT scanhead) with an oil-immersion lens (Leica, 100 $\times$ , NA 1.4).

## Results and Discussion

**Particle Synthesis.** Silver ions are reduced to metal silver by ascorbic acid ( $C_6H_8O_6$ ), which has a sufficiently lower redox potential,<sup>21,41</sup> according to the following reaction



Matijevic *et al.* proposed a particle growth model for a similar synthesis of gold particles.<sup>42</sup> The nucleation burst takes place when the concentration of metal atoms reaches a critical supersaturation. In the first step, the nuclei formed grow to nano-sized primary particles by diffusion capture of the remaining atoms. In the second step, depending on the reaction conditions, the primary particles aggregate leading to the formation of larger spherical aggregates accompanied with narrowing of the size distribution.<sup>42</sup> The precipitation was carried out at different pH values, concentration of the protective colloid, and different concentration of silver and ascorbic acid (Table III.1–1).

**Table III.1–1 Radius ( $R$ ) and polydispersity ( $\delta$ ) of silver particles obtained at different experimental conditions as determined by TEM.**

[AgNO <sub>3</sub> ] (mol/l)	[C <sub>6</sub> H <sub>8</sub> O <sub>6</sub> ] (mol/l)	Ratio [acid]/[Ag]	Gum arabic wt (%)	$R$ (nm)	$\delta$ (%)
0.083	0.333	4	0.7	223	67
0.083	0.167	2	0.7	894	24
0.083	0.333	4	0.35	429	33
0.083	0.167	2	0.35	1149	16
0.167	0.666	4	0.7	796	29
0.167	0.333	2	0.7	525	39
0.167	0.666	4	0.35	943	35
0.167	0.333	2	0.35	588	31

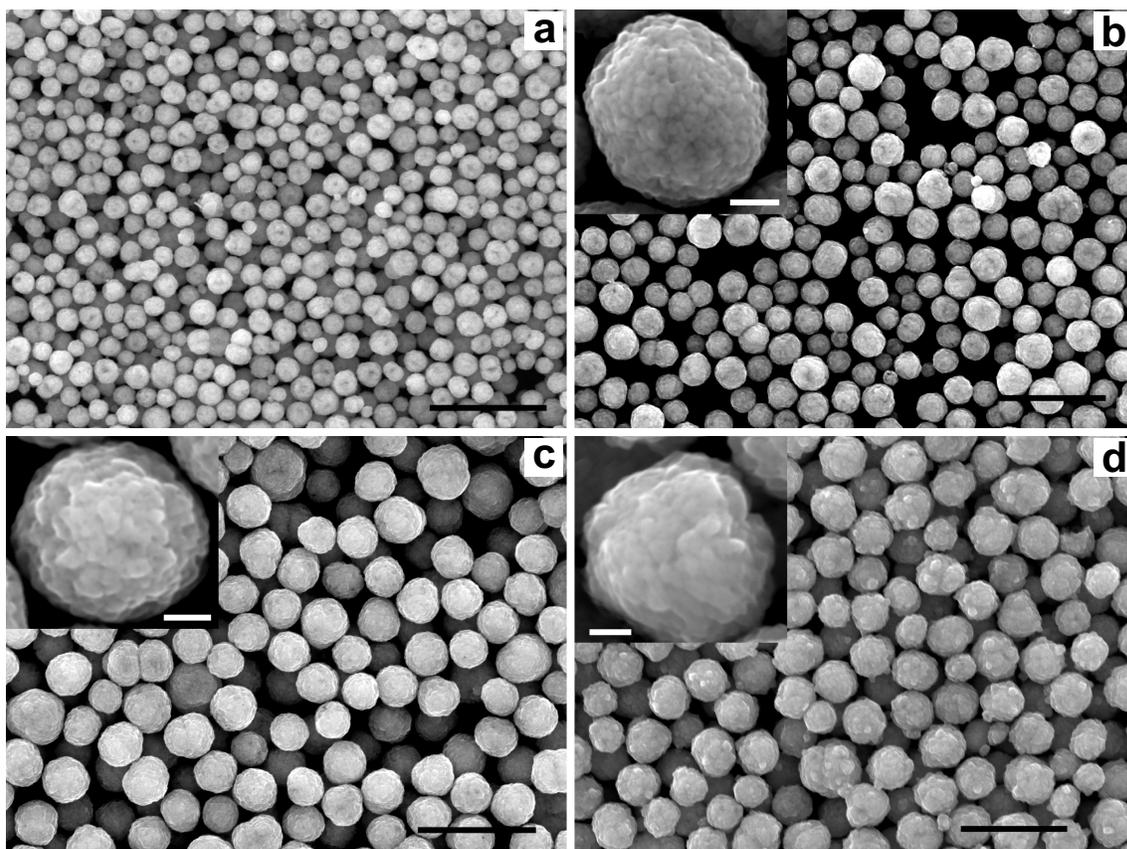


**Figure III.1-1** Scanning electron micrographs (SEM) of relatively monodisperse silver particles obtained under different experimental conditions, radii ( $R$ ) and relative width of the size distribution ( $\delta$ ): (a)  $R = 197$  nm,  $\delta = 13\%$ ; (b)  $R = 284$  nm,  $\delta = 17\%$ ; (c)  $R = 383$  nm,  $\delta = 13\%$ ; (d)  $R = 418$  nm,  $\delta = 12\%$ . Scale bars are  $2\ \mu\text{m}$ . The insets show a blow up of the particle surface. The scale bars in the insets are  $200$  nm.

The results are strongly dependent on the age of the solutions. Using freshly prepared solutions was necessary to obtain reproducible results. Because of the strong size-dependent extinction, the particle growth can be monitored in the reaction flask through a change in color of the suspension. Because of scattering, the final suspension of large particles had a brownish appearance (see below). Figure III.1-1 shows SEM micrographs of relatively monodisperse silver particles obtained at different experimental conditions. The final particle size depends on the pH of the reaction mixture (Fig. III.1-2). At higher pH values the primary particles have a sufficiently large surface charge, which, possibly in combination with the effect of the protective polymer layer, diminishes the effect of the high ionic strength and prevents significant aggregation. As a result, the final particles are not significantly larger than the primary particles. With a decrease of the pH, the system approaches the isoelectric point and, therefore, becomes less stable leading to a higher degree of aggregation of the primary particles and to the formation of larger secondary

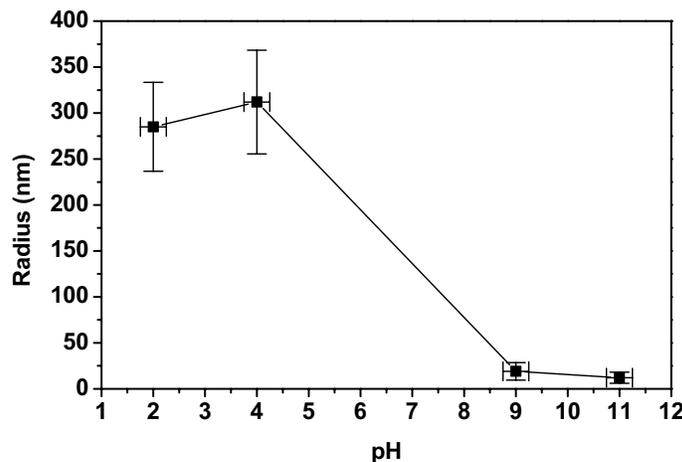


**Figure III.1-2** Particle size as a function of the pH of the reaction mixture. The reaction mixture had an initial pH  $\sim$  2. The pH was regulated by addition of NaOH solution. Particles were synthesized using the following concentrations:  $[\text{AgNO}_3] = 0.010 \text{ M}$ ,  $[\text{C}_6\text{O}_8\text{H}_6] = 0.050 \text{ M}$ , gum arabic 0.056 wt %.

particles. This mechanism is quite general and has been proposed for the formation of several inorganic particles.<sup>42,43</sup>

The amount of gum arabic added also influences the aggregation rate. At higher concentration of gum the particles became smaller (Table III.1-1). This occurs because of the enhanced steric stabilization<sup>44</sup> of the small primary particles, which prevents their aggregation leading to smaller secondary particles. In addition, at high gum concentration the viscosity of the reaction mixture will be increased and the diffusion aggregation of the primary particles will be suppressed. The effect of gum arabic on the reaction was not studied in detail.

As in the case of gold particles,<sup>41</sup> the speed of mixing of the reactants influences the time dependent supersaturation, i.e., the build up of metal silver in the suspension. When the mixing time is shorter, the silver nucleation takes a shorter amount of time which results in more monodisperse primary particles.<sup>42</sup> If the reactants are added slowly, there will be a continuous generation of nuclei during the mixing. As the first nuclei formed will act like seeds<sup>45</sup> and will further grow to larger size before aggregation and forming a secondary particles, the primary particles will have a broader size distribution. As a result, the size of the final secondary particles remains approximately the same, but the particle surface is rougher indicating the presence of larger subunits.

**Particle Morphology.** By use of the procedure described above we obtained spherical silver particles with a radius in the range 100 – 1200 nm. Particle polydispersity was more difficult to control and varied over a wide range. However, a polydispersity as low as 12% was achieved in several samples. The particles are spherical aggregates with a rough surface (see the insets in Fig. III.1-1) where the

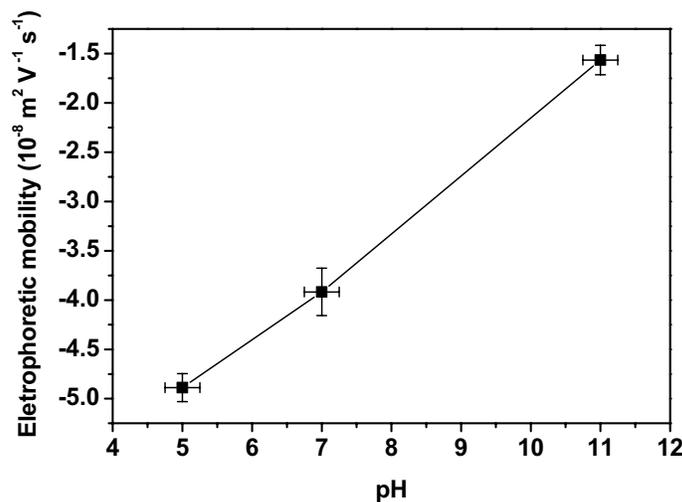


**Figure III.1-3** Electrophoretic mobility of silver particles ( $R = 256 \text{ nm}$ ,  $\delta = 17\%$ ) dispersed in water as a function of the pH.

roughness is on the order of a few nanometers. The SEM pictures clearly reveal the aggregated nature of the final particles, which consist of small ( $< 20 \text{ nm}$ ) subunits. Despite several cleaning cycles, TGA analysis showed that the particles contained  $\sim 4\%$  organic compounds, most likely composed of the protective polymer (gum arabic) and perhaps a small amount of ascorbic acid or its derivatives. As a result of the dissociation of the carboxyl groups of adsorbed ascorbic acid and the absorption of different other ionic species, the particle surface is charged. Figure III.1-3 shows electrophoretic mobility measurements on silver particles of  $256 \text{ nm}$  in radius ( $\delta = 17\%$ ) dispersed in water as a function of pH. The particle surface charge is negative over a wide range of pH values including neutral water suspensions. The fact that the electrophoretic mobility decreases at higher pH values indicates some degree of oxidation of the particle surface, which probably occurred after the separation from the reaction mixture. The particle surface charge is determined by the oxide layer and the remaining carboxyl groups attached to the surface. The surface charge plays an important role in the particle self-organization after sedimentation in aqueous suspensions.

**Optical Properties.** When colloidal particles are used for photonic applications (such as in photonic crystals or SERS) it is important to know the optical response on a single particle level. We performed extinction measurements on dilute suspensions of Ag particles of different radii in water. All spectra were taken in the range of  $250 - 900 \text{ nm}$ . Figure III.1-4 shows two examples of experimentally determined extinction efficiency spectra of Ag particles of radii  $284 \text{ nm}$  and  $383 \text{ nm}$ . Both spectra display a sharp minimum at  $\sim 318 \text{ nm}$ , which corresponds to a

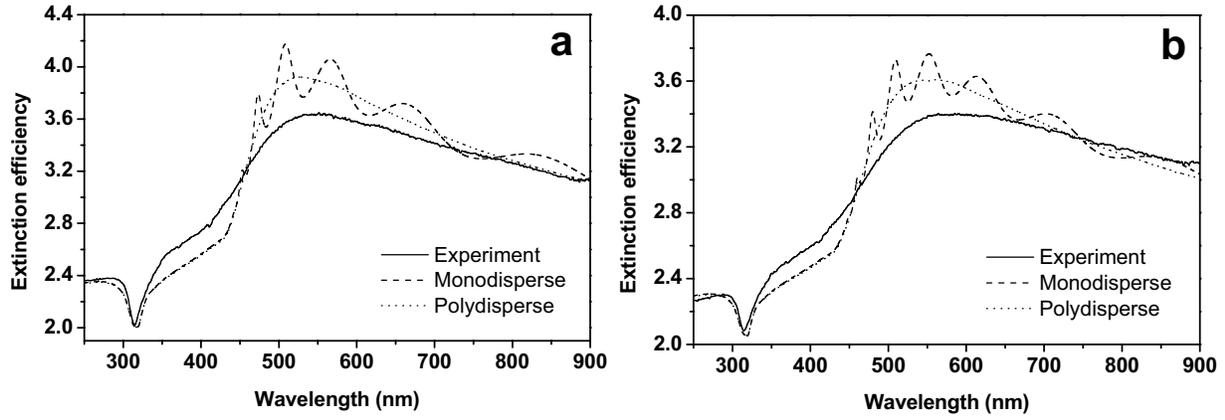


**Figure III.1-4** Comparison between the experimental (solid line) and calculated extinction efficiency for monodisperse (dashed line) and polydisperse (dotted line) particles in water. (a)  $R = 284$  nm,  $\delta = 16\%$  (from TEM); theoretical spectra were calculated using  $R = 285$  nm  $\phi_{Ag} = 0.80$ ; (b)  $R = 383$  nm,  $\delta = 13\%$  (from TEM); theoretical spectra were calculated using  $R = 385$  nm  $\phi_{Ag} = 0.80$ . In both cases polydispersity was set at 15%.

minimum in the imaginary part of the refractive index ( $n_{im} = \text{Im}(\sqrt{\epsilon(\lambda)}) \sim 0.4$  for bulk silver<sup>46</sup>). The depth of this minimum depends on the particle radius, but the position, for the sizes studied here, is determined by the dielectric properties of the metal. At longer wavelengths a broad band due to surface plasma resonances was observed. The position of the peak shifts towards longer wavelengths if the particle size is increased. Our experiments showed that the dependence of the extinction on the particle radius is not as strong as in the case of dielectric spheres.<sup>47</sup> Because of the complex refractive index of Ag and the size of the particles studied, a full solution of the Maxwell equations is necessary to quantitatively describe the light scattering and absorption by the system. The exact shape of the curves in general is sensitive to particle size, dielectric contrast, and polydispersity. In this case, however, due to the imaginary part of the silver refractive index, fine resonances are damped.<sup>47</sup> The extinction efficiency spectra were calculated using scattering theory extended to the case of polydisperse particles assuming a Gaussian size distribution. The effective dielectric constant of a sphere is represented as an effective dielectric constant of a mixture of a bulk Ag and a dielectric (solvent). The effective dielectric constant,  $\epsilon_{eff}$ , was calculated using the Bruggeman effective medium model for a randomly connected inhomogeneous medium<sup>47</sup>

$$\epsilon_{eff}(\lambda) = \frac{1}{4} \left[ g \pm \sqrt{g^2 + 8\epsilon_{Ag}(\lambda)\epsilon_s} \right],$$

where

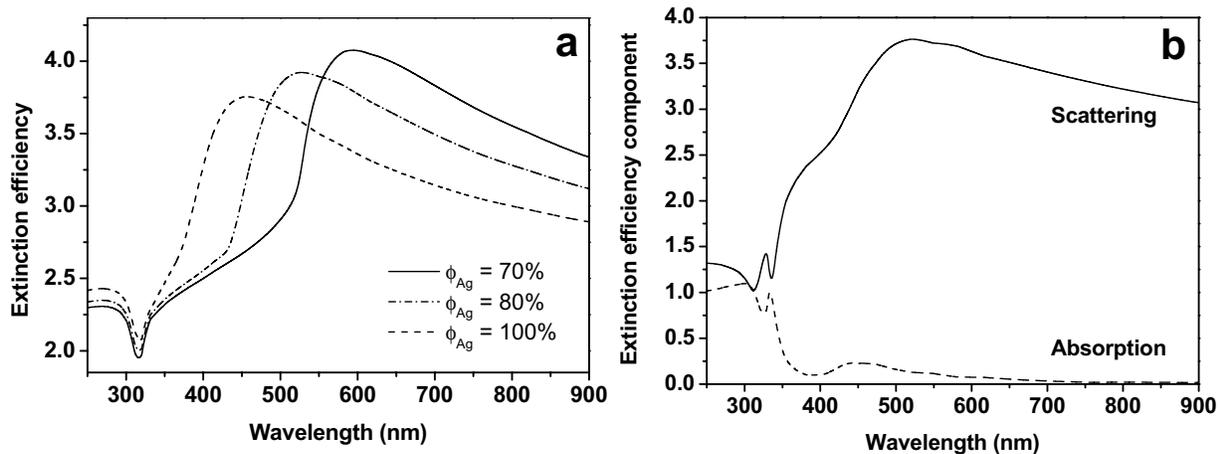


**Figure III.1-5** Extinction efficiency of silver particles (Fig. III.1-1b) of radius 284 nm ( $\delta = 17\%$ ) dispersed in water. (a) Theoretical extinction efficiency spectrum (dotted line) for particles  $R = 285$  nm ( $\delta = 15\%$ ), assuming 70% (solid line), 80% (dashed line), and 100% (dotted line) bulk silver in a particle. The effective dielectric constant was calculated using the Bruggeman effective medium model. (b) Theoretical scattering (solid line) and absorption (dashed line) efficiency components of the total extinction ( $R = 285$  nm,  $\phi_{Ag} = 80\%$ ).

$$g = (3\phi_{Ag} - 1)\varepsilon_{Ag}(\lambda) + (2 - 3\phi_{Ag})\varepsilon_s,$$

where  $\phi_{Ag}$  is the filling fraction of bulk Ag with a wavelength-dependent dielectric constant  $\varepsilon_{Ag}(\lambda)$ ,<sup>46</sup> and  $\varepsilon_s$  is the solvent dielectric constant. The wavelength dependence of the refractive index of the solvent (water  $n_s = 1.33$ ) was neglected. The theoretical spectrum (Fig. III.1-4a) was calculated using a particle size and polydispersity determined from TEM and a filling fraction of bulk silver  $\phi_{Ag} = 0.80$ . Values in the range of 0.75–0.85 for the filling fraction of silver were found to give the best description of the scattering of all particles studied. Model calculations have shown that the position of the maximum extinction is strongly dependent on the filling fraction of bulk silver (Fig. III.1-5a). The theoretical spectra describe the experimental spectra relatively well. However, we could not find a perfect match for the whole extinction curve. Most probably this is because of the more complicated structure and shape (roughness) of the particles studied and/or the use of an effective medium approximation.

As already mentioned, the absorption of light by metal particles is an important issue. The physical origin of this absorption is the coherent oscillation of the conduction band electrons induced by the electromagnetic field<sup>48</sup>. Scattering theory allows for separation of the scattering and absorption components of the total extinction efficiency (Fig. III.1-5b). For large particles the scattering dominates over the absorption. Therefore, for wavelengths longer than 500 nm, the contribution of

absorption to the total extinction is less than 5%.

**Colloidal Crystallization.** Silver particles dispersed in water possess a negative surface charge as inferred from the electrophoretic mobility measurements (Fig. III.1–3). The surface charge of the colloidal spheres derives probably from the dissociation of acid groups, which were adsorbed during the synthesis of the spheres, or a thin layer of silver oxide formed thereafter. Figure III.1–6a shows a confocal image in reflection mode of the bottom layer of a charge-stabilized colloidal crystal of Ag spheres of radius 257 nm ( $\delta = 17\%$ ) in water formed at the bottom of a small glass vial. The crystal lattice spacing as determined by reflection confocal microscopy was  $\sim 1 \mu\text{m}$ , a value which is much larger than the particle diameter. Despite the relatively large size polydispersity of the core, the particles formed single colloidal crystals, which in some cases were hundreds of  $\mu\text{m}$  in size. It is known from computer simulations and experiments that colloids interacting with a hard-sphere like potential cannot form colloidal crystals with a polydispersity above  $\sim 7\%$ .<sup>49,50</sup> The core of the silver particles are significantly more polydisperse. The fact that these particles can form crystals, with low filling fraction, is caused by the double layer repulsion, which is long-range because of the low ionic strength. The long-range repulsion decreases the effective polydispersity of the system. In general, the crystal structure of the lattice is determined by parameters such as particle number density,

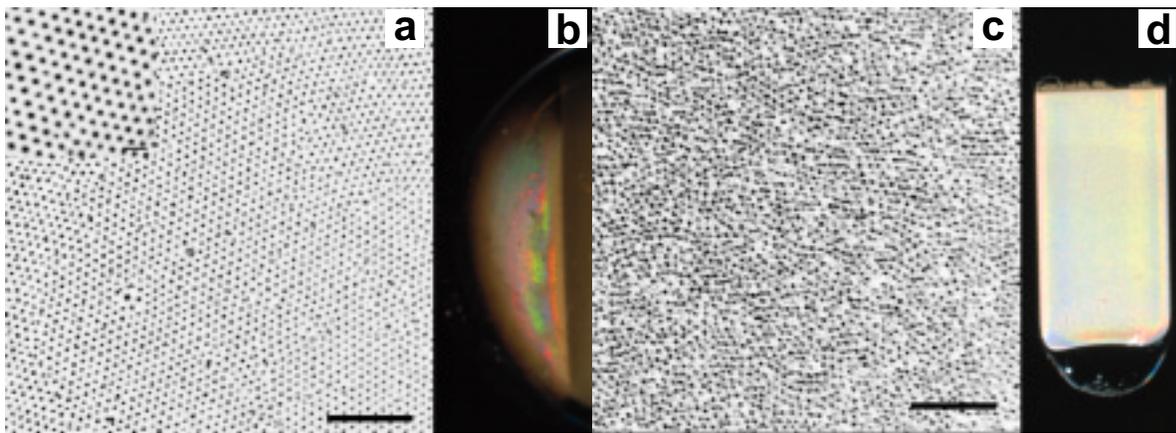


**Figure III.1–6** Confocal images (a, c) in reflection mode ( $\lambda = 632 \text{ nm}$ ) and optical photographs (b, d), under illumination with white light, of samples of Ag particles dispersed in water. (a) Charged-stabilized crystal of silver spheres in water ( $R = 257 \text{ nm}$ ,  $\delta = 17\%$ ). The spacing between the particles is  $\sim 1 \mu\text{m}$ . The scale bar is  $10 \mu\text{m}$ . The inset shows a single crystal domain. The inset scale bar is  $2 \mu\text{m}$ . (b) Reflection colors from a charge-stabilized crystal formed at the round bottom of a glass flask (the picture is rotated  $90^\circ$  clockwise). (c) Amorphous glass-like sample of Ag particles ( $R = 418 \text{ nm}$ ,  $\delta = 13\%$ ). The scale bar is  $10 \mu\text{m}$ . (d) Diffuse reflection colors from a colloidal glass formed in thin glass capillary.

surface charge, ionic strength, and the particle diameter. Based on the symmetry of the first layer (we could not image the second layer), we expect the crystal to be face-centered-cubic (*fcc*).

When we tried to grow colloidal crystals in a capillary, we only obtained amorphous, glass-like, arrangements of spheres (Fig. III.1–6c, d). This was caused both by the fact that it is harder to keep the ionic strength sufficiently low in a capillary and by the increased weight of silver dispersion compressing the system. The particles described in the present paper can therefore not be crystallized at the volume fractions that are necessary ( $> 50\%$ ) to open up a CPBG.<sup>10</sup> In the glassy sample only short-range order remains. In both cases, however, these structures display reflection colors when the samples are illuminated with white light. In the case of a crystal (Fig. III.1–6b) these colors are much brighter in contrast to the colloidal glass where the colors are more diffuse (Fig. III.1–6d). The optical characterization of these glasses and crystals is described in Chapter III.2.<sup>51</sup>

## Conclusions

In conclusion, we developed a method to synthesize large silver colloidal particles with radii larger than 100 nm via controlled aggregation of silver nanocrystals. The final particle radius can be controlled by the pH of the reaction mixture and the concentration of the reactants. The resulting particles are spherical aggregates with a low polydispersity ( $< 20\%$ ) and surface roughness on the order of 10 nm, as determined by electron microscopy. Good correspondence with scattering theory was found when an effective dielectric constant modeled by the Bruggeman effective medium model was used. The porosity of the particles was in the range of 15–25%. At low volume fraction the silver particles could be crystallized in charged stabilized colloidal crystals. At higher volume fractions only glassy structures were obtained.

## Acknowledgements

We thank Alexander Moroz (Utrecht University) for inspiring this research and Paul van Ekeren (Utrecht University) for performing the TGA analysis.

---

## References

- (1) Gates, B. C.; Guezi, L.; Knosinger, H. *Metal clusters in catalysis*; Elsevier: Amsterdam, 1986.
- (2) Jana, N. R.; Sau, T. K.; Pal, T. *J. Phys. Chem. B* **1999**, *103*, 115.
- (3) Elghanian, R.; Storhoff, J. J.; Mucic, R. C.; Letsinger, R. L.; Mirkin, C. A. *Science* **1997**, *277*, 1078.
- (4) Olsen, A. W.; Kafafi, Z. H. *J. Am. Chem. Soc.* **1991**, *113*, 7758.

- (5) Ganeev, R. A.; Ryasnyanskii, A. I.; Kodirov, M. K.; Kamalov, S. R.; Usmanov, T. *Opt. Spectrosc.* **2001**, *90*, 568.
- (6) Ganeev, R. A.; Ryasnyansky, A. I.; Kamalov, S. R.; Kodirov, M. K.; Usmanov, T. *J. Phys. D-Appl. Phys.* **2001**, *34*, 1602.
- (7) Kambhampati, D. K.; Knoll, W. *Curr. Opin. Colloid Interface Sci.* **1999**, *4*, 273.
- (8) Nie, S. M.; Emery, S. R. *Science* **1997**, *275*, 1102.
- (9) Tominaga, J.; Mihalcea, C.; Buchel, D.; Fukuda, H.; Nakano, T.; Atoda, N.; Fuji, H.; Kikukawa, T. *Appl. Phys. Lett.* **2001**, *78*, 2417.
- (10) Moroz, A. *Phys. Rev. Lett.* **1999**, *83*, 5274.
- (11) Moroz, A. *Europhys. Lett.* **2000**, *50*, 466.
- (12) Zhang, W. Y.; Lei, X. Y.; Wang, Z. L.; Zheng, D. G.; Tam, W. Y.; Chan, C. T.; Sheng, P. *Phys. Rev. Lett.* **2000**, *84*, 2853.
- (13) El-Kady, I.; Sigalas, M. M.; Biswas, R.; Ho, K. M.; Soukoulis, C. M. *Phys. Rev. B* **2000**, *62*, 15299.
- (14) Wang, Z.; Chan, C. T.; Zhang, W.; Ming, N.; Sheng, P. *Phys. Rev. B* **2001**, 113108.
- (15) Yablonoitch, E. *Phys. Rev. Lett.* **1987**, *58*, 2059.
- (16) John, S. *Phys. Rev. Lett.* **1987**, *58*, 2486.
- (17) Bykov, V. P. *Sov. J. Quantum Electron.* **1975**, *4*, 861.
- (18) Biswas, R.; Sigalas, M. M.; Subramania, G.; Ho, K. M. *Phys. Rev. B-Condens Matter* **1998**, *57*, 3701.
- (19) Busch, K.; John, S. *Phys. Rev. E* **1998**, *58*, 3896.
- (20) Moroz, A. *submitted* **2001**.
- (21) Goia, D. V.; Matijevic, E. *New J. Chem.* **1998**, *22*, 1203.
- (22) Adair, J. H.; Li, T.; Kido, T.; Havey, K.; Moon, J.; Mecholsky, J.; Morrone, A.; Talham, D. R.; Ludwig, M. H.; Wang, L. *Mater. Sci. Eng. R-Rep.* **1998**, *23*, 139.
- (23) Adair, J. H.; Suvaci, E. *Curr. Opin. Colloid Interface Sci.* **2000**, *5*, 160.
- (24) Mayer, A. B. R.; Hausner, S. H.; Mark, J. E. *Polym. J.* **2000**, *32*, 15.
- (25) Chou, K. S.; Ren, C. Y. *Mater. Chem. Phys.* **2000**, *64*, 241.
- (26) Hachisu, S. *Croatica Chemica Acta* **1998**, *71*, 975.
- (27) Taleb, A.; Petit, C.; Pileni, M. P. *Chem. Mat.* **1997**, *9*, 950.
- (28) Egorova, E. M.; Revina, A. A. *Colloid Surf. A-Physicochem. Eng. Asp.* **2000**, *168*, 87.
- (29) Rodriguez-Sanchez, L.; Blanco, M. C.; Lopez-Quintela, M. A. *J. Phys. Chem. B* **2000**, *104*, 9683.
- (30) Zhu, J. J.; Liu, S. W.; Palchik, O.; Koltypin, Y.; Gedanken, A. *Langmuir* **2000**, *16*, 6396.
- (31) Matijevic, E. *Chem. Mat.* **1993**, *5*, 412.
- (32) Matijevic, E. *Langmuir* **1994**, *10*, 8.
- (33) Mulvaney, P.; Giersig, M.; Henglein, A. *J. Phys. Chem.* **1993**, *97*, 7061.
- (34) Torigoe, K.; Nakajima, Y.; Esumi, K. *J. Phys. Chem.* **1993**, *97*, 8304.
- (35) Link, S.; Wang, Z. L.; El-Sayed, M. A. *J. Phys. Chem. B* **1999**, *103*, 3529.
- (36) David, R. L. *Handbook of chemistry and physics*; 76 th ed.; CRC Press, 1995-1996.

- (37) Wang, W.; Efrima, S.; Regev, O. *Langmuir* **1998**, *14*, 602.
- (38) Bright, R. M.; Musick, M. D.; Natan, M. J. *Langmuir* **1998**, *14*, 5695.
- (39) Liz-Marzan, L. M.; LadoTourino, I. *Langmuir* **1996**, *12*, 3585.
- (40) The original source can be found at <http://climate.gsfc.nasa.gov/~wiscombe/>
- (41) Goia, D. V.; Matijevic, E. *Colloid Surf. A-Physicochem. Eng. Asp.* **1999**, *146*, 139.
- (42) Privman, V.; Goia, D. V.; Park, J.; Matijevic, E. *J. Colloid Interface Sci.* **1999**, *213*, 36.
- (43) Bogush, G. H.; Zukoski, C. F. *J. Colloid Interface Sci.* **1991**, *142*, 19.
- (44) Napper, D. H. *Polymeric stabilization of colloidal dispersions*; Academic Press: London, 1983.
- (45) Jana, N. R.; Gearheart, L.; Murphy, C. J. *Chem. Mat.* **2001**, *13*, 2313.
- (46) Jonson, P. B.; Christy, R. W. *Phys. Rev. Lett.* **1972**, *6*, 4370.
- (47) Bohren, C. F.; Huffman, D. R. *Absorption and scattering of light by small particles*; Wiley: New York, 1983.
- (48) Kreibig, U.; Vollmer, M. *Optical properties of metal clusters*; Springer: Berlin, 1995.
- (49) Kofke, D. A.; Bolhuis, P. G. *Phys. Rev. E* **1999**, *59*, 618.
- (50) Auer, S.; Frenkel, D. *Nature* **2001**, *413*, 711.
- (51) Velikov, K. P.; Vos, W. L.; Moroz, A.; van Blaaderen, A. *in preparation* **2002**.



---

## III.2 Photonic Glasses of Colloidal Silver Particles

We report on the fabrication and optical reflection studies of photonic glasses of metallo-dielectric colloidal silver spheres with particle sizes comparable to the wavelength of visible light dispersed in a dielectric host. Polydisperse silver particles readily form colloidal glasses when sedimented in water, as indicated by reflection microscopy. Strong modulations in optical specular and off-specular reflectivity curves were found for these glasses. Our results suggest that some applications in which spontaneous emission of light needs to be modified might be performed with metallo-dielectric glasses.

## Introduction

Photonic crystals are materials with a periodic dielectric permittivity. When light travels in a photonic crystal, it can be diffracted by the periodic dielectric constant leading to a formation of stop gaps.<sup>1-3</sup> This diffraction is analogous to how the flow of electrons is influenced by the positively charged atoms in a metal or semiconductor crystal lattice. A complete photonic band gap (CPBG) can be formed if the stop gaps overlap for all directions of propagation and for all polarizations. Metallo-dielectric photonic crystals have been proposed recently as a possible candidate for achieving a CPBG in the optical or visible wavelength range.<sup>4,5</sup> Theoretical studies have shown that a CPBG can form in crystals with many different symmetries.<sup>5</sup> In addition, the gap appears to be more robust against disorder than for purely dielectric photonic crystals. Disorder is always present in dielectric photonic crystals made using self-assembling methods and it was found to play a critical role in determining their photonic properties.<sup>6,7</sup> For instance, the CPBG in an inverted air-sphere crystal is strongly affected, and in some cases can be closed, by the presence of disorder (e.g., caused by polydispersity of the spheres used in the initial template).<sup>8,9</sup> Stacking faults in finite crystals, the other very common type of disorder, were found to introduce localized states within the CPBG.<sup>10</sup>

Amorphous semiconductors, like silicon, do possess an electric band gap despite the absence of long-range order. It is interesting to see to what extent this also holds for photonic glasses. In a two-dimensional (2D) calculation for purely dielectric scatters, a low lying gap survived even in the case of short-range ordered, glassy, structures.<sup>11</sup>

Colloidal glasses have short-range order and have been studied extensively as a model system for the glass transition.<sup>12</sup> The photonic properties of colloidal glasses are hardly studied<sup>13</sup> mainly because of difficulties in comparison with theoretical calculations. The experimental study of metallo-dielectric systems with short-range order will give a significant contribution in understanding how the photonic properties are affected by disorder. In addition, as Arya *et al.* suggested, randomly distributed metal particles in a dielectric host might be a suitable system to study light localization.<sup>14,15</sup> Finally, from a practical point of view, it is easier and cheaper to fabricate amorphous, glass-like, photonic materials than crystals.

In this Chapter, we report on the fabrication and optical reflection measurements of photonic glasses with a varying degree of order made of polydisperse silver (Ag) colloidal particles in water. All samples were found to display bright colors when illuminated with white light. Wavelength-resolved and angle-resolved optical reflection measurements were performed to quantify the modulations in the reflectivity.

## Experimental Section

**Sample Preparation.** Silver particles with different radii (Table III.2-1) were prepared as described in Chapter III.1.<sup>16</sup> The particles were characterized by transmission electron microscopy (TEM) (Philips CM10) and by scanning electron microscopy (SEM) (Philips XL30). The particle size and polydispersity were determined from TEM micrographs using a Nikon profile projector. Extinction spectra of single particles were measured on a Cary 1E UV-Vis spectrophotometer using dilute ( $< 10^{-5}$  vol. %) aqueous suspensions. Theoretical extinction spectra of single particles were calculated using a FORTRAN program, based on an algorithm of Wiscombe,<sup>17</sup> modified to take the sphere size polydispersity into account. Samples for reflection measurements were prepared both in little glass vials (1.7 ml), of which the bottom was replaced by a microscope cover slip (Chance Propper) with a thickness of 0.15 mm, and in thin (0.20 mm) glass capillaries (VitroCom).

Table III.2-1 Radius ( $R$ ) and polydispersity ( $\delta$ ) of silver particles obtained as determined by TEM.

Sample	$R$ (nm)	$\delta$ (%)
Ag 67	197	13
Ag 18	320	15
Ag 28	349	16
Ag 68	383	13
Ag 23	418	12
Ag 66	284	15
Ag 57	560	23
Ag 6.1	626	25
Ag 32b	257	17

**Confocal Microscopy.** To examine the microscopic structure of the samples, we used a confocal microscope operating in reflection mode. Samples in water were observed in reflection mode ( $\lambda = 632$  nm) with an inverted confocal microscope (Leica DM IRB, in combination with a Leica TCS NT scanhead) with an oil-immersion lens (Leica, 100 $\times$ , NA 1.4). Vertically standing capillaries were examined with the microscope tilted at 90°. Because of the strong interaction of the silver particles with light, only the first layer of particles, in contact with the glass wall, could be imaged. Based on the fact that all dispersions were easily redispersed upon shaking, and therefore were not irreversibly aggregated, we assume that the structure observed close to the wall extends through the whole sample.

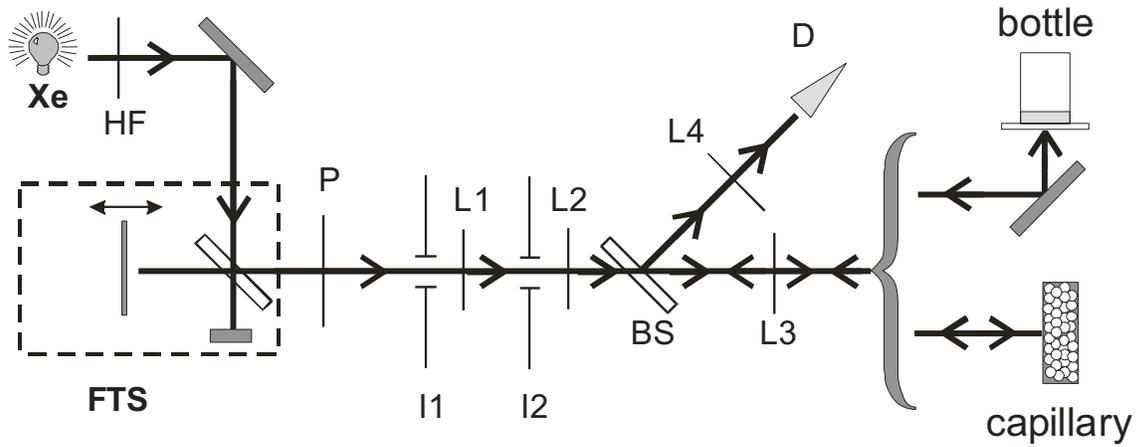


**Figure III.2-1** Schematic drawing of the reflectivity set up. L1, L2, L3, and L4 are lenses ( $f_{L1} = 75$  mm,  $f_{L2} = 75$  mm,  $f_{L3} = 150$  mm and  $f_{L4} = 50$ ), P is a polarizer to suppress He-Ne emission, I1 and I2 are irises for beam attenuation, FTS is a Fourier-transform spectrometer, BS is a beam splitter, HF is a thermal filter, and D is a Si diode detector.

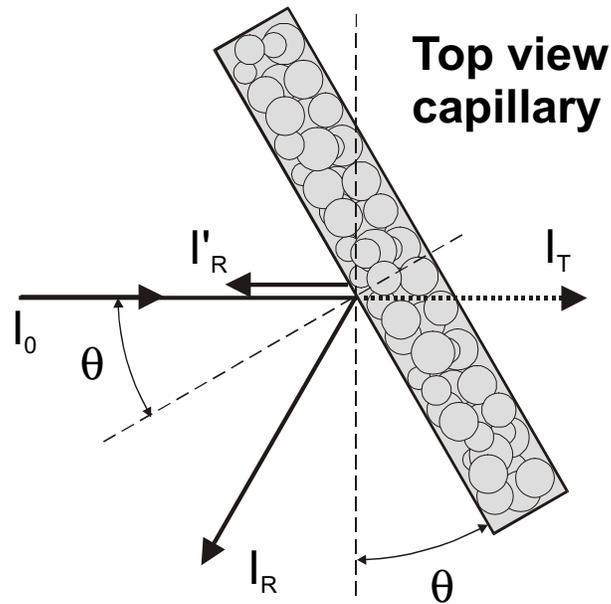


**Figure III.2-2** Top view of the beam configuration for off-specular angle-resolved reflectivity measurements on capillaries.

**Reflectivity Measurements.** The setup for the frequency resolved reflection measurements is similar to that described in Ref. 18 and is depicted in Fig. III.2-1. The output of a broad-band xenon lamp is focused on a pinhole, which acts as a point source. The light is collimated and sent through a Fourier-transform interferometer (Biorad FTS-60A) operating with a spectral resolution of  $16 \text{ cm}^{-1}$ . The light beam is focused to a  $0.5 \text{ mm}$  diameter spot on the sample. The samples in a capillary were mounted vertically on a goniometer head to align the face of a capillary to the incident beam. The beam configuration for the angle-resolved off-specular reflectivity measurements is shown in Fig. III.2-2. The measured off-specular reflectivity is defined as the ratio between the incoming light beam  $I_0$  and the back reflected  $I'_R(\theta)$  light. At  $\theta = 0$  (normal incidence) the off-specular reflectance coincides with the specular reflectance. The samples in small bottles were placed horizontally on a holder and the reflectivity was measured only at normal incidence from the flat bottom. The reflected light is collected by a Si diode, which yields an interferogram that is Fourier transformed to get the spectrum of the reflected light. The spectra were referenced to those of a silver mirror with  $> 95\%$  reflectivity.

## Results and Discussion

Figure III.2-3 shows optical photographs of capillaries filled with silver particles of different sizes sedimented in water. Under illumination with white light, these samples display bright colors at almost all angles of observation. The brightness of the colors, however, is not as sharp as in the case of colloidal crystals of these

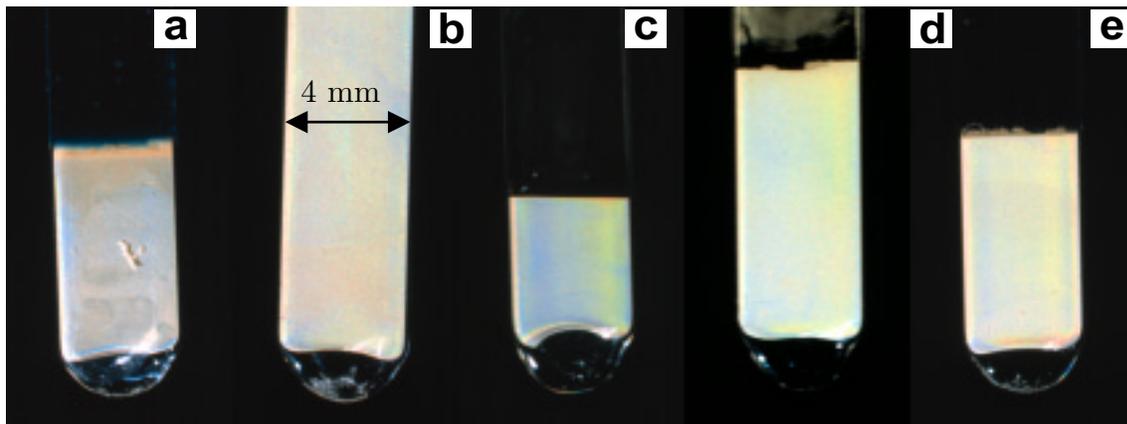


**Figure III.2-3** Optical photographs of capillaries filled with sedimented in water silver particles with different radii ( $R$ ): (a) Sample Ag 67, ( $R = 197 \text{ nm}$ ); (b) Sample Ag 18, ( $R = 320 \text{ nm}$ ); (c) Sample Ag 28, ( $R = 349 \text{ nm}$ ); (d) Sample Ag 68, ( $R = 383 \text{ nm}$ ); (e) Sample Ag 23, ( $R = 418 \text{ nm}$ ). All samples display bright reflection colors under illumination with white light.

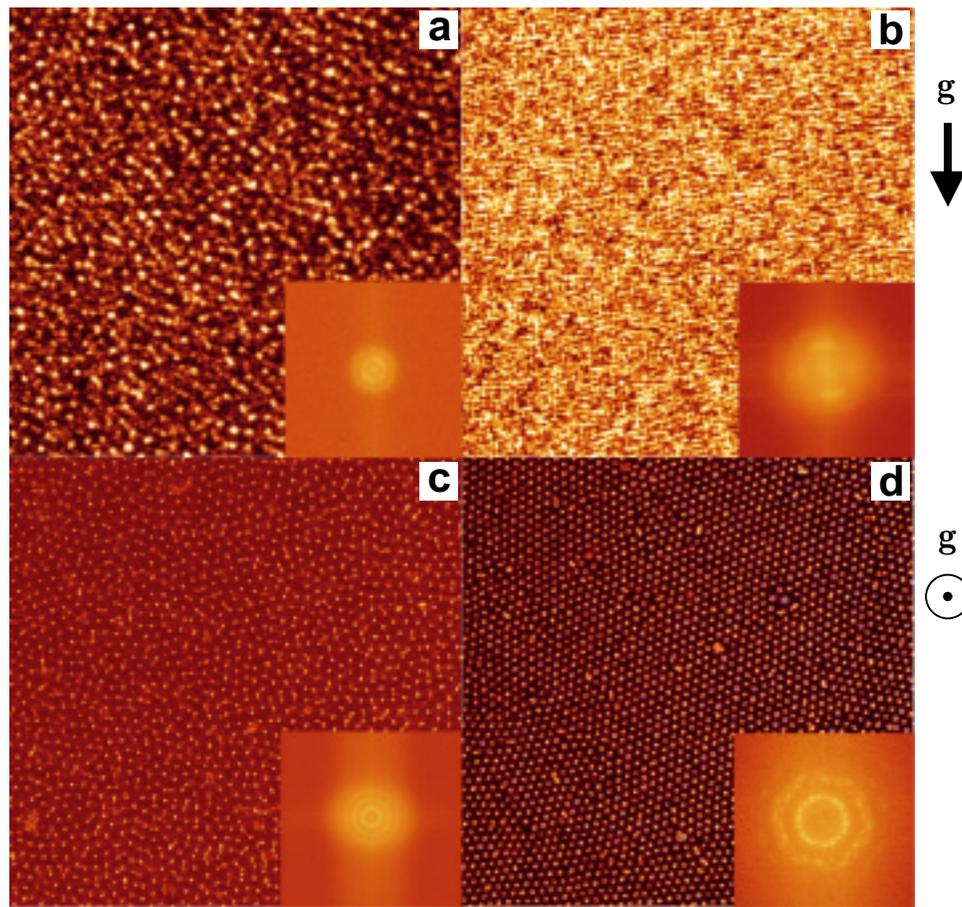


**Figure III.2-4** Reflection confocal images of Ag particles dispersed in water displaying different degree of order: (a) Sample Ag 23 in capillary ( $R = 418$  nm); (b) Sample Ag 66 in capillary ( $R = 284$  nm); (c) Sample Ag 28 in bottle ( $R = 349$  nm); (d) Sample Ag 32b in bottle ( $R = 257$  nm). The insets show Fourier transformation (FFT) of the images.

particles (for a macroscopic photo of the crystals see Chapter III.1). This feature already hints at a decrease of the order in the samples shown in Fig. III.2-3.

The structure of samples was studied by reflection confocal microscopy. Figure III.2-4 shows images of samples displaying different degrees of order. Because of the strong interaction of the silver particles with light, particles that are deeper inside the sample could not be imaged as the point spread function of the microscope is already completely scrambled after the first layer. Nevertheless, in analogy to hard-sphere and charge-stabilized colloidal glasses of fluorescent particles studied by confocal microscopy, we can assume that the same structure extends through the whole sample. The brightest spots in the images correspond to particles that are closest to the glass wall. The less bright particles are not in contact with the wall. The first two pictures (Fig. III.2-4a, b) are taken at the wall of vertically placed capillaries. Pictures in Fig. III.2-4c and III.2-4d are taken at the bottom of a bottle containing

sedimented particles. The first three samples are amorphous with different degree of disorder. The ring-like patterns in the Fourier transformed (FFT) images, shown in the insets (Fig. III.2–4a, b, c), also indicate the presence of short-range order only. The appearance of a second ring in Fig. III.2–4c indicates that the particles in the bottles are more ordered as is also obvious from the real-space picture. Confocal images were taken at different heights in the sediments in the capillaries.

Unfortunately, because of the fact that we can image only the particles closest to the wall, because of the strong degradation of the point spread function with depth, and the fact that for the glasses in the capillaries these particles are not arranged in perfect layers, it was hard to obtain the average interparticle distance in the glasses accurately. By measuring distances between particles that are close to each other and close to the wall, we were able to get an estimate of the interparticle distance. From such a distance follows an effective radius that is the sum of the particle radius and a distance due to charge repulsion. The volume fraction of such effective spheres is assumed to be random close-packed (63%). This then gives an estimate of the Ag volume fraction. It is important to note here that for all samples the metal spheres were not in (conducting) contact with each other, contrary to recently prepared 'inverse' photonic metallic crystals.<sup>19,20</sup>

The last image shows a crystalline region displaying long-range order and strong particle layering. The determination of the interparticle distance in such sample is relatively easy. The FFT image also clearly shows the six-fold symmetry. The estimated mean interparticle distance in the samples in the bottles is much larger ( $\sim 1 \mu\text{m}$ ) than in the capillaries due to the lower ionic strength and the reduced pressure. The amount of silver pressing down on the layer observed in the bottles was much less than in the capillaries. Thus, the volume fraction of glasses formed in the bottles is lower than in the capillaries.

Reflectivity measurements at normal incidence were done both on samples in capillaries and in bottles. Figure III.2–5 shows reflectivity spectra measured at normal incidence on samples in capillaries containing particles of different sizes. Strong modulation in the reflectivity appears in a range of wavelengths in the visible. However, no sharp peaks are observed as expected from calculations on perfect (*fcc*) crystals using the Korringa-Kohn-Rostoker (KKR) method.<sup>21</sup> The reflectivity shows a significant dependence on crystals volume fraction, which is related to the height in the sample as observed with dielectric particles.<sup>22</sup> Except for the smaller size particles (Fig. III.2–5a), all samples display an increase of the reflectivity above 600 nm. For large sizes and higher packing fraction (close to the sample bottom) this upturn disappears (Fig. III.2–5e, f). In some samples (Fig. III.2–5c, d), a clear maximum in the reflectivity is observed.

The reflectivity measured on samples in bottles (Ag 23 and 28) show a variety of curves depending on the position of measurement (Fig. III.2–6).

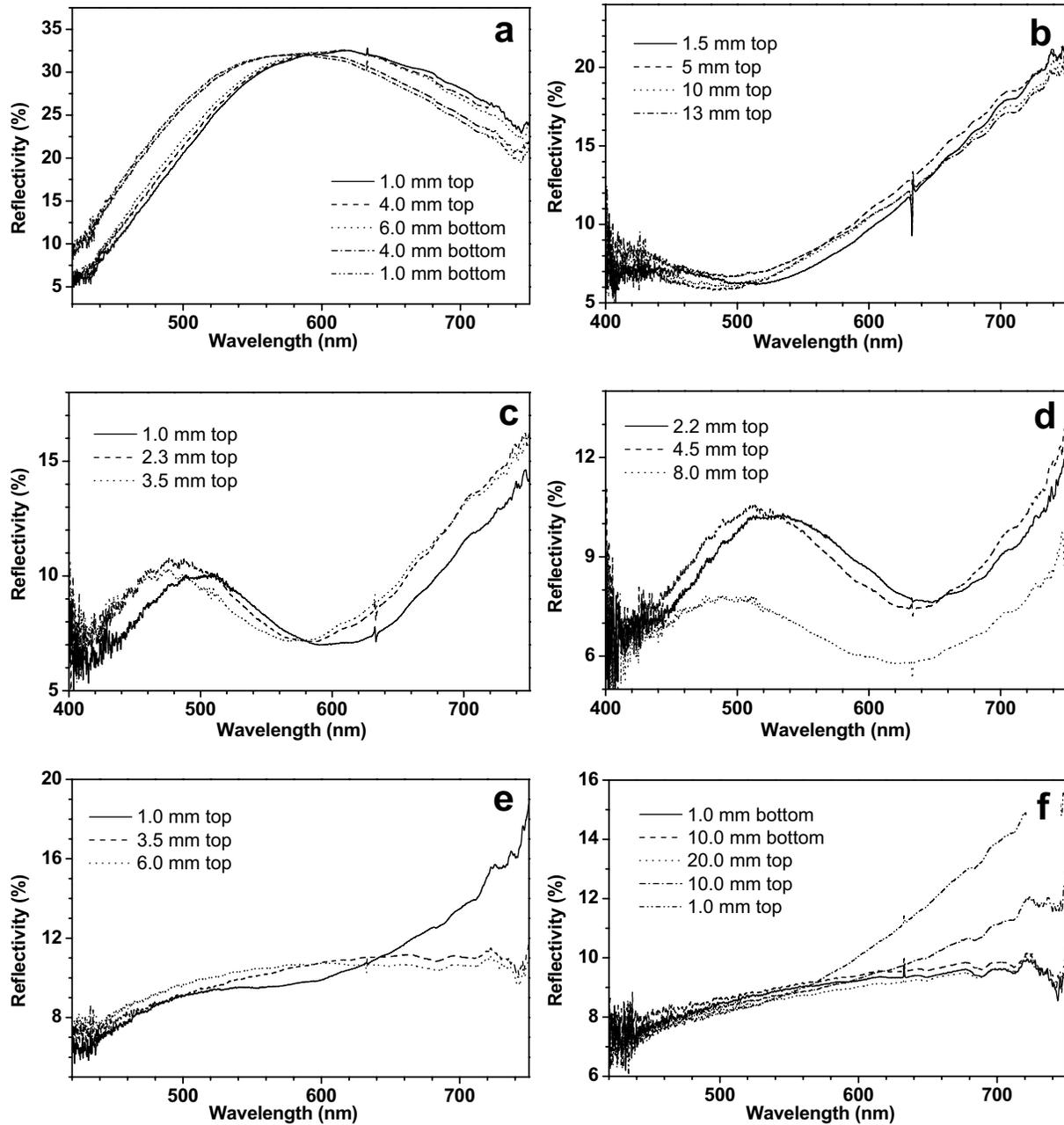


**Figure III.2-5** Optical reflectivity at normal incidence as a function of wavelength of samples with different total height ( $h$ ) of the sediment in capillaries containing particles with different radii ( $R$ ): (a) Sample Ag 67 ( $R = 197$  nm,  $h = 7$  mm); (b) Sample Ag 66 ( $R = 284$  nm,  $h = 15$  mm); (c) Sample Ag 28 ( $R = 349$  nm,  $h = 5$  mm); (d) Sample Ag 23 ( $R = 418$  nm,  $h = 8$  mm); (e) Sample Ag 57 ( $R = 560$  nm,  $h = 7$  mm); (f) Sample Ag 6.1 ( $R = 626$  nm,  $h = 38$  mm). Different curves correspond to measurements at different distances from the top or from the bottom of the sample, giving an indication of changes as a function of the volume fraction.

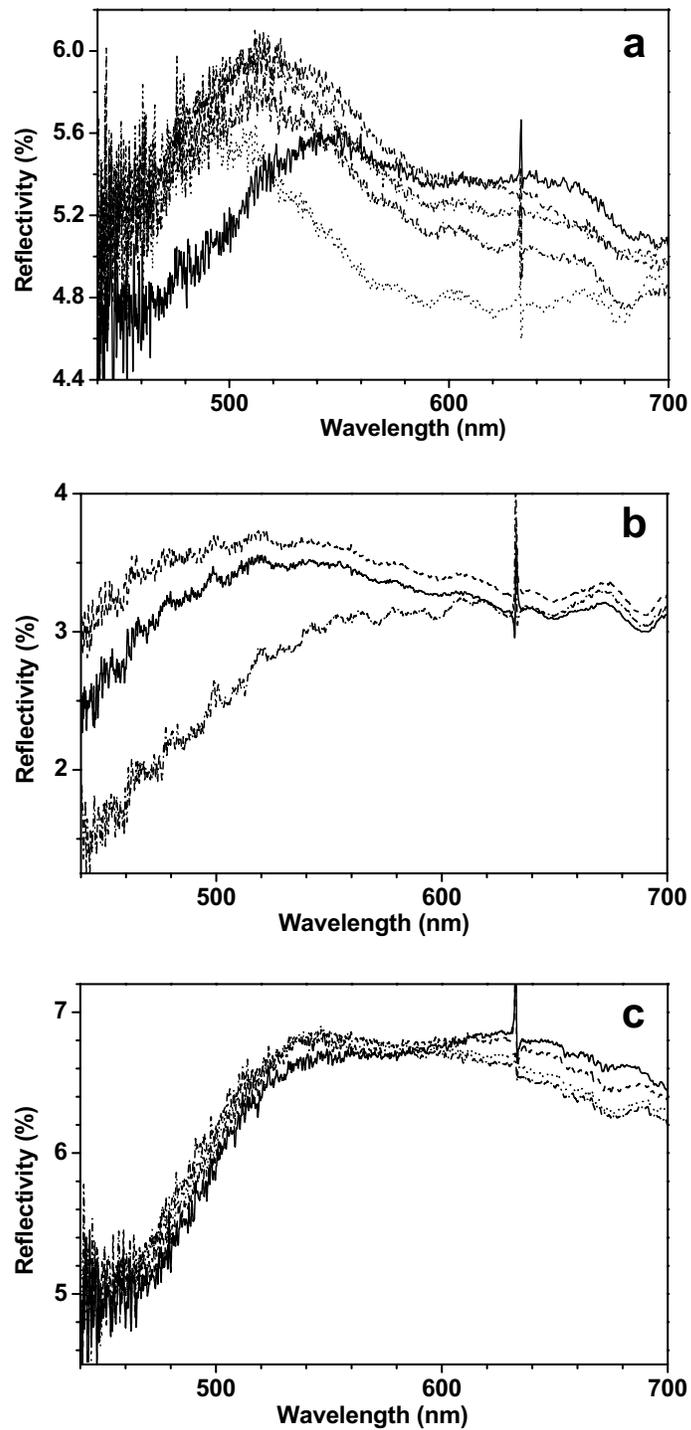


**Figure III.2-6** Optical reflectivity at normal incidence as a function of wavelength of samples in bottles containing particles of different radii ( $R$ ): (a) and (b) two different bottles containing sample Ag 28 ( $R = 349$  nm); (c) Sample Ag 23 ( $R = 418$  nm). Different curves correspond to measurement on different spots of the bottom of the samples, giving an indication of the variation in spectra caused by a different amount of order.

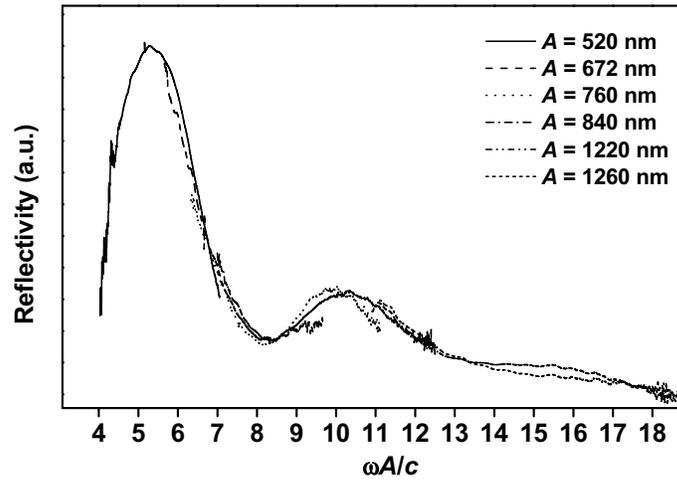


**Figure III.2-7** Relative reflectivity at normal incidence for samples from Fig. III.2-5 as a function of the scaled frequency,  $\omega A/c$ .

The different reflectivity curves, which correspond to different positions in the sample, are probably taken on regions with different amount of order as was also observed with the confocal microscope. Sample Ag 28 (Fig. III.2-6c) had a uniform degree of order over the whole bottom area. Therefore, the reflectivity curves are similar. The other two samples had a much more variable degree of ordering. The absolute value of the reflectivity of the samples shown in Fig. III.2-6 is lower than the reflectivity of the capillaries. Probably, this is due to the lower filling fraction of the glasses. Because of the long crystallization time and fragility of charge-stabilized crystals, we have not measured reflectivity on samples as ordered as shown in Fig. III.2-4d.

In order to see to what extent the scattering of the metallo-dielectric photonic glasses scales with the volume fraction and interparticle particle distance, we plotted the reflectivity measured on samples in capillaries as a function of the scaled frequency,  $\omega A/c$ , where  $A$  is the mean interparticle distance, and  $c$  is the speed of light. The mean interparticle distance was determined with relatively large error ( $\sim 15\%$ ) by confocal observations. Figure III.2-7 shows scaled reflectivity spectra taken close to the top of the sediment in the capillary. All spectra seem to lie on a common curve with a series of maxima which appear to have a period. This scaling behavior is not expected as silver has a strongly wavelength-dependent dielectric constant.

To see if we could find this behavior also for *fcc* crystals of silver spheres, we performed numerical calculations using the layer KKR method.<sup>23</sup> We performed calculations for six layers only, which was sufficient for convergence and the reflectivity did not change with increasing number of layers.

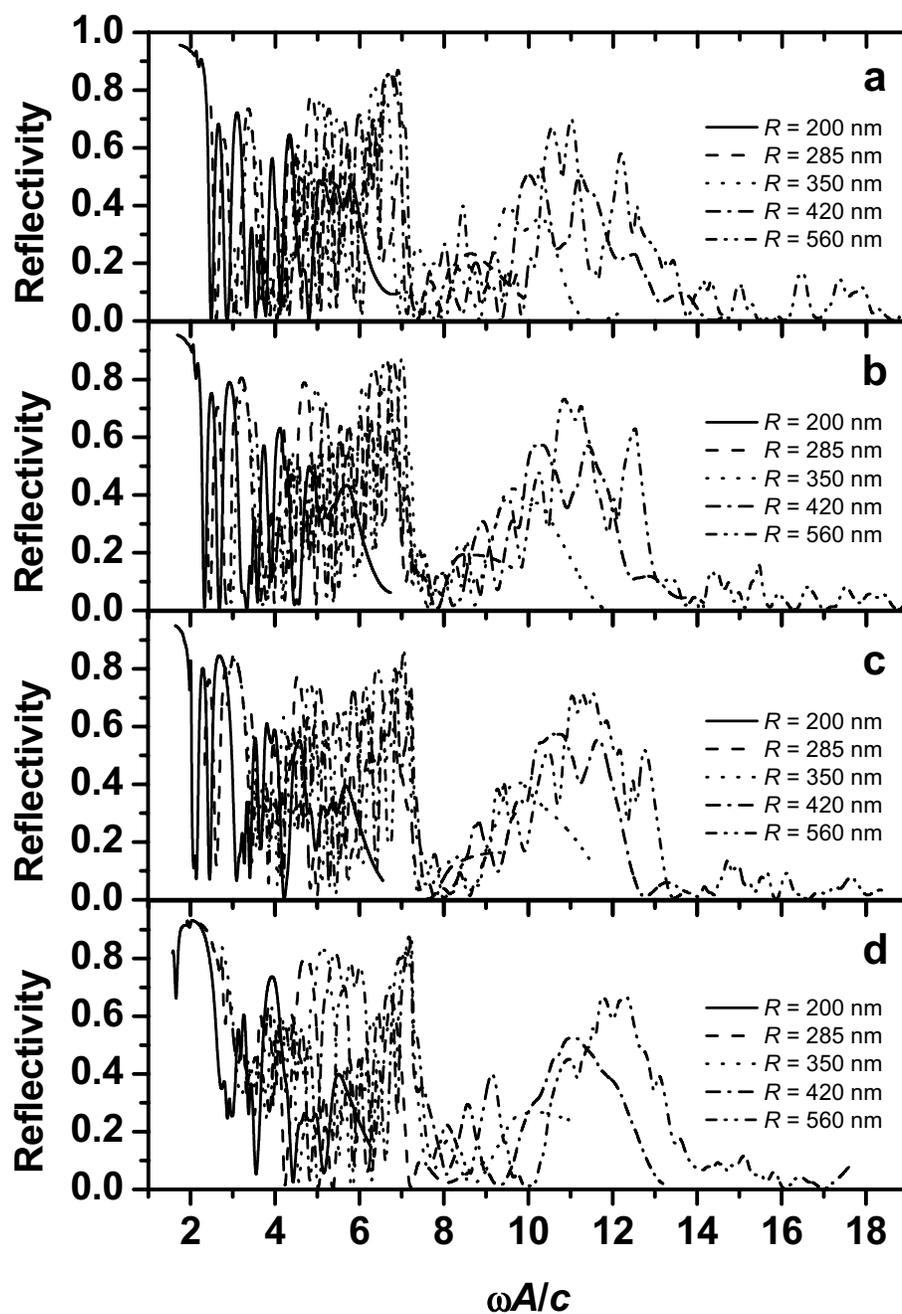


**Figure III.2-8** Theoretical reflectivity spectra along the (111) crystallographic axis as a function of the scaled frequency,  $\omega A/c$ , for a six-layer *fcc* crystal of Ag particles with different sizes. The calculations were performed for different packing fractions ( $\phi$ ) of the crystal: (a)  $\phi = 55\%$ ; (b)  $\phi = 60\%$ ; (c)  $\phi = 65\%$ ; (d)  $\phi = 70\%$ .

Figure III.2–8 shows calculated specular reflectivity at normal incidence (111 – crystallographic plane) for six-layer thick *fcc* crystals with different volume fraction and different sphere sizes in host water. As Ag particles appear to be porous aggregates their dielectric properties are described by an effective dielectric function (see Chapter III.1). In the calculations, we used the Bruggeman effective medium model<sup>24</sup> to calculate the effective dielectric function of a silver-water composite

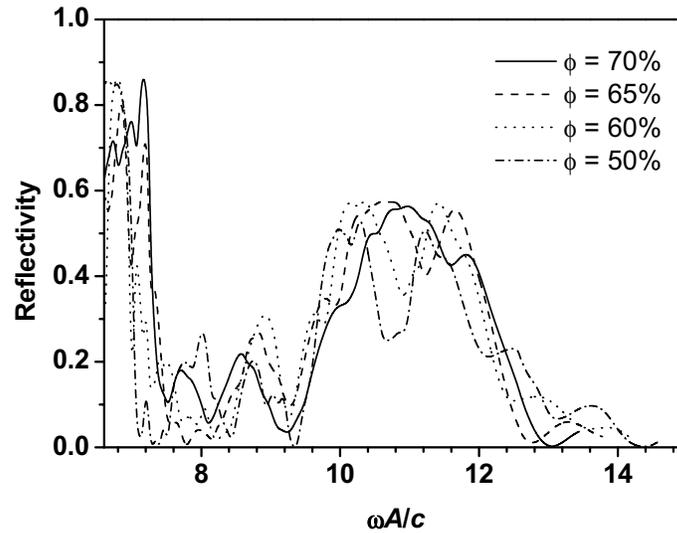


**Figure III.2–9** Theoretical reflectivity spectra along the (111) crystallographic axis as a function of the scaled frequency,  $\omega A/c$ , for a six-layer *fcc* crystal with different packing fraction ( $\phi$ ) made of sample Ag 23 ( $R = 418$  nm) particles.

assuming 80% bulk silver in one particle. As seen from the graphs, the 'global' and 'broad' features in reflectivity are not strongly dependent on the particle radius and even volume fraction. However, no exact scaling is possible. Roughly, we can identify a common up-swing around  $\omega = 2$  and, maximum in the region 3 – 7, and a broad lower maximum in the region 10 – 11. The last two maxima were also observed in the experimental spectra of the glasses (Fig. III.2–7). The samples of which the reflectivity is shown in Fig. III.2–7 have different volume fraction. However, as already mentioned, the 'broad' features of the reflectivity spectra are not too sensitive to the volume fraction. See Fig. III.2–9 where we plotted the scaled reflectivity (for the experimentally studied wavelengths: 400 – 800 nm) of sample Ag 23 calculated for different volume fractions.

As we have found similar behavior in the calculated scaled spectra for the *fcc* crystals and in the scaled experimental spectra for the glasses, it is no surprise that the same also holds for unscaled individual reflectivity curves. Here we show several

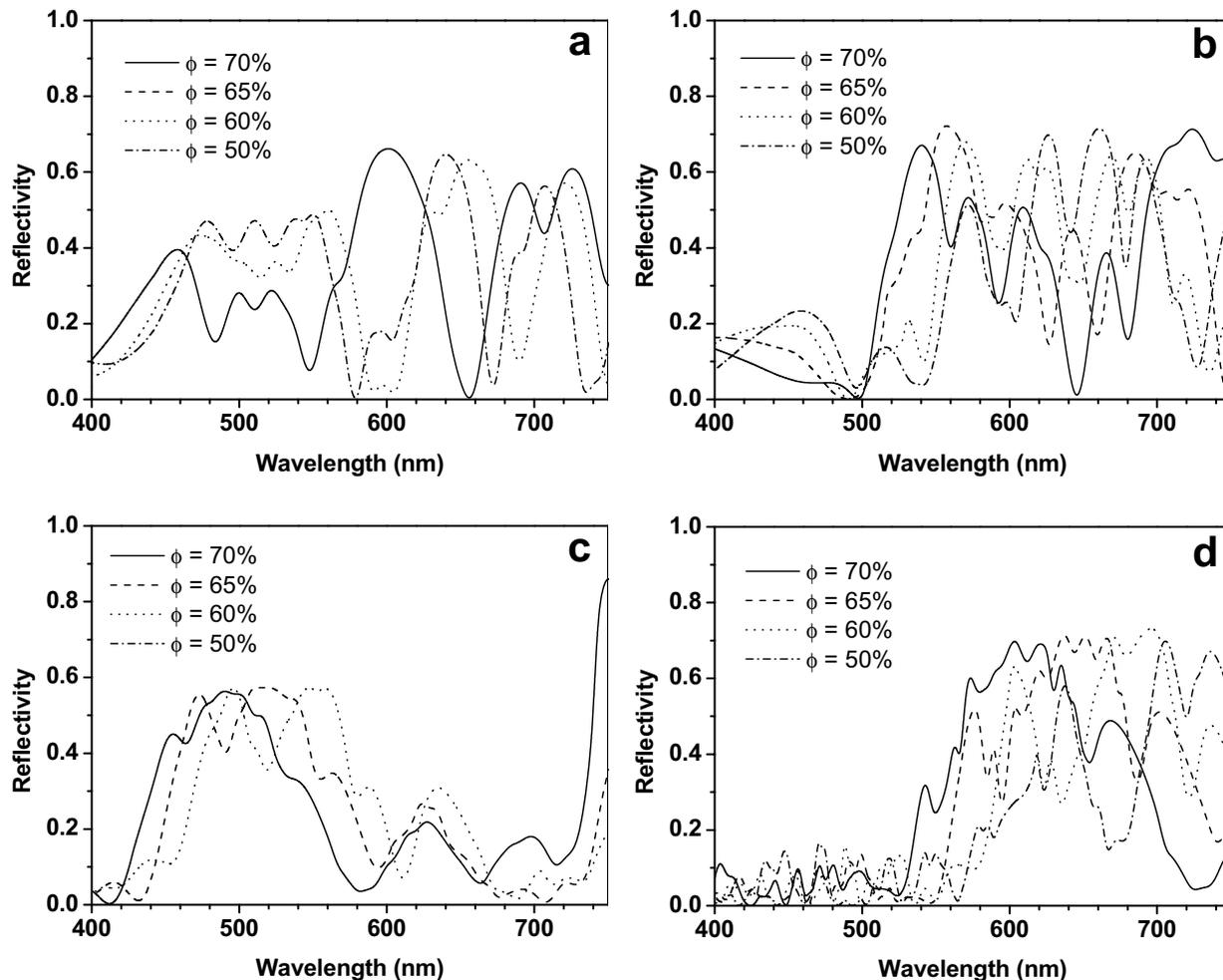


**Figure III.2-10** Theoretical reflectivity spectra along the (111) crystallographic axis as a function of the wavelength for a six-layer *fcc* crystal made of particles of different radii ( $R$ ) chosen to match the measured samples shown in Figs. III.2-5: (a)  $R = 200$  nm; (b)  $R = 285$  nm; (c)  $R = 420$  nm; (d)  $R = 560$  nm. The spectra were calculated for crystals with different packing fraction ( $\phi$ ).

examples. The first example is sample Ag 67, shown in Fig. III.2-10a, that features a broad maximum centered around 600 nm. Such a broad maximum is indeed experimentally observed (Fig. III.2-5a). In sample Ag 66 (Fig. III.2-10b) we can identify an initial relatively flat region and a minimum around 500 nm. However, the resemblance between the theoretical and experimental spectra (Fig. III.2-5b) is less clear.

In the next example, sample Ag 23 (Fig. III.2-10c), we can identify a maximum around 500 nm which was also observed in the amorphous sample (Fig. III.2-5d). At longer wavelengths the reflectivity increases, which was also observed for these particles in small bottles (Fig. III.2-6a). Furthermore, at lower filling

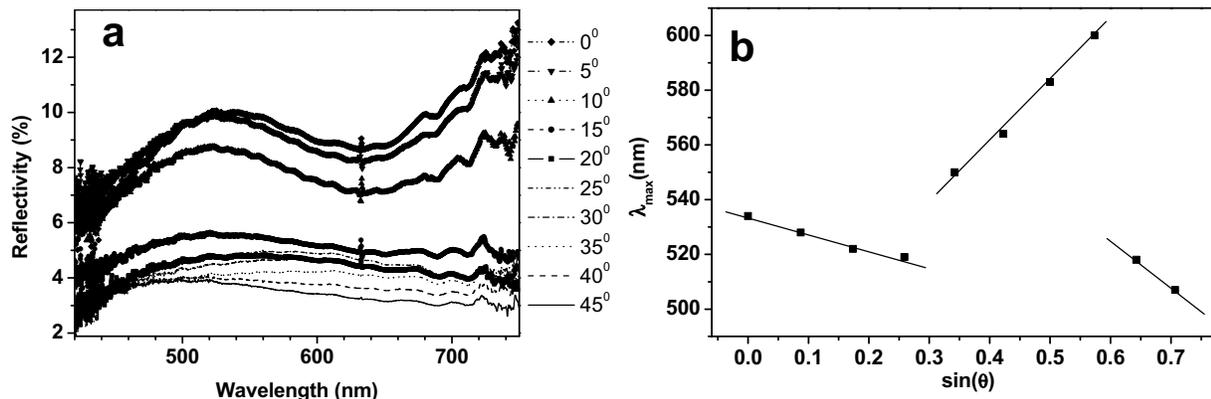


**Figure III.2-11** Off-specular optical reflectivity measurements (taken at 2.0 mm from the top of the sediment) on capillary containing particles Sample Ag 23 ( $R = 418$  nm) (a) Reflectivity as a function of wavelength measured at different angles with respect to the incoming beam (Fig. III.2-2). (b) Position of the maximum in the reflectivity as a function of  $\sin(\theta)$ . The lines are to guide the eye.

fraction this up-turn drastically decreases, which was also observed in the reflectivity measurements in less dense colloidal crystals in bottles (Fig. III.2-6a).

For the last example, sample Ag 57 (Fig. III.2-10d), we again see a correspondence between reflectivity in glasses and in the perfect crystal. Below  $\sim 500$  nm the reflectivity is low and flat, followed by an increase at longer wavelengths. Furthermore, our measurements show that at higher volume fraction (close to the bottom of the capillary), the up-turn in the reflectivity disappears. Instead one can identify a very broad maximum around 600 nm. Such a tendency can also be found in the reflectivity spectra for the *fcc* crystal, e.g., for volume fraction 60–70%. It is clear that exact calculations for disordered metallo-dielectric photonic crystals should be performed in order to make a quantitative comparison with the experimental data. Nevertheless, the analogy we found between the reflectivity spectra of ordered and disordered systems warrants further research and indicates strong modulations in the local density of photonic states that can be probed with fluorescent dyes.

We also performed some angle-resolved off-specular reflectivity measurements. Figure III.2-11 shows off-specular measurements on sample Ag 23 measured in a capillary. The reflectivity drops at angles larger than  $20^\circ$ . However, even at these angles a peak that shifts for different angles of incidence can be observed. This shift is shown in Fig. III.2-11b where the position of the reflectivity peak is plotted as a function of  $\sin(\theta)$ . This behavior is not fully understood and further research is needed.

## Conclusions

In summary, we studied the optical properties of metallo-dielectric photonic glasses of colloidal silver particles in water. These samples display bright colors, observable by naked eye, when illuminated with white light. We demonstrated experimentally the presence of a strongly modulated specular and off-specular reflectivity in photonic glasses caused by the presence of short-range order. We found that when the wavelength was scaled to the interparticle distance results a reflectivity spectra with a series of equidistant peaks. Qualitatively, the general features in the experimental spectra were found as well in reflectivity spectra calculated for *fcc* crystals. Our findings suggest that some applications in which spontaneous emission of light needs to be modified might be performed with amorphous metallo-dielectric materials.

## Acknowledgements

We are grateful to Gabby E. Zegers (Utrecht University) for the preparation of the silver colloidal particles and to Rudolf Sprik (University of Amsterdam) and Arnout Imhof (Utrecht University) for stimulating discussions.

---

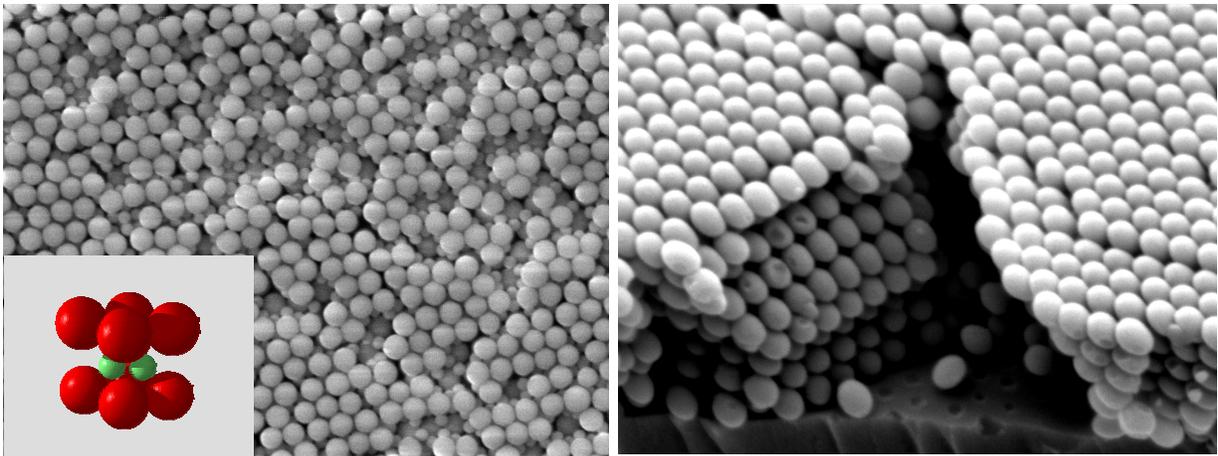
## References

- (1) Yablonovitch, E. *Phys. Rev. Lett.* **1987**, *58*, 2059.
- (2) Bykov, V. P. *Sov. J. Quantum Electron.* **1975**, *4*, 861.
- (3) Joannopoulos, J. D.; Meade, R. D.; Winn, J. N. *Photonic Crystals*; Princeton Univ. Press: Princeton, 1995.
- (4) Moroz, A. *Phys. Rev. Lett.* **1999**, *83*, 5274.
- (5) Zhang, W. Y.; Lei, X. Y.; Wang, Z. L.; Zheng, D. G.; Tam, W. Y.; Chan, C. T.; Sheng, P. *Phys. Rev. Lett.* **2000**, *84*, 2853.
- (6) Vlasov, Y. A.; Astratov, V. N.; Baryshev, A. V.; Kaplyanskii, A. A.; Karimov, O. Z.; Limonov, M. F. *Phys. Rev. E* **2000**, *61*, 5784.
- (7) Vlasov, Y. A.; Deutsch, M.; Norris, D. J. *Appl. Phys. Lett.* **2000**, *76*, 1627.
- (8) Li, Z. Y.; Zhang, Z. Q. *Phys. Rev. B* **2000**, *62*, 1516.
- (9) Biswas, R.; Sigalas, M. M.; Subramania, G.; Soukoulis, C. M.; Ho, K. M. *Phys. Rev. B* **2000**, *61*, 4549.
- (10) Yannopoulos, V.; Stefanou, N.; Modinos, A. *Phys. Rev. Lett.* **2001**, *86*, 4811.
- (11) Jin, C. J.; Meng, X. D.; Cheng, B. Y.; Li, Z. L.; Zhang, D. Z. *Phys. Rev. B* **2001**, *63*, 195107.
- (12) Kegel, W. K.; van Blaaderen, A. *Science* **2000**, *287*, 290. and references therein
- (13) Ballato, J.; Dimaio, J.; James, A.; Gulliver, E. *Appl. Phys. Lett.* **1999**, *75*, 1497.
- (14) Lee, S.-I.; Noh, T. W.; Cummings, K.; Gaines, J. R. *Phys. Rev. Lett.* **1985**, *55*, 1626.
- (15) Arya, K.; Su, Z. B.; Birman, J. L. *Phys. Rev. Lett.* **1986**, *57*, 2725.

- (16) Velikov, K. P.; Zegers, G. E.; van Blaaderen, A. *submitted* **2002**.
- (17) The original source can be found at <http://climate.gsfc.nasa.gov/~wiscombe/>
- (18) Thijssen, M. S.; Sprik, R.; Wijnhoven, J.; Megens, M.; Narayanan, T.; Legendijk, A.; Vos, W. L. *Phys. Rev. Lett.* **1999**, *83*, 2730.
- (19) Velez, O. D.; Tessier, P. M.; Lenhoff, A. M.; Kaler, E. W. *Nature* **1999**, *401*, 548.
- (20) Eradat, N.; Huang, J. D.; Vardeny, Z. V.; Zakhidov, A. A.; Khayrullin, I.; Udod, I.; Baughman, R. H. *Synth. Met.* **2001**, *116*, 501.
- (21) Moroz, A.; Sommers, C. *J. Phys.-Condes. Matter* **1999**, *11*, 997.
- (22) Vos, W. L.; Megens, M.; van Kats, C. M.; Bosecke, P. *J. Phys.-Condes. Matter* **1996**, *8*, 9503.
- (23) Stefanou, N.; Yannopapas, V.; Modinos, A. *Comput. Phys. Commun.* **1998**, *113*, 49.
- (24) Bohren, C. F.; Huffinan, D. R. *Absorption and scattering of light by small particles*; Wiley: New York, 1983.

## Part IV

# Photonic Colloidal Crystals with Complex Lattices and Shape-Anisotropic Particles





---

## IV.1 Layer-by-Layer Growth of Binary Colloidal Crystals

We report the growth of binary colloidal crystals with control over the crystal orientation through a simple layer-by-layer process. Well-ordered single binary colloidal crystals with a stoichiometry of large ( $L$ ) and small ( $S$ ) particles of  $LS_2$  and  $LS$  were generated. In addition, we observed the formation of a new  $LS_3$  superstructure. We can understand the structures formed from a combination of the templating effect of the first layer and the forces exerted by the surface tension of the drying liquid. Using spheres with different composition, one component can be selectively removed as is demonstrated in the growth of a hexagonal non-close-packed colloidal crystal. Our method will substantially expand the stoichiometries, possible compositions and symmetries achievable with colloidal crystals, because it does not rely on self-organization alone.

## Introduction

A mixture of submicron or colloidal particles of two sizes can self-organize into two- (2D)<sup>1</sup> and three-dimensional (3D)<sup>2-6</sup> binary crystals, which can have different stoichiometries and crystal symmetries depending on the size ratio and concentration. Binary colloidal crystals of large ( $L$ ) and small ( $S$ ) particles were first observed in nature. Two types of structures, with stoichiometry  $LS_2$  (atomic analog  $AlB_2$ ) and  $LS_{13}$  (atomic analog  $NaZn_{13}$ ), were found in Brazilian opals.<sup>3</sup> Later, binary crystals were observed in suspensions of charge-stabilized polystyrene<sup>4</sup> and of hard-sphere like PMMA<sup>5</sup> particles. Formation of small 2D binary crystals was observed in a mixture of alkanethiol-derivatized gold nanoparticles although it is unclear if the formation of these crystals was determined by thermodynamics alone.<sup>1</sup> Colloidal crystals with lattice constants comparable to the wavelength of visible light are important for applications and processes as diverse as photonic crystals,<sup>7</sup> (including structures with small refractive index contrast as in optical filters and switches<sup>8</sup>), chemical sensors,<sup>9</sup> lithography,<sup>10</sup> surface enhanced Raman scattering,<sup>11</sup> and the creation of macroporous materials.<sup>12-15</sup> However, binary crystals have not been investigated experimentally as extensively as one-component colloidal crystals mainly because it is harder to grow and characterize them.

Theoretically, it has been shown that entropy alone can lead to the formation of stable  $LS_2$  and  $LS_{13}$  binary crystals in bulk crystallization in a mixture of hard spheres of two sizes.<sup>6</sup> At higher particle concentrations packing arguments can be used to predict which crystal phase will form.<sup>2,3</sup> In bulk crystallization there is not much control over the size and orientation of single crystals. That is why for single crystals of one size particles methods like colloidal epitaxy<sup>16,17</sup> and a form of controlled drying on a substrate<sup>18-20</sup> have been developed. In this controlled drying technique, a colloidal crystal is formed at the drying front of an evaporating dispersion with a relatively low volume fraction of particles. Particles are transported to and concentrated at the drying edge by a fluid flow induced by the evaporation. The crystallization is not only driven by a lowering of the free energy but also under the influence of surface tension effects exerted on particles that are partially sticking through the drying meniscus<sup>20</sup> and the templating action of particles that are already deposited.<sup>16</sup> With this non-equilibrium process, it is possible to grow large single 2D<sup>21</sup> and 3D<sup>19</sup> colloidal crystals with precise control over the thickness through the particle volume fraction.<sup>19,22</sup>

In this Chapter, we demonstrate the fabrication of binary (composite) colloidal crystals through layer-by-layer controlled drying.

## Experimental Section

Silica particles ( $R = 101, 110, 203, 350$  and  $716$  nm) were prepared using a

microemulsion method.<sup>23</sup> The polystyrene particles ( $R = 97$  nm) were purchased from Duke Scientific. Glass substrates were cleaned with chromic acid prior to use. A clean glass substrate was vertically immersed in a scintillation vial containing colloidal particles dispersed in ethanol, covered with a crystallization dish, crystallization on an anti-vibration table in a room of constant temperature and humidity. The crystal growth rate was on the order of 1 – 2 mm per day. After each deposition of a layer of particles, the sample was dried for 24 hour at room temperature. Scanning electron microscopy (SEM) was carried out on a Philips XL30 FEG microscope. Polystyrene particles were burned away in an oven at 600°C for four hours under air.

## Results and Discussion

First, a 2D hexagonal close-packed (*hcp*) crystal of large ( $L$ ) silica spheres ( $R_L = 203$  nm)<sup>24</sup> was grown on a clean glass substrate. In the next, structure-determining step, the 2D crystal was used as a template on which small ( $S$ ) silica or polystyrene

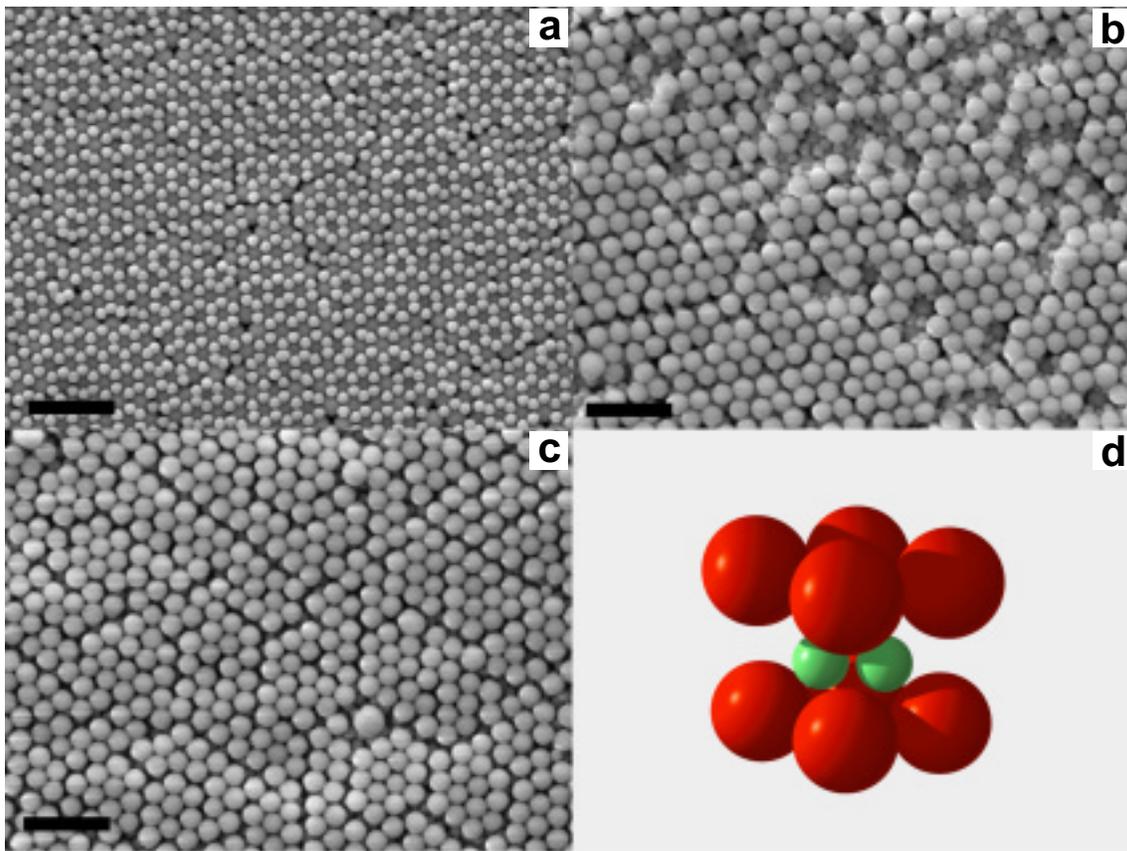


**Figure IV.1-1** Scanning electron micrographs (SEM) showing binary colloidal crystals (size ratio,  $\gamma = 0.54$ ) with a stoichiometry  $LS_2$  (atomic analog  $AlB_2$ ). (a) Open packing with hexagonal symmetry where each small sphere has three neighbors on top of a 2D crystal of large spheres. (b) An incomplete third layer of large particles. (c) Well-ordered complete third layer of large spheres. (d) Schematic presentation of the unit cell of an  $LS_2$  binary crystal. Scale bars, 1  $\mu$ m.

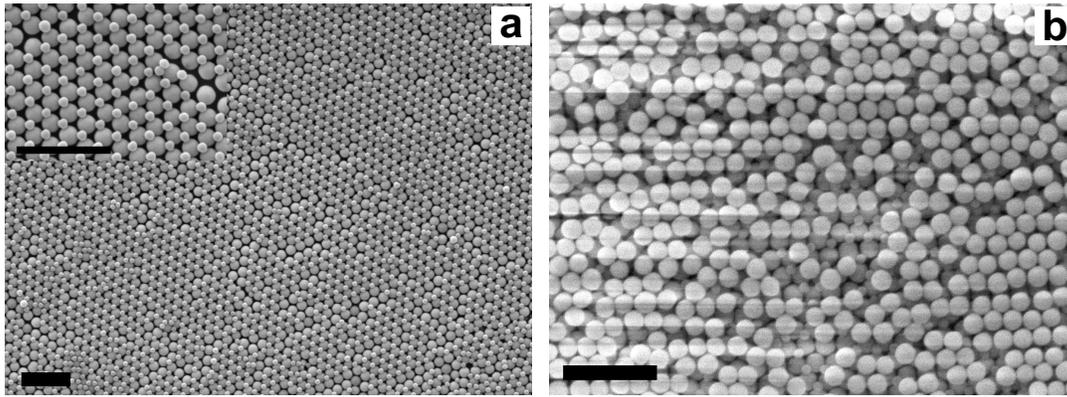


**Figure IV.1-3** Scanning electron micrographs (SEM) showing binary colloidal crystals ( $\gamma = 0.48$ ) with a stoichiometry  $LS$ . (a) Small spheres ordered in an open hexagonal lattice on top of a 2D crystal of large spheres. (b) An incomplete third layer of large particles shows that the large spheres deposit in the interstices not occupied by the small spheres. Scale bars,  $2 \mu\text{m}$ .

particles were deposited. The small particles ( $R_S = 101, 110 \text{ nm}$  silica or  $97 \text{ nm}$  polystyrene) arranged themselves in regular structures depending on their volume fraction,  $\phi$ , and on the size ratio,  $\gamma = R_S / R_L$ . Subsequently, another layer of large particles was deposited. These steps can be successively repeated to grow a 3D structure of the desired thickness and composition. We studied a narrow range of size ratios,  $\gamma = 0.48 - 0.54$ , where we expected  $LS_2$  based on experimental observations in bulk crystallisation<sup>4,5</sup> and on packing arguments.<sup>3</sup>

First, we will present our results for the largest size ratio  $\gamma = 0.54$ . When depositing the second layer of small particles at relatively high volume fraction,  $\phi =$

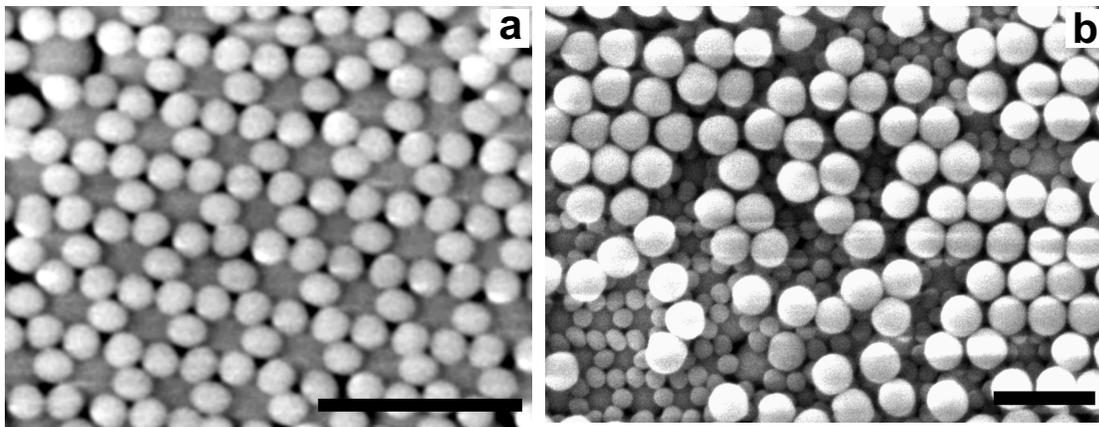


**Figure IV.1-2** Scanning electron micrographs (SEM) showing binary colloidal crystals with stoichiometry  $LS_3$  (no binary atomic analog was found). (a) A magnified region with a *kagomé* net of small spheres on top of a 2D crystal of large spheres ( $\gamma = 0.50$ ). (b) An incomplete third layer of large particles ( $\gamma = 0.48$ ). Scale bars,  $1 \mu\text{m}$ .

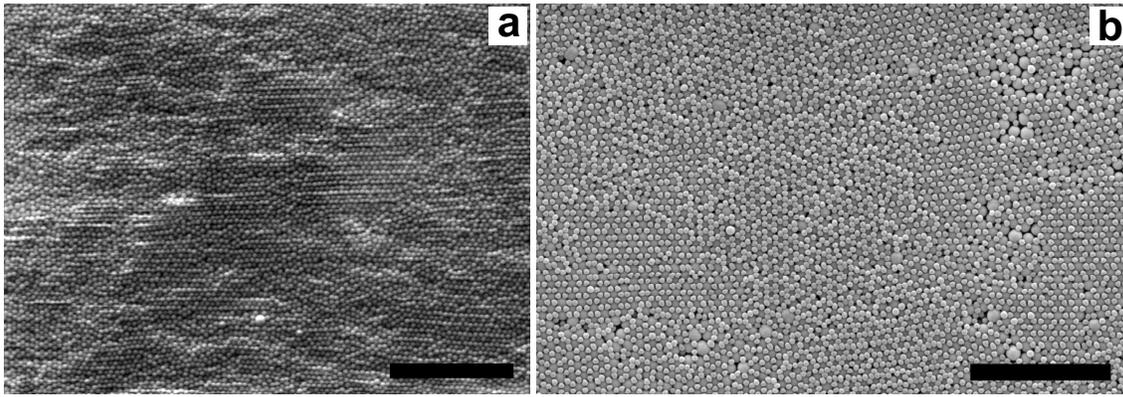


**Figure IV.1-4** Scanning electron micrographs (SEM) showing areas with *kagomé* ( $LS_3$ ) net of small spheres on top of a 2D crystal of large spheres ( $\gamma = 0.48$ ), which co-exist with a ‘complete’ close-packed layer of small spheres (**a**) and an  $LS_2$  net of small spheres (**b**). Scale bars, 5  $\mu\text{m}$ .

0.043 % - sufficient to form a 2D close-packed crystal on a smooth substrate, a slightly corrugated but ‘complete’ close-packed layer of small particles on top of the large ones was observed (not shown). Decrease of the volume fraction to  $\phi = 0.021\%$  led to the formation of large ( $\sim 200 \mu\text{m}^2$ ) areas with a still hexagonal, but more open, packing<sup>25</sup> with three neighbors (Fig. IV.1-1a). Here the small spheres filled in all the hexagonally arranged crevices made by the first layer of larger spheres. The next layer of larger particles deposited themselves exactly on top of the first layer as expected (Fig. IV.1-1b, c), which leads to the formation of the well-known  $LS_2$  binary colloidal crystal (Fig. IV.1-1d). The preserved order of the small spheres can be seen through a patch in the crystal which had an incomplete top layer (Fig. IV.1-1b). Continuation in a layer-by-layer fashion will lead to an  $LS_2$  binary colloidal crystal of desired thickness<sup>26</sup> with exactly the same  $AB_2$  structure (Fig. IV.1-1d) that is observed in bulk colloidal crystallization.<sup>5</sup> Stacking faults in this structure during the layer-by-layer growth are not possible as the optimal positions of small and large particles are uniquely defined in each growth step.

Further decrease of the volume fraction led to the formation of another open structure with hexagonal symmetry. This structure, with stoichiometry  $LS$ , is similar to  $LS_2$ , but instead of six particles there are now three small particles touching each large one. Fig. IV.1-2a shows a large region formed by polystyrene particles ( $\phi = 0.011\%$ ,  $\gamma = 0.48$ ) on a 2D crystal of large silica particles. It is quite surprising that the small particles retain a long-range hexagonal order even when they are not touching. The next layer of larger particles can now stack in two positions: exactly on top of the first layer as for the  $LS_2$  structure ( $AA$  stacking) or into the crevices non-occupied by the small particles formed by the first hexagonal layer ( $AB$  stacking). Our results for  $\gamma = 0.48$  indicated that the next layer always grew as an  $AB$  sequence of the larger spheres; this configuration has a higher packing density (Fig. IV.1-2b),

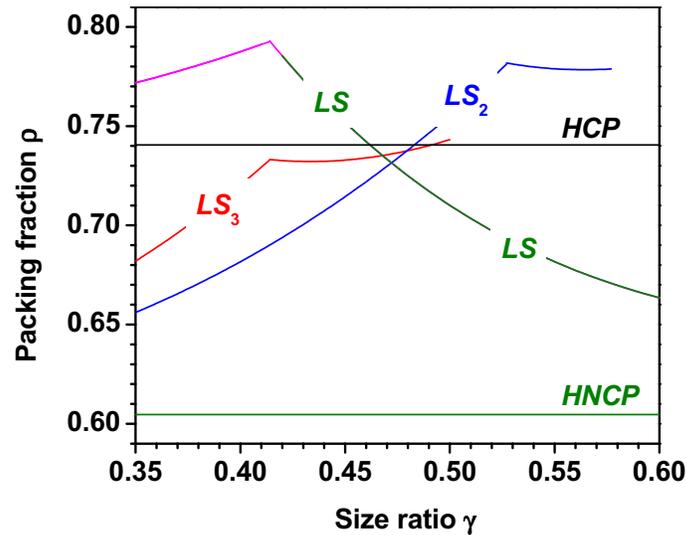


**Figure IV.1-5** Packing fraction diagram as a function of the size ratio  $\gamma$  for the  $LS$  (NaCl type),  $LS_2$  (AlB<sub>2</sub> type), and  $LS_3$  binary colloidal crystals. The calculations are performed only for touching large spheres in the basal plane. The packing limits of hexagonal close-packed (*hcp*) (0.7405) and hexagonal non-close-packed (*hnep*) (0.6046) crystals of one-size spheres are shown by horizontal lines. Note that the new  $LS_3$  structure has a higher packing fraction than  $LS_2$  for  $\gamma < 0.48$ .

although it could be that this preference for  $AB$  stacking of the large spheres is lost for large  $\gamma$ . For the fourth layer, formed from small particles, we did not expect any preferred orientation with respect to the second layer of small particles.

This was indeed what was found and will lead to ambiguity in the stacking of the resulting 3D structure. Therefore, only randomly stacked analogs of NaCl or NiAs can be grown by our layer-by-layer method. Although binary colloidal crystals of NaCl type have been predicted to be a stable phase in bulk crystallization,<sup>27</sup> only

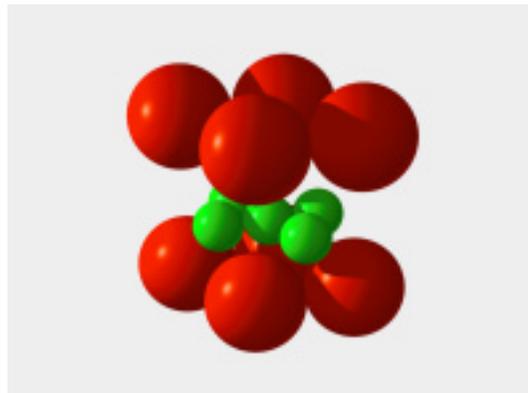


**Figure IV.1-6** Schematic presentation of the unit cell of an  $LS_3$  binary crystal.

very recently small crystallites of binary crystal of stoichiometry  $LS$  were observed for the first time.<sup>28</sup> It was not clear for this structure whether it was a pure NaCl structure or whether it was a random-stacked crystal.

For size ratios,  $\gamma = 0.48 - 0.5$ , a completely different arrangement of the small spheres, in addition to the already described  $LS$  and  $LS_2$  structures, was observed. Again, at a relatively high volume fraction ( $\phi = 0.041\%$ ,  $\gamma = 0.48$ ) of the small particles, a ‘complete’ coverage on the top of the big particles was found. At lower volume fraction ( $\phi = 0.021\%$ ) a *kagomé* arrangement of the small spheres on top of the 2D crystal of large spheres was observed: in this case each small sphere had four neighbors<sup>25</sup> (Fig. IV.1–3a). Similarly to the  $LS_2$  binary crystal, each large sphere was surrounded in a ring by six small spheres, but now the rings were rotated in such a way that the crevices formed in between the large spheres were filled with three small spheres arranged in a (planar) triangle (Fig. IV.1–3a). Mostly, this open structure was found to co-exist with the  $LS_2$  structure observed earlier or with a complete layer of small particles (Fig. IV.1–4) The *kagomé* lattice in antiferromagnetics is probably the best-known geometrically frustrated lattice, which cannot order because of the

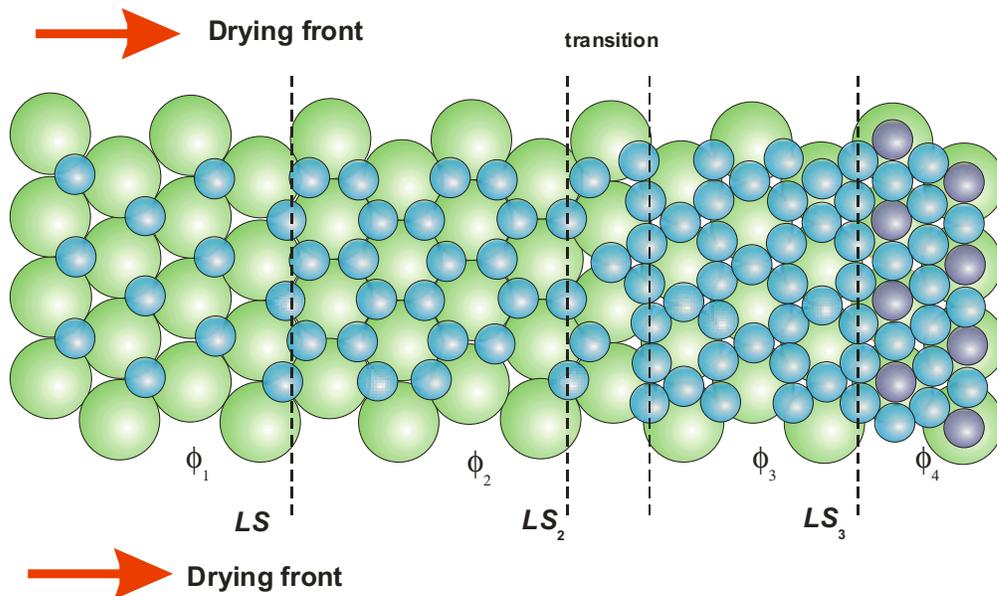


**Figure IV.1–7** Schematic representation of the structures of small spheres with size ratio close to 0.5 that form onto a 2D hexagonal layer of larger spheres as function of the volume fraction. The symmetry of the structures can be understood as resulting from the templating effect of the first layer, and the forces resulting from the particle-liquid interfacial tension. Particles are lined up parallel to the drying front and go into those places that lie lowest on the 2D crystalline layer of the larger particles. The volume fraction,  $\phi$ , determines finally how many of the available low-lying sites can be occupied.

high degeneracy of its ground state and ensuing large fluctuations (see Ref. 29, and references therein). Deposition of a second layer of big particles led to the formation of an  $LS_3$  binary colloidal crystal (Fig. IV.1–3b). Just as with the  $LS_2$  crystal, degeneracy in stacking is not possible as the position of every next layer is unambiguously defined. A schematic presentation of the unit cell of the  $LS_3$  is shown in Fig. IV.1–5.

To our knowledge  $LS_3$  does not have a reported isostructural binary atomic analog. It is interesting to note that this structure has a higher packing fraction than  $LS_2$  for  $\gamma < 0.48$  (Fig. IV.1–6) and should therefore be the thermodynamically stable phase at high pressure. However, as far as we know it has not been studied theoretically or ever suggested before as a possible binary colloidal crystal. There are few systems where a *kagomé* net is realized. Therefore, a composite  $LS_3$  crystal of small magnetic and larger antimagnetic particles will be of interest as a frustrated antiferromagnet model system.

The complex self-organization of the small particles in the second layer is the result of the interplay of geometrical packing arguments, minimization of the surface free energy of the drying liquid film, and surface forces due to the curved menisci. During the drying of the wetting film, particles partially immersed experience both the attractive capillary forces that tend to draw particles together<sup>21</sup> and the corrugated surface of the first layer of large particles. As the drying rate is constant, which (open) packing will be realized is determined by the local particle concentration and the symmetry and orientation of the already deposited layers. A schematic representation of the process is given in Fig. IV.1–7. Here we have used that a lot can be inferred about the mechanism from the orientation of the 2D crystalline layers with respect to the drying front, from the orientation of the

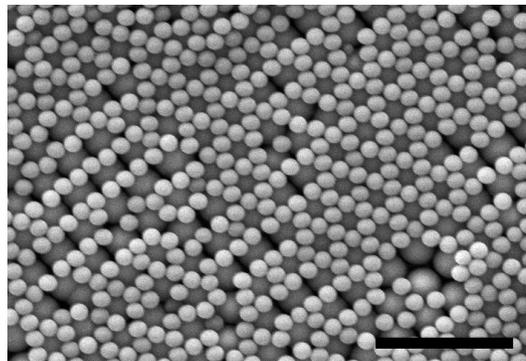


**Figure IV.1–8** Scanning electron micrographs (SEM) showing areas with line-like defects in the *kagomé* ( $LS_3$ ) net of small spheres on top of a 2D crystal of large spheres ( $R_L = 716$  nm,  $\gamma = 0.49$ ). Scale bar, 5  $\mu$ m.

subsequent layer deposited on the first layer and from the defects observed in some of the samples. Both the 2D hexagonal crystals and the 3D crystals of single size spheres, which are not studied here, when grown on a vertical substrate by controlled drying are almost exclusively deposited with rows of touching particles parallel to the drying front. Given that this must be how the particles are arranged at the interface of the drying liquid, this observation can be understood.

At sufficiently high volume fraction the second layer of smaller particles also forms a 2D hexagonal layer with lines of touching particles parallel with the drying front (see Fig. IV.1–7,  $\phi_4$ ). Despite the fact that this layer cannot be flat, e.g., the darker particles in the figure are elevated because they are exactly on top of the particles in the first layer, the size ratio close to 0.5 makes it geometrically possible for the second layer to become hexagonal as well. At slightly lower volume fraction,  $\phi_3$ , complete coverage by the second layer is not possible, so that the dark particles (see Fig. IV.1–7), which are sticking out of the drying film the most, are lost first. This leads to the *kagomé* net observed for the second layer in Fig. IV.1–3a. At yet lower volume fraction,  $\phi_2$ , the structures formed are again explained by taking fewer particles in the drying front and placing them at the lowest points that become available. These are formed by the hexagonal crevices formed by the hexagonally arranged first layer. This structure has the  $LS_2$  arrangement from Fig. IV.1–1a. Because the change in volume fraction from  $\phi_3$  to  $\phi_2$  is quite subtle, the  $LS_3$  structures are mostly seen in combination with the  $LS_2$  (Fig. IV.1–4a) and defects (Fig. IV.1–8) given in the transition region denoted in Fig. IV.1–4. At  $\phi_1$  there are even less particles in the drying front and now filling up lowest points in a line parallel to the drying film results in the  $LS$  structure from Fig. IV.1–2a. Our observations also

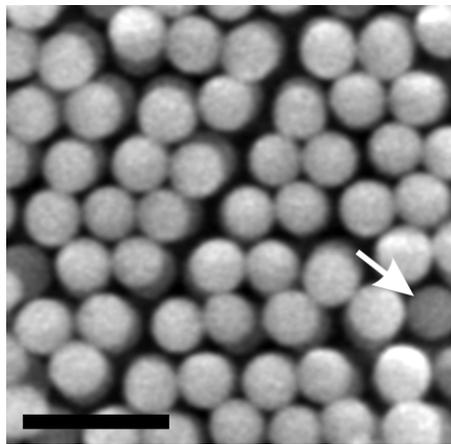


**Figure IV.1–9** Scanning electron micrograph (SEM) of the top layer of a hexagonal non-close-packed (*hncp*) colloidal crystal. The arrow points to a particle from the bottom layer. Scale bar, 1  $\mu\text{m}$ .

explain the observation made in Ref. 30 where it was observed that in holes in a polymer film in which three particles fitted the drying front arranged the triangles with sides parallel to the drying front.

In order to show how our method can be used to create non-close-packed crystals of single-sized particles, we first created a composite  $LS_2$  binary crystal of alternating layers of inorganic (silica) and organic (polystyrene) particles. Then, the organic layer was removed by heating in an oven in air. The resulting structure is a hexagonal non-close-packed (*hnep*) crystal (Fig. IV.1–9), which, to our knowledge has not been made before with colloids. This non-close-packed structure with a low packing fraction of  $\rho = 0.6046$  (Fig. IV.1–6) compared to close-packed (0.7405) is another example of how the layer-by-layer method can be used to create new crystal structures that cannot be grown in bulk.

## Conclusions

We have demonstrated the formation of large areas of  $LS$  and  $LS_2$ , and, a new,  $LS_3$  binary colloidal crystals using a non-equilibrium layer-by-layer growth process. In the work presented here, we explored only a small region of size ratios and already found new structures. Clearly, other size ratios should be explored and the method can be expanded further by including more sizes and particles of different composition to produce more complicated superstructures. The method is simple enough that it can be easily automated to create thicker structures than shown here.<sup>31</sup> Using surface templates,<sup>16</sup> the method can be further extended by growing different crystal planes and new types of crystals with a well-defined crystal orientation.<sup>32</sup> For instance, using a square template will provide the possibility to grow CsCl type binary structures. Our method will substantially expand the stoichiometries, compositions, and symmetries achievable with crystals of colloidal particles.

## Acknowledgements

We thank Paul M. Chaikin (Princeton University), Marileen Dogterom (FOM AMOLF), and Arnout Imhof (Utrecht University) for helpful discussions.

---

## References and Notes

- (1) Kiely, C. J.; Fink, J.; Brust, M.; Bethell, D.; Schiffrin, D. J. *Nature* **1998**, *396*, 444.
- (2) Murray, M. J.; Sanders, J. V. *Nature* **1978**, *275*, 201.
- (3) Murray, M. J.; Sanders, J. V. *Phil. Mag.* **1980**, *43*, 721.
- (4) Hachisu, S.; Yoshimura, S. *Nature* **1980**, *283*, 188.
- (5) Bartlett, P.; Ottewill, R. H.; Pusey, P. N. *Phys. Rev. Lett.* **1992**, *68*, 3801.

- (6) Eldridge, M. D.; Madden, P. A.; Frenkel, D. *Nature* **1993**, *365*, 35.
- (7) Joannopoulos, J. D.; Villeneuve, P. R.; Fan, S. H. *Nature* **1997**, *386*, 143.
- (8) Pan, G. S.; Kesavamoorthy, R.; Asher, S. A. *Phys. Rev. Lett.* **1997**, *78*, 3860.
- (9) Holtz, J. H.; Holtz, J. S. W.; Munro, C. H.; Asher, S. A. *Anal. Chem.* **1998**, *70*, 780.
- (10) Hultheen, J. C.; Treichel, D. A.; Smith, M. T.; Duval, M. L.; Jensen, T. R.; Van Duyne, R. P. *J. Phys. Chem. B* **1999**, *103*, 3854.
- (11) Tessier, P. M.; Velev, O. D.; Kalambur, A. T.; Rabolt, J. F.; Lenhoff, A. M.; Kaler, E. W. *J. Am. Chem. Soc.* **2000**, *122*, 9554.
- (12) Holland, B. T.; Blanford, C. F.; Do, T.; Stein, A. *Chem. Mat.* **1999**, *11*, 795.
- (13) Velev, O. D.; Lenhoff, A. M. *Curr. Opin. Colloid Interface Sci.* **2000**, *5*, 56.
- (14) Yang, P. D.; Rizvi, A. H.; Messer, B.; Chmelka, B. F.; Whitesides, G. M.; Stucky, G. D. *Adv. Mater.* **2001**, *13*, 427.
- (15) Jiang, P.; Bertone, J. F.; Colvin, V. L. *Science* **2001**, *291*, 453.
- (16) van Blaaderen, A.; Ruel, R.; Wiltzius, P. *Nature* **1997**, *385*, 321.
- (17) Heni, M.; Lowen, H. *Phys. Rev. Lett.* **2000**, *85*, 3668.
- (18) Denkov, N. D.; Velev, O. D.; Kralchevsky, P. A.; Ivanov, I. B.; Yoshimura, H.; Nagayama, K. *Nature* **1993**, *361*, 26.
- (19) Jiang, P.; Bertone, J. F.; Hwang, K. S.; Colvin, V. L. *Chem. Mater.* **1999**, *11*, 2132.
- (20) Kralchevsky, P. A.; Denkov, N. D. *Curr. Opin. Colloid Interface Sci.* **2001**, *6*, 383.
- (21) Denkov, N. D.; Velev, O. D.; Kralchevsky, P. A.; Ivanov, I. B.; Yoshimura, H.; Nagayama, K. *Langmuir* **1992**, *8*, 3183.
- (22) Dimitrov, A. S.; Nagayama, K. *Langmuir* **1996**, *12*, 1303.
- (23) Osseoasare, K.; Arriagada, F. J. *Colloid Surf.* **1990**, *50*, 321.
- (24) Highly monodispersed silica particles were prepared using a microemulsion method (See K. Osseoasare, F. J. Arriagada, *Colloid and Surf.* **1990**, *50*, 321) followed by seeded growth.
- (25) Smith, J. V. *Geometrical and Structural Crystallography*; Wiley: New York, 1982.
- (26) It is important to note for the present paper that interesting photonic effects can already be achieved with only 1.5 unit cells of a photonic crystal. Lin, S. Y. et al. A 3-Dimensional photonic crystal operating at infrared wavelengths, *Nature* **1998**, *394*, 251.
- (27) Denton, A. R.; Ashcroft, N. W. *Phys. Rev. A* **1990**, *42*, 7312.
- (28) Hunt, N.; Jardine, R.; Bartlett, P. *Phys. Rev. E* **2000**, *62*, 900.
- (29) Moessner, R.; Sondhi, S. L. *Phys. Rev. B* **2001**, *6322*, 224401.
- (30) Yin, Y. D.; Xia, Y. N. *Adv. Mater.* **2001**, *13*, 267.
- (31) As the basis of the controlled drying technique is similar to industrial coating processes, where good control over thickness of the depositing layers and high automatization are achieved, we believe that scaling up of the process to an industrial scale is feasible.
- (32) van Blaaderen, A.; Wiltzius, P. *Adv. Mater.* **1997**, *9*, 833.



---

## IV.2 Photonic Crystals of Shape-Anisotropic Colloidal Particles

Spherical silica ( $\text{SiO}_2$ ), zinc sulfide ( $\text{ZnS}$ ), and core-shell particles of these materials undergo a substantial anisotropic plastic deformation under high-energy ion irradiation. Individual particles can be turned into oblate or prolate ellipsoids with exact control over the aspect ratio. Here we report on the fabrication and optical characterization of thin three-dimensional (3D) photonic crystals of spherical particles, which have been anisotropically deformed into spheroidal oblates by means of ion irradiation. As a result of the collective deformation process, both the unit cell symmetry and the particle form factor have been changed leading to appreciable tunability in the optical properties of the photonic crystal.

## Introduction

Since their discovery, photonic crystals (materials with a periodically modulated dielectric constant) have received considerable attention because of their unique ability to control the propagation and spontaneous emission of light.<sup>1-3</sup> For photonic crystals (PC) with a high enough contrast in combination with a certain symmetry, the propagation of electromagnetic waves can be inhibited for a certain frequency range leading to the formation of a photonic band gap (PBG). PCs are expected to have many applications such as filters, optical switches, and low-threshold lasers.<sup>4</sup> The fabrication of PCs with a submicron periodicity, however, is difficult and requires state-of-the-art microlithography techniques. With their ability to self-organize into three-dimensional (3D) structures with different symmetries colloidal spheres offer an alternative way for the fabrication of PCs at optical wavelengths.<sup>5,6</sup>

It is well known that face-centered cubic (*fcc*) PCs made of dielectric spheres do not possess a 3D PBG,<sup>7-9</sup> because of a symmetry-induced degeneracy of the polarization modes at the W-point of the Brillouine zone. This degeneracy can be broken by using shape-anisotropic<sup>10</sup> or dielectrically-anisotropic<sup>11</sup> objects as building blocks. Here also, non-spherical colloidal particles offer excellent possibilities as building blocks to create PCs. However, there are additional difficulties to overcome in comparison to the conventional spherical particles.<sup>12</sup> Firstly, there are not many methods to synthesize non-spherical colloids with well-defined size and shapes.<sup>13</sup> Secondly, most of these particles (e.g., metal oxides) strongly absorb light in the visible region. Finally, the most commonly used methods for assembling, such as controlled drying<sup>14</sup> and sedimentation,<sup>15</sup> might not be suitable in the case of non-spherical particles or will provide less control over the final structure.

Recently, it was demonstrated that inorganic, amorphous and polycrystalline, spherical colloidal particles can be turned into ellipsoids by high-energy ion irradiation.<sup>16,17</sup> The method allows continuous variation of the particle shape from oblate to prolate ellipsoids with precise control over the aspect ratio. PCs built from ellipsoidal particles can be used as templates to make inverse opals (See references cited in Refs. 5,6 to a recent approach in which inverse opals are used to make colloidal crystals of shape-anisotropic particles).<sup>18</sup> Because of the shape-anisotropy there will be strong polarization effects leading to birefringence at long wavelengths.<sup>10</sup> The ability to change the shape of the unit cell and its contents will allow control over polarization modes in a PC.<sup>19</sup>

In this Chapter, we demonstrate the fabrication of photonic crystals of (almost) ellipsoidal colloidal particles obtained after ion irradiation of colloidal crystals of spherical SiO<sub>2</sub> and ZnS-core-SiO<sub>2</sub>-shell (see Chapter II.1)<sup>20</sup> particles. We performed angle-resolved optical transmission measurements on thin photonic

crystals. We show that as a result of the irradiation, both the shape of the individual particles and the lattice spacing in the original *fcc* (111) direction were changed leading to a substantial shift in the position of the stop gap.

## Experimental Section

Colloidal photonic crystals were fabricated from monodisperse  $\text{SiO}_2$  and ZnS-core- $\text{SiO}_2$ -shell<sup>20,21</sup> spheres. Silica particles with a radius of 110 nm (relative width in the size distribution,  $\delta = 3\%$ ) were synthesized using a microemulsion method followed by seeded growth.<sup>22</sup> ZnS-core- $\text{SiO}_2$ -shell particles with a total radius of 128 nm ( $\delta = 5\%$ ) with a ZnS- $\text{SiO}_2$  composite core radius of 84 nm ( $\delta = 6\%$ ) were prepared as described in Chapter II.1.<sup>20</sup> Thin colloidal crystals of 8–10 layers thick were grown on clean glass substrates using a controlled drying method.<sup>14,20,23</sup> With this method, the *fcc* crystals are uniquely oriented with the lines of touching particles forming the (111) plane parallel to the drying front (see Chapter IV.1).<sup>24</sup> Silica crystals were annealed at 600°C for four hours in air.<sup>25</sup> Colloidal crystals were irradiated with 4 MeV  $\text{Xe}^{4+}$  ions at 90 K with the sample surface held at an angle of 45° with respect to the direction of the ion beam. The ion fluence was  $4.0 \times 10^{14}$  and  $1.0 \times 10^{15} \text{ cm}^{-2}$  for ZnS-core- $\text{SiO}_2$ -shell and  $\text{SiO}_2$ , respectively. Samples were coated with a 5 nm Pt/Pd layer before analyzing by scanning electron microscopy (SEM) at 5 kV. The angle-resolved optical transmission spectra were measured with a Cary 500 UV-near-IR spectrometer. The light beam spot diameter was about 5 mm<sup>2</sup>, which is comparable to the area of single-crystalline domains for a crystal before annealing or irradiation.

## Results and Discussion

Figure IV.2–1 shows SEM micrographs of a thin planar crystal of close-packed monodisperse silica colloidal particles. After the irradiation all particles were deformed and turned into (almost) oblate ellipsoids.<sup>16</sup> The particles expanded relatively undisturbed in the plane perpendicular to the plane of irradiation. A deformation in other directions, e.g., along the (111) direction, will lead to a more complex collective deformation. The collective deformation process preserved the 3D order of the crystal. However, stresses induced by the deformation and perhaps a small amount of additional shrinkage caused the formation of additional cracks parallel to the direction of irradiation. The cracks are typically observed every 2  $\mu\text{m}$ . All ellipsoids formed are oriented with longitudinal axes in a plane parallel to the plane of ion irradiation, i.e. 45° with respect to the glass substrate. When the sample is imaged at -45° (Fig. IV.2–1b) both semi-axes ( $x$ ,  $y$ ) can be measured directly. The ellipsoidal semi-axes  $x = 123 \pm 5 \text{ nm}$  and  $y = 74 \pm 2 \text{ nm}$  (aspect ratio  $1.65 \pm 0.09$ ) were determined by image processing of the SEM micrographs. From the side view (Fig. IV.2–1c), one can see that the anisotropic deformation is extended throughout

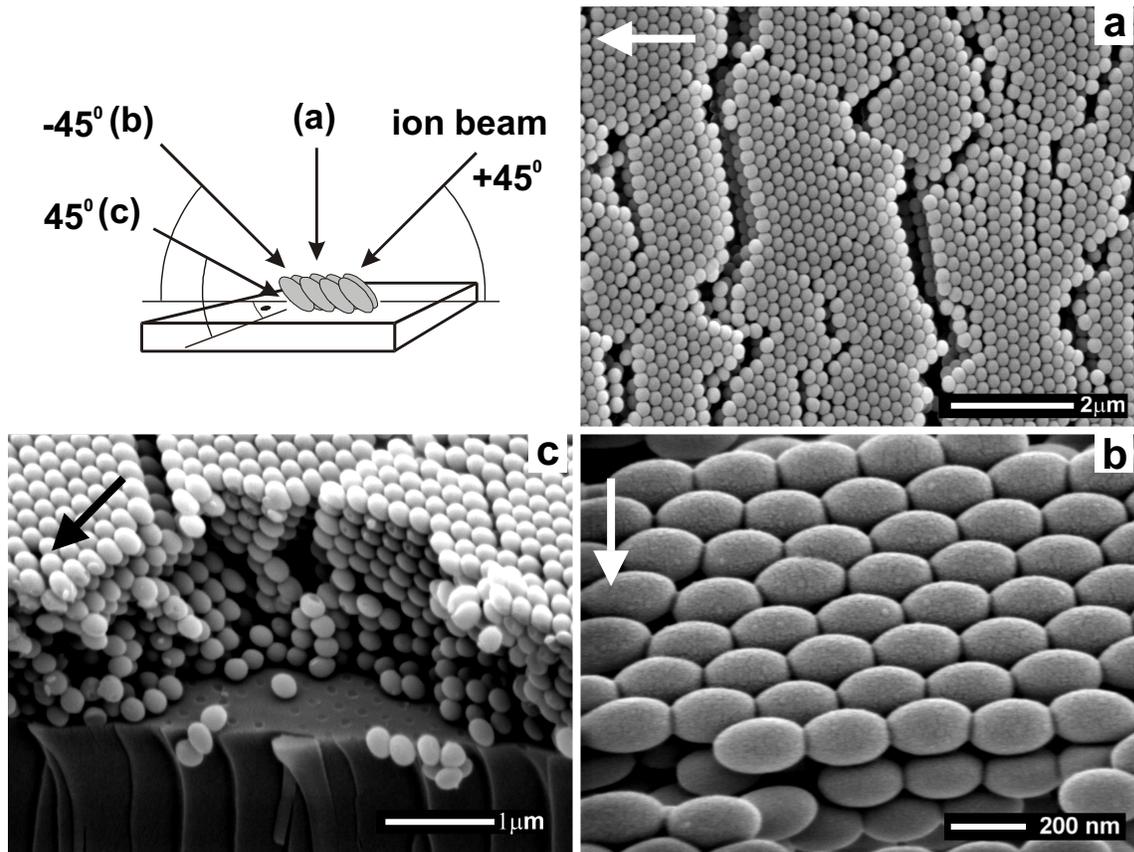


**Figure IV.2-1** Scanning electron microscopy (SEM) images of a planar photonic crystal of close-packed  $\text{SiO}_2$  oblate ellipsoids obtained after irradiation with 4 MeV  $\text{Xe}^{4+}$  ions to a fluence of  $1.0 \times 10^{15} \text{ cm}^{-2}$  at angle of  $45^\circ$  at 90K. (a) Top view of the crystal showing the (111)-crystal plane. (b) Top view at  $-45^\circ$  (perpendicular to the plane of irradiation) of the crystal. The average semi-axes of the ellipsoids determined from the SEM picture are  $x = 123 \pm 5 \text{ nm}$  and  $y = 74 \pm 2 \text{ nm}$ . (c) Side view of a broken crystal showing the depth of the deformation caused by the irradiation. The big arrows show the direction of the ion beam.

the full crystal including to the first layer of particles in contact with the substrate. However, as the crystal thickness ( $\sim 1.8 \mu\text{m}$ ) is close to the calculated penetration depth of the 4 MeV  $\text{Xe}^{4+}$  ions, taking the angle of irradiation and the filling fraction of  $\text{SiO}_2$  into account, it might be that the particles close to the substrate are slightly less deformed. From Fig. IV.2-1c, it is apparent that there is a slight deviation from the ellipsoidal shape caused by the fact that deforming spheres were touching each other in the crystal. Most likely, this increases the packing fraction and consequently the effective refractive index of the composite.

Figure IV.2-2 shows optical transmission spectra of thin photonic crystals of  $\text{SiO}_2$  (a) and ZnS-core- $\text{SiO}_2$ -shell (b) colloidal particles taken along the (111) direction (crystallographic directions mentioned hereafter are with respect to the undeformed

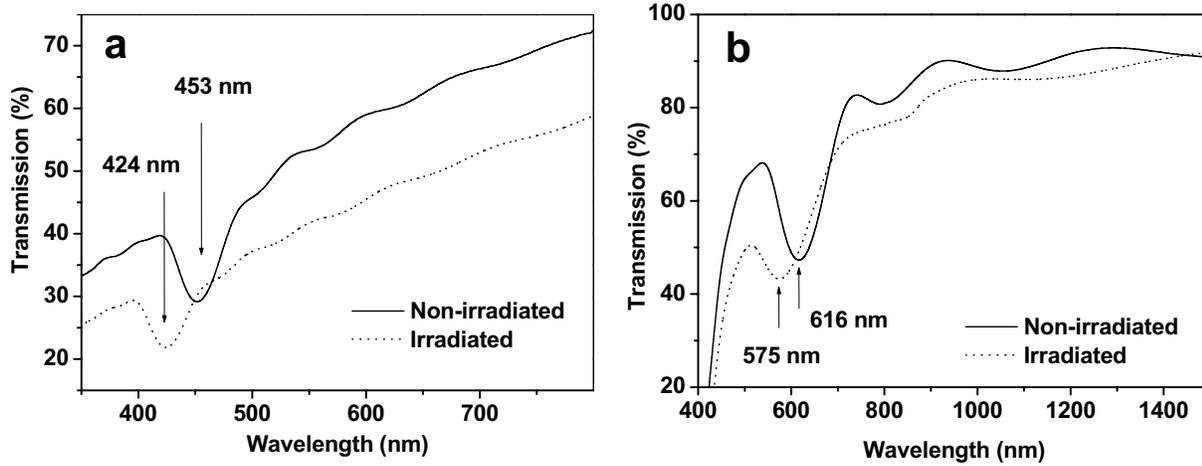


**Figure IV.2-2** Optical transmission spectra taken along the (111) crystallographic axis measured on thin colloidal photonic crystals of (a) ZnS-core-SiO<sub>2</sub>-shell and (b) SiO<sub>2</sub> colloidal particles grown on glass substrates. The position of the minimum in the optical transmission spectra of the irradiated samples (dotted line) is shifted to shorter wavelengths in comparison to the non-irradiated samples (solid line). The crystals consist of ten layers of close-packed silica particles (b) and eight layers of core-shell particles (a), respectively. In both cases a shift of > 20 nm in the position of the stop gap is observed.

*fcc* crystal). The spectra before and after the ion irradiation exhibit a minimum in the optical transmission, where the Bragg condition is fulfilled and light is diffracted away from the axis of propagation. The presence of a Bragg peak after irradiation indicates that the crystal structure remains after the ion irradiation. However, the minimum, which corresponds to the stop gap, has shifted to shorter wavelengths both in Fig. IV.2-2a and Fig. IV.2-2b. This shift is an effect of the changed lattice spacing in the crystal and possibly a small densification of the whole crystal. Figure IV.2-3 shows optical transmission spectra measured at different angles on non-irradiated and irradiated samples. The transmission was measured from different points on the L → W line towards the  $\Gamma$  of the Brillouin zone. In both cases, the stop gap gradually disappears at large angles of incidence.

In order to determine the correct position of the stop gap from the experimental spectra, we subtracted the background scattering.<sup>20,26</sup> The positions of the stop gaps for irradiated and non-irradiated crystals as a function of  $\sin^2(\theta)$  are shown in Fig. IV.2-4. In the case of spherical particles, the position of the stop gap can to first approximation be related to the particle diameter,  $2R$ , and the effective dielectric constant of the medium through the modified Bragg law,  $\lambda_{\max} = 2d_{111}\sqrt{\epsilon_{\text{eff}} - \epsilon_b \sin^2 \theta}$ , where  $d_{111} = 2R\sqrt{2/3}$  is the distance between the crystal planes in the (111) direction,  $\epsilon_{\text{eff}}$  is the volume averaged dielectric constant of the

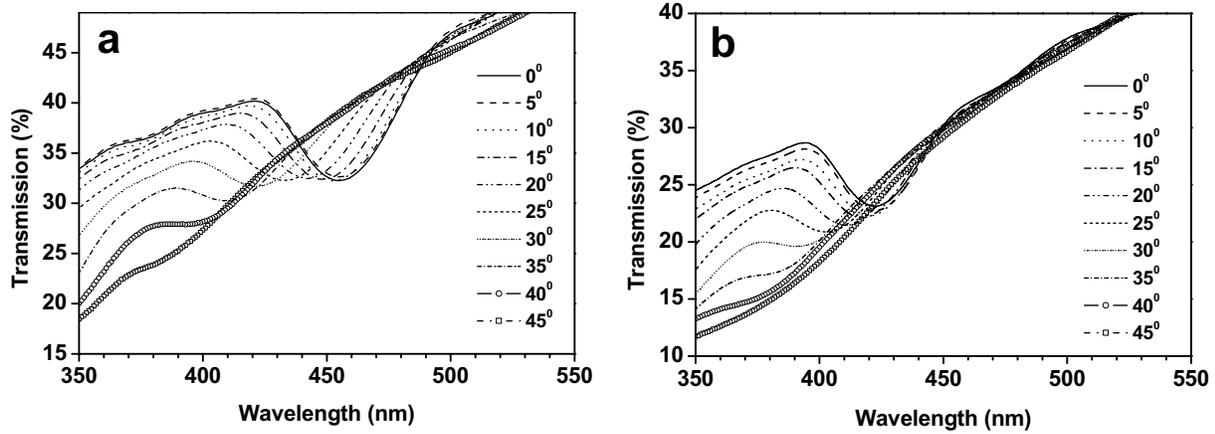


**Figure IV.2-3** Angle-resolved optical transmission spectra of colloidal photonic crystals of silica particles grown on a glass substrate. The spectra were taken from different points on the  $L \rightarrow W$  line towards the  $\Gamma$  point of the Brillouin zone. (a) Non-irradiated crystal of spherical particles. (b) Irradiated crystal of oblate ellipsoidal particles of aspect ratio  $1.65 \pm 0.09$ .

composite:  $\varepsilon_{eff} = f\varepsilon_p + (1-f)\varepsilon_b$ , where  $f$  is the crystal filling fraction ( $f = 0.74$  for closely-packed spheres),  $\varepsilon_p$  and  $\varepsilon_b$  are the dielectric constants of the particle, and the background, respectively. From the fit with a silica refractive index of 1.47, we determined a particle radius of 103 nm ( $d_{111} = 168$  nm). This value corresponds to a  $\sim 6\%$  shrinkage of the silica particles after thermal annealing and is similar as observed before.<sup>25</sup> The calculated volume of the spheres before the irradiation agrees well with the volume of an ellipsoid ( $4/3\pi x^2 y$ ) calculated using the values of the two semi-axes determined from the SEM images. The volume of a single silica particle was previously found not to change significantly after ion irradiation.<sup>16</sup>

After the ion irradiation the lattice spacing in the (111) direction decreased. As a result, the position of the Bragg peak shifted accordingly to shorter wavelengths. Because of the deformation, the crystal unit cell is now tetragonal rather than cubic. It can be shown that the lattice spacing in the (111) direction after isotropic deformation under certain angle,  $\alpha$ , can be written as  $d_{111} = 2y\sqrt{2/3}\left[1 - \left(1 - y^2/x^2\right)\cos^2\alpha\right]^{-1/2}$ , where  $x$  and  $y$  are the lengths of the two semi-axes of the ellipsoid ( $x > y$ ). Using this equation we find  $d_{111} = 147$  which is close to the value of  $d_{111} = 153$  nm determined from the fit in Fig. IV.2-4. This analysis assumes that the particles deform into ellipsoids and there is no change in the volume of the particles. From the fit in Fig. IV.2-4, we also determined an effective refractive index of the composite of 1.40, which corresponds to a  $\sim 2.6\%$  increase in comparison to the non-irradiated sample. This indicates that some densification of the crystal has

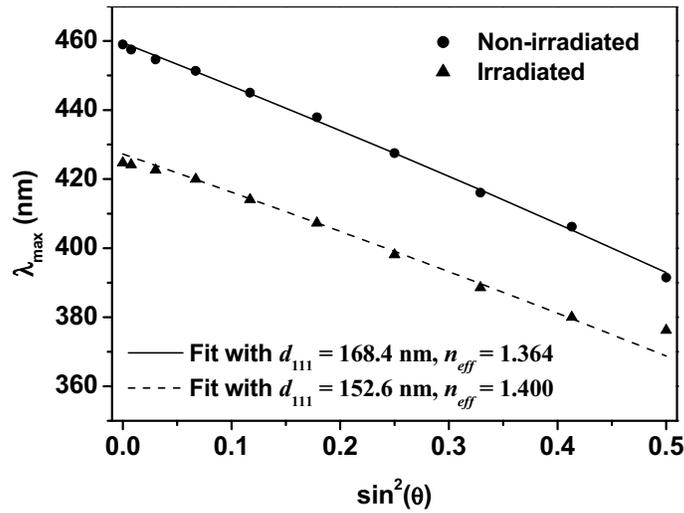


**Figure IV.2-4** Position of the transmission minima in Fig. IV.2-3 as a function of  $\sin^2(\theta)$ . After irradiation, the positions of the stop gap for ellipsoidal particles (triangles) shift to shorter wavelengths in comparison to the case of spherical particles (spheres). The values are determined from the experimental spectra after correction for the background scattering. The lines are theoretical fits using  $\lambda_{\max} = 2d_{111}\sqrt{\varepsilon_{\text{eff}} - \sin^2 \theta}$ .

taken place after the irradiation assuming that the dielectric constant of silica did not change.

## Conclusions

In conclusion, we demonstrated the fabrication of colloidal photonic crystals of shape-anisotropic particles from crystals made of spheres using MeV ion irradiation. In this way, both the lattice structure and the form factor were changed in a controlled way. The aspect ratio of the shape-anisotropic particles can be used as an additional parameter to engineer the photonic band gap.

## Acknowledgements

The authors thank Dimitrii Mazurenko, Christina Christova, and Arnout Imhof (Utrecht University) for helpful discussions.

---

## References

- (1) Bykov, V. P. *Sov. J. Quantum Electron.* **1975**, *4*, 861.
- (2) Yablonovitch, E. *Phys. Rev. Lett.* **1987**, *58*, 2059.
- (3) John, S. *Phys. Rev. Lett.* **1987**, *58*, 2486.
- (4) Soukoulis, C. M. *Photonic crystals and light localization in the 21th century*; Kluwer Academic

Publishers: Dordrecht, 2001; Vol. C 563.

- (5) van Blaaderen, A. *MRS Bull.* **1998**, *23*, 39.
- (6) Colvin, V. L. *MRS Bull.* **2001**, *26*, 637.
- (7) Leung, K. M.; Liu, Y. F. *Phys. Rev. Lett.* **1990**, *65*, 2646.
- (8) Sozuer, H. S.; Haus, J. W.; Inguva, R. *Phys. Rev. B-Condens Matter* **1992**, *45*, 13962.
- (9) Haus, J. W. *J. Mod. Opt.* **1994**, *41*, 195.
- (10) Haus, J. W.; Sozuer, H. S.; Inguva, R. *J. Mod. Opt.* **1992**, *39*, 1991.
- (11) Li, Z. Y.; Wang, J.; Gu, B. Y. *Phys. Rev. B-Condens Matter* **1998**, *58*, 3721.
- (12) Lu, Y.; Yin, Y. D.; Xia, Y. N. *Adv. Mater.* **2001**, *13*, 415.
- (13) Matijevic, E. *Chem. Mat.* **1993**, *5*, 412.
- (14) Jiang, P.; Bertone, J. F.; Hwang, K. S.; Colvin, V. L. *Chem. Mater.* **1999**, *11*, 2132.
- (15) Mayoral, R.; Requena, J.; Moya, J. S.; Lopez, C.; Cintas, A.; Miguez, H.; Meseguer, F.; Vazquez, L.; Holgado, M.; Blanco, A. *Adv. Mater.* **1997**, *9*, 257.
- (16) Snoeks, E.; van Blaaderen, A.; van Dillen, T.; van Kats, C. M.; Brongersma, M. L.; Polman, A. *Adv. Mater.* **2000**, *12*, 1511.
- (17) van Dillen, T.; Polman, A.; Fukarek, W.; van Blaaderen, A. *Appl. Phys. Lett.* **2001**, *78*, 910.
- (18) Velev, O. D.; Kaler, E. W. *Adv. Mater.* **2000**, *12*, 531.
- (19) Noda, S.; Yokoyama, M.; Imada, M.; Chutinan, A.; Mochizuki, M. *Science* **2001**, *293*, 1123.
- (20) Velikov, K. P.; Moroz, A.; van Blaaderen, A. *Appl. Phys. Lett.* **2002**, *80*, 49.
- (21) Velikov, K. P.; van Blaaderen, A. *Langmuir* **2001**, *17*, 4779.
- (22) Osseasare, K.; Arriagada, F. J. *Colloid Surf.* **1990**, *50*, 321.
- (23) Denkov, N. D.; Velev, O. D.; Kralchevsky, P. A.; Ivanov, I. B.; Yoshimura, H.; Nagayama, K. *Langmuir* **1992**, *8*, 3183.
- (24) Velikov, K. P.; Christova, C. G.; Dullens, R. P. A.; van Blaaderen, A. *submitted* **2001**.
- (25) Miguez, H.; Meseguer, F.; Lopez, C.; Blanco, A.; Moya, J. S.; Requena, J.; Mifsud, A.; Fornes, V. *Adv. Mater.* **1998**, *10*, 480.
- (26) Bertone, J. F.; Jiang, P.; Hwang, K. S.; Mittleman, D. M.; Colvin, V. L. *Phys. Rev. Lett.* **1999**, *83*, 300.

---

# Summary

A photonic crystal (PC) is a material with a periodically modulated dielectric constant. In analogy to electrons in a semiconductor, light propagation in a PC can be inhibited for a certain frequency range resulting in the formation of photonic (stop) band gaps (PBGs). If the stop gaps are wide enough to overlap for both polarization states along all crystal directions, a complete photonic band gap (CPBG) is formed. By use of PCs, it is possible to manipulate both the propagation and the spontaneous emission of light. It is believed that PCs, acting as semiconductors for light, could lead to a revolution in the information and the telecommunication industry by enabling higher-capacity optical fibers, nanoscopic lasers, and photonic integrated circuits to replace today's microchips. Because of difficulties in the fabrication of PCs with sub-micron features, a CPBG in the visible has not been realized yet.

This thesis focuses on issues concerning the design and the fabrication of PCs that might possess a CPBG in the visible, and, the engineering the properties of the PBG using new types of building blocks. By use of core-shell and non-spherical colloidal particles, we demonstrate the ability to modify the properties of the PBG. In a quest for a CPBG in the visible, we fabricate and study metallo-dielectric ordered (crystals) and disordered (glasses) photonic materials of metal particles. Furthermore, we demonstrate the fabrication of PCs with complex unit cells and different stoichiometries.

The first part of the thesis describes the fabrication and the characterization of face-centered-cubic (*fcc*) PCs of dielectric (core-shell) spheres in a low-dielectric host (air). In Chapter II.1 we demonstrate the synthesis and optical characterization of the PC's building blocks: well-defined core-shell colloidal particles and hollow shells of zinc sulfide (ZnS) and silica (SiO<sub>2</sub>). The synthesis method allows for the production of monodisperse particles with a tunable core-to-shell size ratio and total radius. These particles are an attractive system for photonic applications because ZnS has a large refractive index and does not absorb light in the visible. In addition, in both ZnS and SiO<sub>2</sub> fluorophores can be easily incorporated. In Chapter II.2, by use of the controlled drying method, we demonstrate the fabrication of large planar PCs of well-defined thickness from SiO<sub>2</sub>, ZnS, and ZnS-core-SiO<sub>2</sub>-shell colloidal particles. We demonstrate, both experimentally and theoretically, that the relative stop gap width in the (111) *fcc* crystallographic direction in the case of high-index core and low-index shell spheres is larger than in a PC of homogeneous spheres of either material. We show that a low-dielectric coating can be used to control the filling fraction of the high-dielectric material and the optical properties of a PC.

The second part of the thesis focuses on the preparation and characterization of photonic materials of different degree of order made of metal colloidal particles. In Chapter III.1 we demonstrate the synthesis and characterization of large ( $R > 100$  nm) silver (Ag) particles. The particles are obtained by reducing silver nitrate with ascorbic acid in aqueous solutions in the presence of a protective polymer. The resulting particles are spherical porous aggregates with a low polydispersity ( $< 20\%$ ) and surface roughness on the order of a few nanometers. The optical properties on a single-particle level are well described if an effective dielectric constant is used. Depending on the volume fraction and the effective polydispersity, in water these particles form charge-stabilized glasses or crystals. In Chapter III.2 we study the optical properties of metallo-dielectric PCs and photonic glasses of sedimented Ag particles in water. Under illumination with white light, these samples display bright colors. A strong modulation is found in the reflectivity of photonic glasses possessing a short-range order only. The general features in the experimental spectra are found in the theoretical reflectivity spectra for *fcc* crystals. From our results, it is likely that amorphous metallo-dielectric materials can be used in some applications where the spontaneous emission of light needs to be modified.

The last part of the thesis deals with PCs with complex lattices and PCs made of non-spherical colloidal particles. In Chapter IV.1 we present the fabrication of binary colloidal crystals through a simple layer-by-layer drying process. We demonstrate the fabrication of crystals with a stoichiometry of large ( $L$ ) and small ( $S$ ) particles of  $LS_2$  and  $LS$ . In addition, we observed the formation of a new  $LS_3$  binary crystal. By using spheres with different composition, one component can be selectively removed. As an example, we demonstrate the synthesis of a hexagonal non-close-packed colloidal crystal. In Chapter IV.2 we demonstrate the fabrication of PCs of ellipsoidal colloidal particles. By use of MeV ion irradiation, we deformed spheres into oblate ellipsoids as organized in a thin 3D colloidal crystal. Both the unit cell symmetry and the particle form factor have been changed as a result of the collective deformation process, leading to an appreciable tunability in the optical properties of the PC.

---

# Acknowledgements

I would like to express my deep and sincere gratitude to many people who made possible the successful outcome of this research work.

First and foremost, I would like to thank my supervisor Prof. Dr. Alfons van Blaaderen for giving me the opportunity to carry out my PhD on this exiting topic. I sincerely thank for the many useful discussions, for the creative and enjoyable atmosphere, and for the given freedom in my research.

I also would like to thank my colleagues from the van't Hoff Laboratory for their support and help and for making the two years I spent there so enjoyable and productive. I am very grateful to Prof. Dr. Henk Lekkerkerker who took risk of accepting the first Bulgarian PhD student in his group, in which I started when my promoter did not have his own group yet. I would like to thank some people who helped me in the beginning to enjoy my work and the Dutch society: my first roommate Felix van der Kooij, for his irresistible sense of humor and invaluable advice; Jacob Hoogenboom, for many discussions and for making me part of the team; Carlos van Kats, for helping me with some syntheses; Diana Maas for the gentle introduction in the field of the electronic microscopy; Prof. Dr. Jan Dhont who was always available to answer my questions, Gilles Bosma, Tjerk Lenstra, Gerard van Ewijk, Carel and Bonny for the technical support, Haran for many discussions, thank You all.

I am very grateful to my wonderful students, Roel Dullens and Gabby Zegers, with who I had the great pleasure to work and share knowledge. Their scientific results became an important part of this thesis.

I would like to thank my colleagues and groupmembers Dirk Vossen, Christina Christova, Dr. Arnout Imhof, Dr. Anand Yethiraj, Dr. Christina Graf, and Dr. Marjolein Dijkstra. I would like to acknowledge the fruitful collaboration with Dr. Alexander Moroz, who provided the theoretical support for this research.

I greatly appreciate the collaboration with my colleagues from Amsterdam Prof. Dr. Albert Polman, Teun van Dillen, Michiel de Dood, Dr. Adriaan Tip, and Han van der Lem (AMOLF), Prof. Dr. Willem Vos, and members of Prof. Dr. Ad Lagendijk's (UvA) group.

I also deeply appreciate the continuous support and important advice from Prof. Dr. Orlin Velev (NCSU, USA) regarding my entire scientific career.

I would like to thank the people from FOM personnel department: Marije van Hussel, Ria Slob, and Reinalda Meyners. I would also like to thank the people from the Audiovisuele dienst: Jan den Boesterd, Ingrid van Rooijen, and Aloys Lurvink, for designing and preparing some of my posters.

During these years in Utrecht, I met many people from different countries. I was very fortunate to make friends for life with some of them. Special thanks should go to Jukka, José Luis, Camilla, Pilar, Alberto, Patricia, Felicity, Bodo, Mika, Pekka, Manuela, Joachim, Karen, Willemien, Karin, Sylvia, Roni, Alice, Alison, Jacob, Felix, Dirk, Gilles, Irinka & Martijn, Martin, Bertha, and Stella. I am deeply grateful to you Ildikó for being by my side and for all the beautiful moments we spent together. I thank my Bulgarian friends in The Netherlands and abroad: Katya, Petya, Goran, Stoyan, Chrissi, Alex, Niki & Ivan, Kiril, Genady, and Dancho. I would like to give my special thanks to the two families of Danka & Kroum and Emi & Ivan, who made me always welcome in their homes.

*Искам да благодаря на всички приятели в България с които споделям добри и лоши моменти. Специално благодаря на Теодор и Весела, Дени и Светли, Левен и Таня, Боби и Пелагия, Иво и Ваня, Анелия, и Кръстанка. Искрено благодаря на Теодора и Валентин Даскалови и на Величка и Трендафил Кутинчеви за тяхната подкрепа и гостоприемство.*

*Дълбоко съм признателен на моите родители, които ме отгледаха и дариха с много обич, за разбирането и подкрепата във всичко което правя, за свободата и доверието които ми гласуваха. Благодаря на брат ми за това че е до тях.*

I dedicate this thesis to my son *Kristian*. His true love and happiness are giving me strength and motivation. With all my love, this is for you.

# Publications

This thesis is based on the following articles:

**Chapter II.1 Synthesis and Characterization of Monodisperse Core-Shell Colloidal Spheres of Zinc Sulfide and Silica**

Velikov, K. P.; van Blaaderen, A. *Langmuir* **2001**, *17*, 4779.

**Chapter II.2 Photonic Crystals of Core-Shell Colloidal Particles**

Velikov, K. P.; Moroz, A.; van Blaaderen, A. *Appl. Phys. Lett.* **2002**, *80*, 49.

**Chapter III.1 Synthesis and Characterization of Large Colloidal Silver Particles for Photonic Applications**

Velikov, K. P.; Zegers, G. E.; van Blaaderen, A. submitted to *Langmuir*.

**Chapter III.2 Photonic Glasses of Colloidal Silver Particles**

Velikov, K. P.; Vos, W. L.; Moroz, A.; van Blaaderen, A. in preparation.

**Chapter IV.1 Layer-by-Layer Growth of Binary Colloidal Crystals**

Velikov, K. P.; Christova, C. G.; Dullens, R. P. A.; van Blaaderen, A. accepted in *Science*.

**Chapter IV.2 Photonic Crystals of Shape-Anisotropic Colloidal Particles**

Velikov, K. P.; van Dillen, T.; Polman, A.; van Blaaderen, A. submitted to *Appl. Phys. Lett.*

Articles to which the author also contributed:

**Colloidal Assemblies Modified by Ion Irradiation**

Snoeks, E.; van Blaaderen, A.; van Dillen, T.; van Kats, C. M.; Velikov, K.; Brongersma, M. L.; Polman, A. *Nucl. Instrum. Methods Phys. Res. Sect. B-Beam Interact. Mater. Atoms* **2001**, *178*, 62.

**Anisotropic Deformation of Colloidal Particles Under MeV Ion Irradiation**

van Dillen, T.; Snoeks, E.; Fukarek, W.; van Kats, C. M.; Velikov, K. P.; van Blaaderen, A.; Polman, A. *Nucl. Instrum. Methods Phys. Res. Sect. B-Beam Interact. Mater. Atoms* **2001**, *175*, 350.

## Manipulating Colloidal Crystallization for Photonic Applications: From Self-Organization to Do-It-Yourself Organization

A. van Blaaderen, K. P. Velikov, J. Hoogenboom, D. Vossen, A. Yethiraj, R. Dullens, T. van Dillen, A. Polman, in NATO ASI: *Photonic Crystals and Light Localization*, C. M. Soukoulis, ed. **2001**.

## Curriculum Vitae

*Krassimir Petkov Velikov* was born in Silistra (a small town on the Danube River) in Bulgaria on 29<sup>th</sup> of June 1970. He completed his primary school in his home-village *Aūdempup*. In 1985, he moved to town of Rouse, where he studied until 1989 in the *Technical Secondary School of Chemical Engineering*. In 1989, he started his undergraduate study in chemistry at the *Department of Chemistry* of the *University of Sofia* (Bulgaria). In 1994, he obtained his M.Sc. degree in Chemistry with specialty Chemical Physics and Theoretical Chemistry. After that, he joined a chemical engineering program at a joint TEMPUS project between the *Laboratory of Thermodynamics and Physico-chemical Hydrodynamics, University of Sofia* (Bulgaria) and universities from the EC in Bordeaux (France), Erlangen-Nürnberg (Germany), Hull (England), Antwerp (Belgium), and Patra (Greece). During this study, he spent three months for research practice in the *Centre de Recherche Paul-Pascal/CNRS* in Pessac in France (there he carried out the experimental part of his second M.Sc.) under the supervision of Dr. B. Pouligny. In March 1997, he obtained his M.Sc. degree in Chemical Engineering with specialty “Separation Techniques in Various Industries and Environmental Protection”. From July 1996 to April 1997, he was appointed as a Research Associate in the *Laboratory of Thermodynamics and Physico-chemical Hydrodynamics, University of Sofia* (Bulgaria). In April 1998, after his military service, he started his Ph.D. in The Netherlands under the supervision of Prof. dr. Alfons van Blaaderen. In the period of April 1998 – June 2000, he was located at the *Van Hoff Laboratory* in the group of Prof. dr. Henk N.W. Lekkerkerker and in the summer of 2000 he was moved to the *Ornstein Laboratory, Debye Institute, University of Utrecht*. The project is a part of the research program in the group of Prof. dr. Alfons van Blaaderen: *Colloidal Matter, FOM AMOLF* (Amsterdam) and *Soft Condensed Matter & Biophysics, Ornstein Laboratory, Debye Institute, University of Utrecht*. A part of the project is a close collaboration with the groups of Dr. Adriaan Tip (Photonic Materials: Theory) and Prof. dr. Albert Polman (Nanostructured Optoelectronic Materials) at *FOM AMOLF*, and Prof. dr. Willem L. Vos at the *Van der Waals-Zeeman Institute, University of Amsterdam*.